# POLITECNICO DI TORINO

Department of Mechanical and Aerospace Engineering

MSc Thesis
in Automotive Engineering

# Development of simplified vehicle models for barrier impact


**Tutor**

Prof. Eng. Alessandro Scattina

**Candidate**

Annibale Spizzirri
ID 291709

December 2023

## Abstract

Nowadays, the FEM approach to face complex problem is becoming much more used than before, saving computational cost and obtaining reliable results. In the automotive field, this strategy could eventually fulfil the goal of modelling complex systems, to simulate for instance a car crash against a barrier, using advanced solvers like LS-Dyna, or other software in development like Euro Plexus, conceived to be used for other applications. From this starting point, the need of having a solid benchmark between the two codes arises, trying to establish a software independent way to solve a numerical problem.

Once this benchmark has been established, understanding what the main differences and the common aspects between the two software are, the work will be moved on analysing a real vehicle impact case.

To the scope of this master thesis, the knowledge of FEM modelling will be applied to the design of safety barriers carried out by the JRC, in order to deeply validate a model – in this case a generic N2/N3 vehicle model, lately adapted to an N2A vehicle category – in the case of an impact with a protective barrier, namely a bollard. This model will be preliminary validated for the chosen experimental test and subsequently tested in different boundary conditions, in order to analyse the influence of varying several parameters, such as the vehicle dimensions or the vehicle speed, rather than the position of the barrier in front of the vehicle.

# Index

## List of Figures

## List of Tables

## List of Equations

# Chapter 1. Introduction and aim of the work

The aim of the present thesis is to deeply investigate the reasons behind the development of safety barriers to protect pedestrians from dangerous terroristic attacks. To arrive to the final scope, a model of a generic N2/N3 vehicle category will be tested, in order to have a deeper validation as far as an impact with a safety barrier is concerned. More specifically, an example of barrier could be, how it will be shown in the following sections, a planar surface barrier, a road blocker or a simple bollard.

The model testing will be performed in *LS-Dyna* and *EPX*, from the JRC [1] side, and for this reason it could be interesting to set a benchmark between the two software, trying to understand their main differences, using the same model, since the simulations should be solver independent. To compare the two codes, some simple examples will be used – a tube shock and a tube shock-crush – representing a strong simplification of several vehicle components, like for instance a vehicle beam.

## 1.1 Terroristic attacks: the history behind the development of safety barriers

In the last decade, an increasing number of attacks that used vehicles to breach the security perimeter of public and social events has been recorded. For this reason, several guidelines [2] [3] [4] propose the use of protective security barriers that guarantee protection against such attacks.

Since there are different classes and categories of vehicles, of various dimensions, it is necessary to assess the risk behind a possible terroristic attack, in order to select the most efficient barrier, in terms of protection of pedestrians and public spaces in general, to reduce to the minimum the possible life losses, as a consequence of an attack.

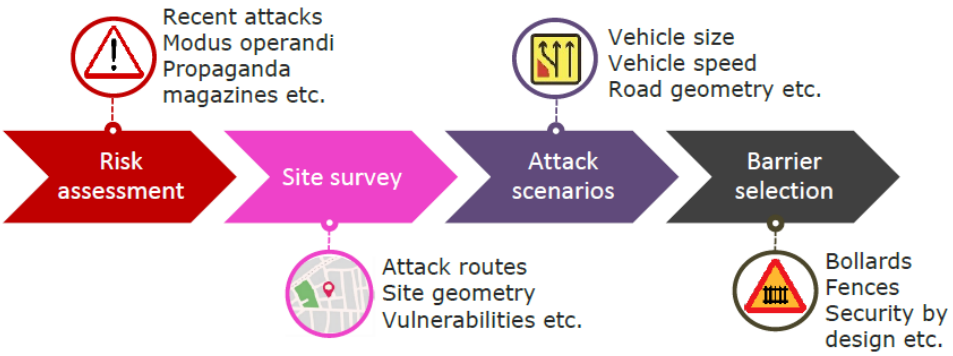


***Figure 1.1*** *– Correct procedure for security barrier selection*

The procedure shown in Figure 1.1 is fundamental to realize the optimal barrier, suitable for the risk that a possible terroristic attack represents for the actual site to protect. A proper layout of a barrier, for instance, could be the one that is aimed to reduce the vehicle speed of the threat vehicle, to minimize the level of victims and destruction.

The most important step to investigate is the *attack scenario*, which involves all those parameters of the vehicles and of the road that aim to assess the possible risks derived from an attack. Some parameters could be for instance the vehicle size or the vehicle speed, since a suitable barrier must absorb the kinetic energy of the vehicle coming from an impact. All these aspects will be analysed in the following section 1.1.1.

### 1.1.1 Vehicles used for terrorist attacks

As a matter of fact, vehicles are becoming the most frequently used solution for terrorist attacks, because of their versatility and the ease of planning. Due to the high number of vehicles categories, the risk behind a terrorist attack, quantified in expected life losses, injuries and destruction, needs to account for different vehicle sizes and speeds. Clearly, the higher the vehicle size and speed are, the higher the threat represented by those vehicles will be, in relation to the possible damages they could cause. Figure 1.2 illustrates the increasing threat for increasing size of the attacking vehicle.

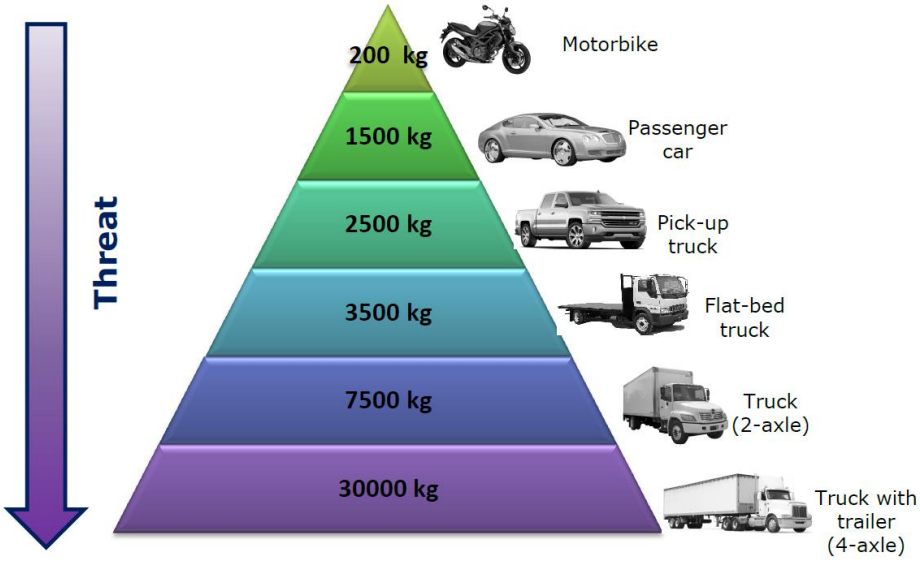


***Figure 1.2*** *– Threat corresponding to vehicle size*

In this thesis, the vehicle model that will be analysed belongs to the generic N2/N3, defined by the *Consolidated Resolution on the Construction of Vehicles (R.E.3)* [5] as vehicles used for goods transportation, whose Gross Vehicle Weight is lower than 12 $tons$. In particular, this model is defined as *generic* since it could be considered representative of both N2A and N3C categories.

Even the vehicle speed is considered a fundamental parameter to evaluate in order to assess the risk connected to a terrorist attack since, as it has been said in the previous section, the main objective of a safety barrier is to absorb the kinetic energy generated by the impact of the vehicle.

Estimating the vehicle weight and its attainable velocity, it is possible to compute the kinetic energy dissipated from an impact with a safety barrier, as indicated by Equation 1.1.

$$E_k = \frac{1}{2}mv^2 \tag{1.1}$$

***Equation 1.1*** *– Kinetic energy dissipated during the impact between vehicle and barriers*

Where $m$ is the vehicle mass and $v$ is the expected impacting speed of the vehicles with the barrier. Clearly, this speed depends on the initial speed, the travel distance and, nevertheless, the acceleration of the vehicle, function of its power-to-weight ratio, the gearshift type, and some other parameters.

### 1.1.2 Barriers to protect pedestrians

The *vehicle barriers* are defined as structural obstacles that block – or at least control – the access of vehicles to a particular area, designated as protected for several reasons (social events, sport events, etc.). Nevertheless, these barriers need to be able to properly stop attacking vehicles from creating a breach into the protected perimeter, so that they must be realized in a proper way, following strict design rules. Indeed, the main goal of a barrier, as it was mentioned in the previous section, is to properly absorb the kinetic energy coming from the impact between the vehicle and the barrier itself.

For the reasons mentioned so far, protective barriers differentiate in shape, materials, size, etc., in order to be compliant with different vehicles categories. As far as materials are concerned, they can be realized in wood, steel, rock, or any other stiff material with a proper absorption capability.

An important distinction that can be made among barriers is based on their capability of being activated by means of an electrical device, namely *active barriers*, or, if they are completely static, *passive barriers*. To this purpose, both categories will be analysed in this thesis, in order to assess which barrier performs better with a prescribed impact.

Bollards, temporary barriers, street furniture or trees belong to the passive classification. The most versatile solution is the *bollard*, whose performance depends on some parameters, like their foundation depth or their size. Other solutions are represented by *re-deployable obstacles*, which must rely on their mass to stop an attacking vehicle, because of the lack of foundation below the soil. Some examples of protective security barriers are shown in Figure 1.3.

***Figure 1.3*** *– Examples of bollards and temporary re-deployable barriers*

Clearly, every barrier type has pros and cons, regarding for instance the monotony of the bollards, namely aesthetic reasons, or even the incapability of temporary barriers to deal with high-speed impacts. As it has been explained in the previous sections of the current Chapter 1, the choice

of the most suitable barrier should be a good compromise, depending on the study done on the possible scenario of a terroristic attack.

## 1.2 Software for model development: LS-Dyna and EPX

The most used software to develop a vehicle model for explicit Finite Element analysis is LS-Dyna, whit its *.k* input file. For this reason, a great effort has been made in order to create a compatibility with EPX, which is the software used by the JRC.

In particular, EPX has to be able to read all the basic inputs to perform the calculations, such as the geometry, the coordinates of the nodes and their connectivity.

Nevertheless, there are several parameters that are difficult to be translated from one code to the other, due to the variability of the keyword cards, like for instance the material law, rather than the methodology of calculation of some parameters that will be described in the following sections.

### 1.2.1 Contacts in LS-Dyna

It is important to define how the contact between two parts occurs in LS-Dyna [6], being a fundamental aspect of this thesis. For each couple of contacting parts, a slave and a master part need to be specified. More in detail, it is possible to define:

- **Master**: it is the part that is *constrained* during the contact.
- **Slave**: it is the *moving* part.

These two entities can be set as a part, a part set, or even a node set. In some cases, it could be useful to select the softest part as slave, even if it is fixed, since this can provide more reliable results. The logic behind a contact is shown in Figure 1.4.

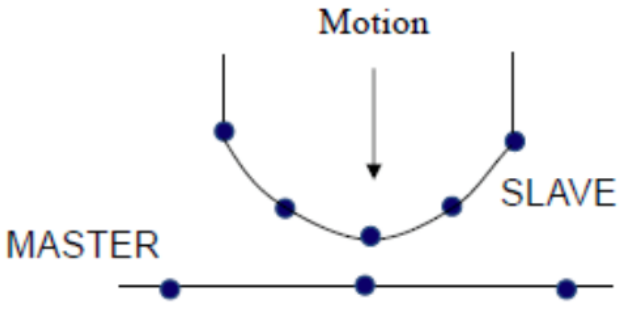


***Figure 1.4** – Example of contact in LS-Dyna*

For the purposes of this thesis, two contact cards are mainly used to describe the contacts in the models, which are:

- **AUTOMATIC_SINGLE_SURFACE**: it uses only a slave part, checking for all possible contacts with other surfaces. This option is also called "*auto contact*".
- **AUTOMATIC_SURFACE_TO_SURFACE**: it needs the definition of a master and a slave part.

The concept of *segment* is a key aspect inside the code, since LS-Dyna converts the faces of the elements involved in the contact in segments, involving three or four nodal points, as it is illustrated in Figure 1.5.

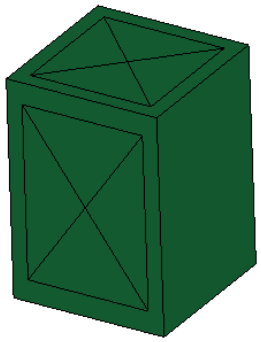

***Figure 1.5** – Element faces involved in a contact*

The top and left faces are involved in the contact, so the code converts the faces in segments, starting from a nodal point analysis. The right face instead, is not considered for the contact, so it is not considered as a segment.

In the next section, a deep analysis of how the contact is formulated in LS-Dyna will be carried out, highlighting the main differences between each contact formulation.

### 1.2.2 Contact Penalty Formulations

LS-Dyna analyses the contact between two parts according to the formulation chosen by the user. Clearly, depending on which contact formulation has been chosen, the code calculates the contact stiffness in different ways. The most used formulations are the following ones:

- **Penalty-based formulation**: this is the default contact algorithm used in LS-Dyna, named *SOFT = 0* in the rest of the thesis. This contact option detects penetration of nodes into segments, and consequently applies penalty forces to the penetrating nodes and segment nodes. The contact stiffness, for shell elements, is computed through the following Equation 1.2, where $\alpha$ is the penalty scale factor, $A$ is the segment area and $K$ is the material bulk modulus.

$$k = \frac{\alpha K A}{Max\ shell\ diagonal} \tag{1.2}$$

***Equation 1.2** – Contact stiffness for shell elements for SOFT = 0*

Here the contact force at the interface between the two parts in contact is considered as an elastic force exploited by a spring of stiffness $k$ and displacement $\delta_i$, as indicated in Equation 1.3.

$$F_i = \delta_i k \tag{1.3}$$

***Equation 1.3** – Contact force at the contact interface*

The displacement of these ideal springs represents the amount of penetration that occurs between two parts. Figure 1.6 shows the mechanics behind this type of contact.

- **Soft-constraint penalty-based formulation**: it detects penetration of nodes into segments in the same way of the default algorithm, named *SOFT = 1*. The only noticeable difference with the SOFT = 0 option is the way the contact stiffness is computed, as it is shown in Equation 1.4.

$$k_{cs}(t) = 0.5 \cdot SOFSCL \cdot m^* \left(\frac{1}{\Delta t_c(t)}\right) \tag{1.4}$$

***Equation 1.4*** *– Contact stiffness for shell elements for SOFT = 1*

Nevertheless, this contact formulation will not be mentioned in this work.

- **Segment-based formulation (pinball)**: this option detects penetration of one segment into another one, and then applies penalty forces to the segment nodes, named *SOFT = 2*. This formulation is used to enforce the impenetrability of the two parts, since it can give better results in case of contacts between sharp edges. Equation 1.5 shows how the contact stiffness is computed with this contact algorithm.

$$k_{cs}(t) = 0.5 \cdot SLSFAC \cdot \begin{Bmatrix} SFSA \\ or \\ SFSB \end{Bmatrix} \left(\frac{m_1 m_2}{m_1 + m_2}\right) \left(\frac{1}{\Delta t_c(t)}\right) \tag{1.5}$$

***Equation 1.5*** *– Contact stiffness for shell elements for SOFT = 2*

It is worth highlighting that explaining how the contact stiffness is computed by the software is not the final goal of this work.

Figure 1.6 and Figure 1.7 illustrate how the segments in contact are treated and how the contact between two parts occurs with this contact option.

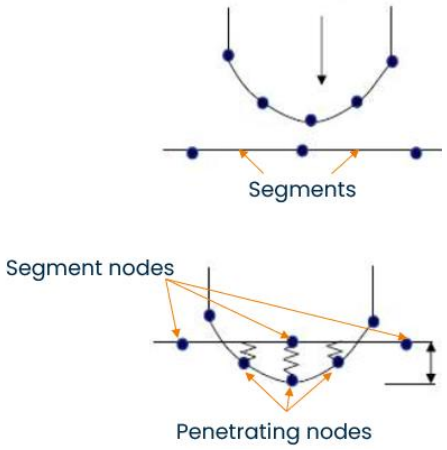


***Figure 1.6*** *– Mechanics of SOFT = 0 contact algorithm*

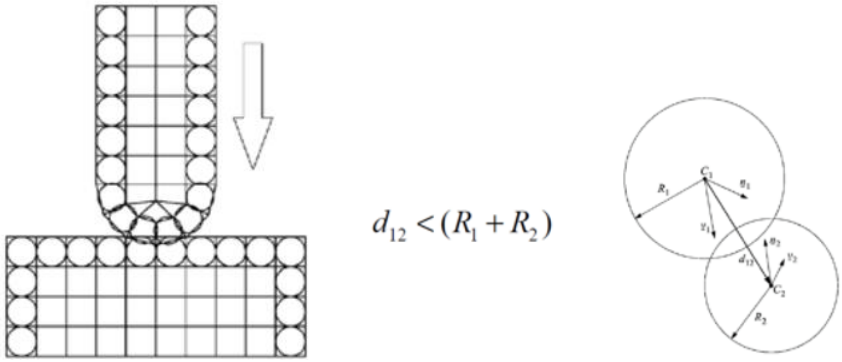


***Figure 1.7** – Mechanics of SOFT = 2 contact algorithm*

In particular, for SOFT = 2, the contact occurs when $d_{12} < (R_1 + R_2)$, where $R_1$ and $R_2$ are the radius of the circumferences – for this reason, this option is called *pinball algorithm* – and $d_{12}$ is the distance between the two centers of the circumferences.

### 1.2.3 Contact energy computation and time integration method in LS-Dyna

Estimating the contact energy is important to understand if there are undetected penetrations of elements during a contact between two parts. Due to this relevance, it is important to define how this contact energy is computed inside the code, and this definition is provided by Equation 1.6.

$$E_{contact}^{n+1} = E_{contact}^{n} + \left[\sum_{i=1}^{nsn} \Delta F_i^{slave} \times \Delta dist_i^{slave} + \sum_{i=1}^{nmn} \Delta F_i^{master} \times \Delta dist_i^{master}\right]^{n+\frac{1}{2}} \quad (1.6)$$

***Equation 1.6** – Contact energy calculation in LS-Dyna*

Basically, the contact energy – also named *Net Contact Energy* – is updated every $n$ time step size and can be considered as the sum of slave and master contact energy. Moreover, this calculation is done for every slave and master nodes involved in the contact – $nsn$ and $nmn$ – while $F_{slave}$ and $F_{master}$ are the interface forces of the slave and master nodes at the contact interface and $\Delta dist_{slave}$ and $\Delta dist_{master}$ are the incremental distances that slave and master nodes have moved during the time step $n \rightarrow n + 1$.

Having stated this, the value that the contact energy can assume during a contact strongly depends on the boundary conditions imposed by the case study of interest:

- If friction is included, positive contact energy accumulates due to the dissipative frictional energy.
- If friction is not included, the net contact energy is expected to be zero, or at least lower than the 10% of the peak value of the internal energy of the system, in order to avoid instability of the results.
- Negative contact energy instead, can cause parts to slide between each other, rather than penetrated nodes to slide from its original master segment to an adjacent one, through unconnected master segment. At this stage, a penetration is immediately detected.

An abrupt increase in negative contact energy values may be caused by undetected initial penetration of elements, even before the calculations have started. For this reason, it is fundamental

to provide a sufficient initial gap between parts in contact, in order to avoid this condition to occur.

It is worth highlighting that contact energy, rather than internal energy, needs to be integrated in time. So it would be useful to understand how the time integration loop of LS-Dyna works, as illustrated in Figure 1.8.

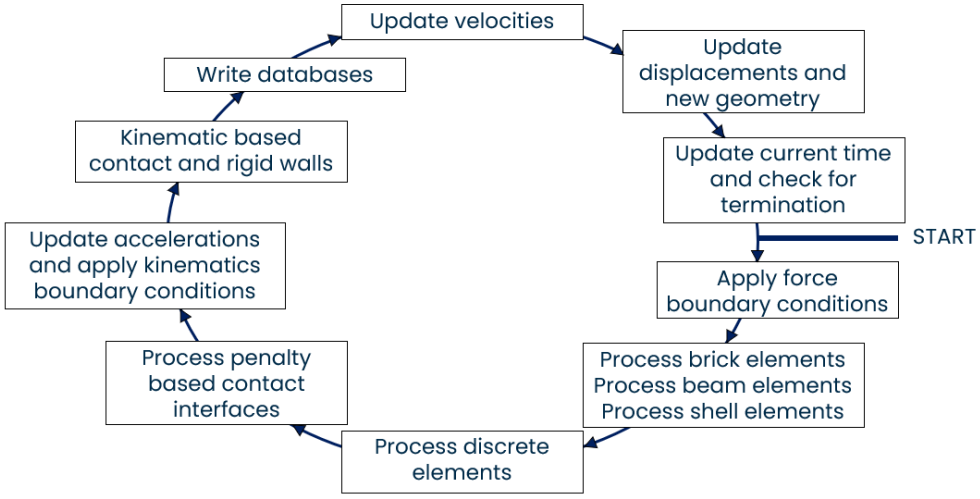


***Figure 1.8*** *– Time loop integration in LS-Dyna*

More in detail, LS-Dyna uses a modification of the *Central Difference time integration method*, in which the geometry of the elements is used as integration variable to solve differential equations. In this way, displacements, velocities and accelerations are updated through calculations. Anyway, describing this process is not the scope of the thesis.

### 1.2.4 Added mass computation in LS-Dyna

*Mass scaling* is a term that is used for the process of scaling the elements mass in explicit simulations to adjust their time step. The primary motivation is to change – usually an increase is preferred to a decrease – the global output time step, which is limited by the Courant's stability criteria.

In LS-Dyna it is possible to perform the mass scaling using the *DT2MS* parameter inside the *CONTROL_TIMESTEP* card, with the default set to no mass scaling. When *DT2MS* is less than zero, the code adds mass to each element whose time step falls below the absolute value of *DT2MS*, such that the element updated $\Delta t$ becomes equal to |DT2MS|. When *DT2MS* is greater than zero instead, the software adds mass to elements whose time step falls again below the absolute value of *DT2MS*, while "removing" mass from elements whose time step is greater than zero. However, this option is seldom used, since the main objective should be to overcome the smallest computed time step.

Nevertheless, care should be taken when using mass scaling, since added mass could have an adverse effect on the simulation accuracy. For this reason, as it will be also stated in the example of the tube shock analysis of Chapter 2, it is common practice to limit the percentage of added mass to less than 5% of the total mass of the part in dynamic simulations. Figure 1.9 graphically describes the way in which mass scaling is performed during simulations.

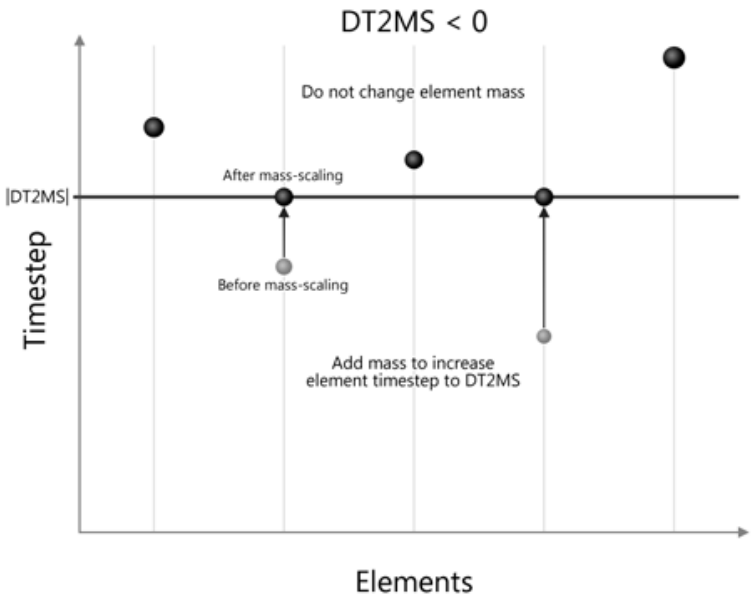


***Figure 1.9*** *– Added mass logic in LS-Dyna*

For sake of completeness, it is worth underlining that it is also possible to limit the mass scaling just to the first compute cycle, using the parameter *MS1ST* – set to 1 – inside the card *CONTROL_TIMESTEP*, or even to perform a dynamic mass scaling, using monotonically increasing load curve, even though this is common practice in simulations in which some time instants are dominated by inertia effects, so that performing the mass scaling during this instants could affect the system response. By the way, this will not be the subject of investigation during this work.

# Chapter 2. Tube shock analysis

In this section, an analysis on a tube, impacting against a rigid wall, is conducted, in order to verify how it behaves in terms of energies and momentum, even though this is a relative goal.

More in detail, the final objective of this test, as it will be for that one performed in Chapter 3, consists of comparing the results obtained in LS-Dyna with those obtained in EPX, in order to understand how the two software behave when analysing the same model, and to check the consistency between them.

For sake of completeness, here the tube can be considered as a strong simplification of a vehicle beam that undergoes an incident.

## 2.1 Plastic model and contact setup: Tube and Rigid Barrier

**Model setup**

The model that will be analysed, and shown hereafter in Figure 2.1 is composed by:

- A *tube*, with a squared section and made of a plastic deformable steel.
- A *rigid barrier*, made with the same material characteristic of the tube, and completely constrained in all directions.

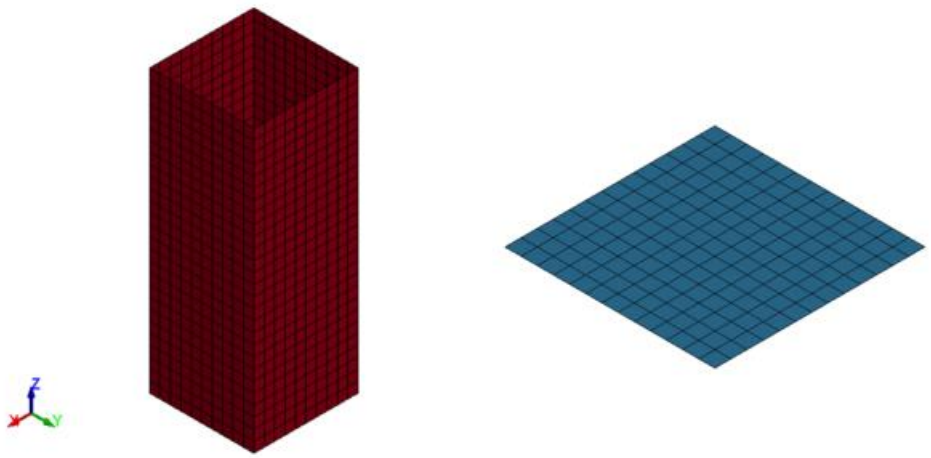

***Figure 2.1*** *– Tube and rigid barrier model representation*

The material of the tube has the characteristic shown in Figure 2.2. This material is modelled using the card *024_PIECEWISE_LINEAR_PLASTICITY*, which behaves as a plastic *deformable steel* that has the characteristics listed in Table 2.1.

The material of the barrier instead, is modelled as a *rigid steel*, using the card *020_RIGID*, with the characteristics listed in Table 2.2.

It is noticeable that the material used for modelling the two parts is the same, but it has a different behaviour in the two cases.

| ***PARAMETER*** | *SYMBOL* | *VALUE* |
|---|---|---|
| ***YOUNG'S MODULUS*** | $E\ (MPa)$ | 200000 |
| ***POISSON'S RATIO*** | $\nu\ (-)$ | 0.3 |
| ***DENSITY*** | $\rho\ (kg/\mathrm{m}^3)$ | 7830 |
| ***YIELD STRESS*** | $\sigma_Y$ (MPa) | 207 |
| ***EFFECTIVE PLASTIC FAILURE LIMIT*** | $\varepsilon_Y\ (-)$ | 0.75 |

***Table 2.1*** *– Deformable steel parameters*

| ***PARAMETER*** | *SYMBOL* | *VALUE* |
|---|---|---|
| ***YOUNG'S MODULUS*** | $E\ (MPa)$ | 200000 |
| ***POISSON'S RATIO*** | $\nu\ (-)$ | 0.3 |
| ***DENSITY*** | $\rho\ (kg/\mathrm{m}^3)$ | 7830 |

***Table 2.2*** *– Rigid steel parameters*

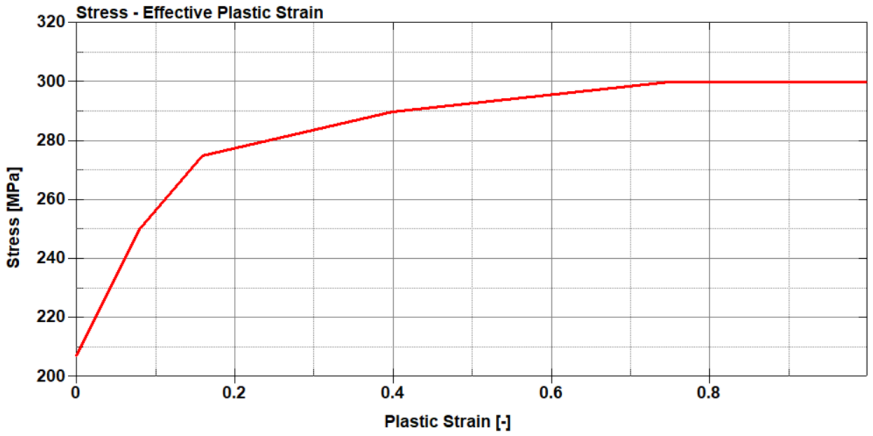


***Figure 2.2*** *– Characteristic of a deformable steel subjected to a tensile test*

The mesh of the two parts is characterized by shell elements of different sizes, in order to avoid some criticalities, as far as the contact is concerned, as it is indicated in Table 2.3. The other important parameter to be set is the *Element Formulation*, which has a great influence on the results. To this purpose, a deeper analysis on the influence of the element formulation on the results will be performed in the following Chapter 3. For this case of study, the element formulations that will be used are:

- **ELFORM = 2**: *Belytschko-Tsay* formulation, used for the rigid barrier.
- **ELFORM = 16**: *Fully integrated shell element* formulation, used for the tube.

| ***PART*** | *MESH SIZE (mm)* |
|---|---|
| ***TUBE*** | 10 |
| ***RIGID BARRIER*** | 11.5 |

***Table 2.3*** *– Mesh size of the two parts*

Being made of shell elements, both parts have a low thickness, shown in Table 2.4, in order to be consistent with the *shell* definition, in which the thickness has to be much lower than the other dimensions.

| ***PART*** | *SHELL THICKNESS (mm)* |
|---|---|
| ***TUBE*** | 2 |
| ***RIGID BARRIER*** | 2 |

***Table 2.4*** *– Shell element thickness of the two parts*

Regarding boundary conditions, an initial velocity of $-10\ m/s$ is applied to the tube, towards the Z direction, in order to make it impact against the rigid barrier, while the duration of the simulation has been set to $5\ ms$. In this case, a compression of the tube of about $10\ mm$ is expected.

**Contact setup**

Proceeding with the contact setup, the card used in LS-Dyna to setup the contact between the tube and the rigid barrier is *AUTOMATIC_SURFACE_TO_SURFACE*. More in detail, the Contact Penalty Formulations (as reported in section 1.2.2) used for this case of study are the following ones:

- **SOFT = 0**: Standard Penalty Formulation
- **SOFT = 2**: Segment-based (Pinball) Contact Penalty Formulation

For each Contact Penalty Formulation, the results obtained in LS-Dyna will be compared to the ones obtained in EPX by the JRC.

Moreover, for each contact formulation, the methodology used to perform the sensitivity analysis consists of varying the Scale Factors of the contact stiffness, in a range between 1 and 5, to analyse the influence of the contact stiffness on the results. This test plan is better represented in Table 2.5.

In this case, no friction – neither static nor dynamic – between the tube and the barrier will be considered, and all the other contact parameters have been left by default.

## 2.2 Results and comparison with EPX

In this section, following the aim of the work, the results obtained in LS-Dyna will be compared to the ones of EPX on the same model, in terms of internal, kinetic and total energies, other than momentum along the Z direction.

In the plots shown in Figure 2.3, the two curves used as reference for the comparison between the software are the ones obtained in EPX, with two contact options – namely *EPX Liaj 0* and *EPX Liaj 1*, corresponding to the ideal infinite and zero stiffnesses respectively.

To begin with the comparison, the following first results, highlighted by the red curves of Figure 2.3, are obtained in LS-Dyna using the Standard Contact Penalty Formulation (SOFT = 0) and the default contact stiffness. Then, a sensitivity analysis on the influence of the contact formulation and stiffness will be lately carried out.

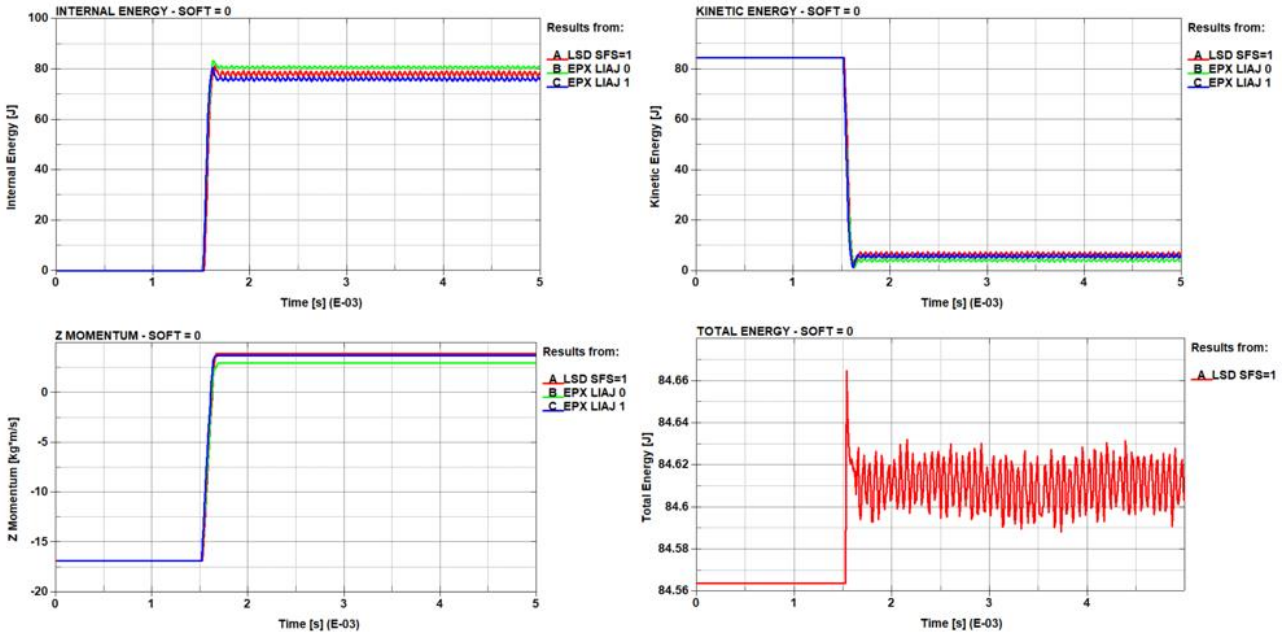


***Figure 2.3** – Preliminary results comparison of tube shock with SOFT = 0*

The results show a good consistency between the two software, since all the curves have the same trend of the ones obtained in EPX. The plot of the total energy was not provided by JRC for the two Liaj contact options, so that only the one relative to LS-Dyna has been shown.

The most evident and noticeable difference concerns the Z momentum plot, which is characterized by little oscillations slightly after the impact between the two parts, instead of the highly oscillating behaviour shown by the energies. This is directly related to the Z momentum linear dependence from the tube velocity, instead of the quadratic one that characterizes the energies. Regarding energies instead, the high frequency oscillations are related to the small *output time step* that has been chosen ($1e-05\ s$). It has been demonstrated in EPX indeed, by the JRC, that decreasing the output time step leads to a consistent increment of the oscillations frequency of the results.

As far as the total energy is concerned, it is well known that, thanks to the energy conservation principle, it should be equal to the sum of all the energy contributions. This is also the explanation of

why the internal and kinetic energies are perfectly symmetric. Nevertheless, the total energy is not perfectly constant, due to some other contributions, given for instance by the hourglass energy, measure of the distortion of the elements, the sliding energy or the rigid wall energy. By the way, looking at the total energy plot, the curve oscillates in a very narrow interval, so that all these additional components do not have a huge impact on results, and for this reason they will not be analysed in deep in this case of study.

### 2.2.1 Influence of Contact Penalty Formulation and SFS

In the following sections, the results previously shown, relative to the internal, kinetic and total energies, rather than the momentum along the Z direction, are shown, with a particular attention to the influence that a variation of the Stiffness Scale Factor parameters has on all the results. Table 2.5 describes the plan used to perform the analysis.

| ***CONTACT PENALTY FORMULATION*** | *SFS VARIATION* | | |
|---|---|---|---|
| ***SOFT = 0*** | 1 | 2 | 4 |
| ***SOFT = 2*** | 1 | 3 | 5 |

***Table 2.5*** *– Planning of the analysis on SFS factors*

The variation of the SFS parameters is not the same for the two contact formulations since it has been verified that a greater influence on the results was achieved with a further increasing of the SFS parameters for the pinball contact option. Nevertheless, increasing more than 5 led to unvaried results, so that 5 has been identified as the upper limit value of SFS for SOFT = 2. The same condition holds for the formulation SOFT = 0, where the upper limit has been set to 4, as it is shown in Table 2.5.

Moreover, an analysis of the average values of the oscillations will be lately performed, in order to evaluate the discrepancy between the results obtained in LS-Dyna and those obtained in EPX.

**Internal Energy – SOFT = 0**

The plots relative to the internal energy, using the SOFT = 0 Contact Penalty Formulation, are shown in Figure 2.4. The right one shows a zoomed view of the plot, since it would be useful to appreciate the oscillations present in the curves. For this reason, a mean value of these oscillations will be computed, and then a comparison between these averages will be explained in later sections.

In particular, the approach described above will be followed throughout the whole analysis, since all the results are heavily characterized by oscillations.

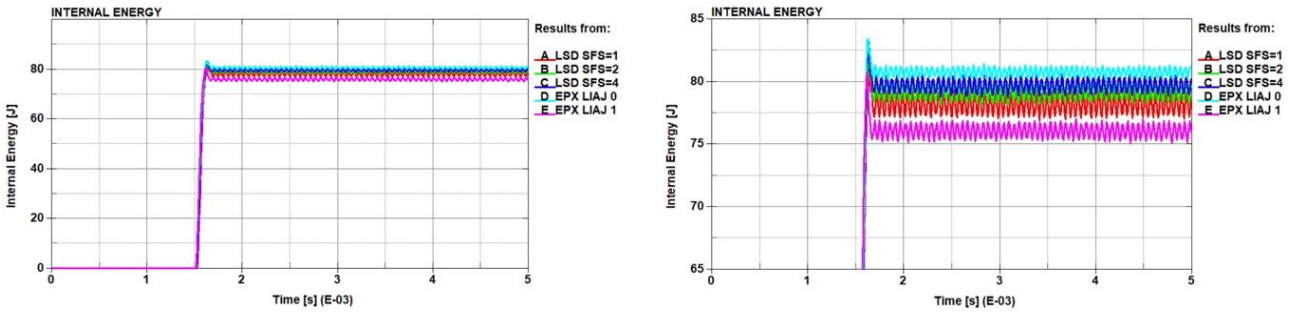


*Figure 2.4 – Time history plots of internal energy with SOFT = 0*

The influence of the SFS parameters is clearly visible, since the curves seem to shift up increasing the Scale Factors, moving closer to the one relative to the Liaj 0 contact setup of EPX, corresponding to the ideal case of infinite stiffness. The increase of the internal energy with the contact stiffness can be explained by Equation 1.3 of Chapter 1, regarding the computation of penalty forces at the contact interface between the tube and the rigid barrier. It is well known that the internal energy is the measure of the deformed state of a system. As a consequence, being the contact stiffness higher, a higher penalty force will be applied to the penetrating nodes, causing a more deformed tube after the impact.

Moreover, it was verified that increasing the SFS further than the value of 4 would have led to a result deviation from the reference of EPX.

**Kinetic Energy – SOFT = 0**

The trend of the kinetic energy is exactly specular with respect to the internal one, thanks to the energy conservation, also showing the same type of oscillations. As expected, after the impact, a drop of the kinetic energy is appreciated, due to a reduction of the tube velocity, but even because of the conservation of the total energy that, being defined at the beginning of this section 2.2, has to remain more or less constant. This time, the curves shift down increasing the SFS parameters, always towards the Liaj 0 contact option of EPX, as it is shown in Figure 2.5.

This time, the movement of the curves is less marked than the case of the internal energy, with larger amplitudes of oscillation. In any case, the results seem to be coherent with the ones of EPX.

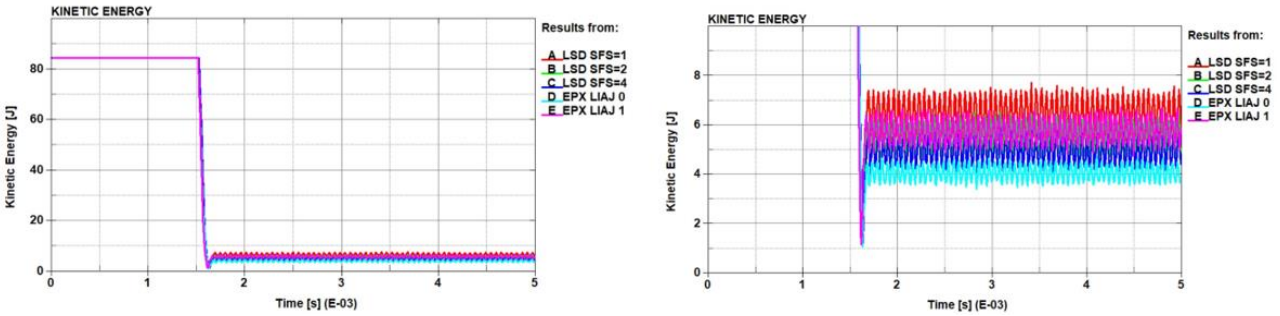


*Figure 2.5 – Time history plots of kinetic energy with SOFT = 0*

Also in this case, the influence of the variation of the SFS parameters is evident from the

zoomed plot, with a progressive shifting down, towards the EPX Liaj 0 curve, as the contact stiffness increases. It is important to underline that, after the impact, most of the energy of the system remains internal, due to the use of an elasto-plastic material to model the tube that causes a permanent plastic deformation of the tube itself.

### Total Energy – SOFT = 0

As far as the total energy is concerned, only an analysis on the results obtained in LS-Dyna was conducted, in order to appreciate the influence of the variation of the SFS parameters also with this component.

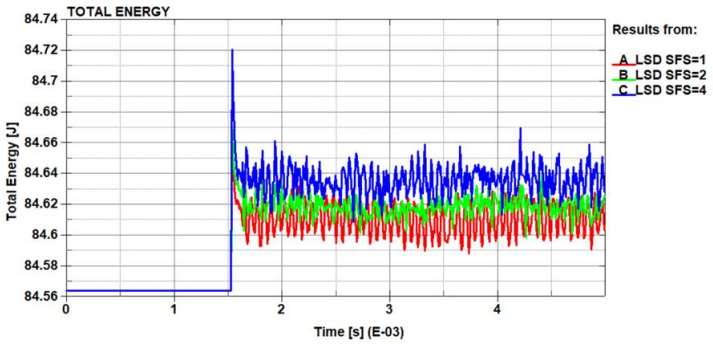


*Figure 2.6 – Time history plot of total energy with SOFT = 0*

Being defined as it was stated in section 1.2.3, the total energy has the same trend of the other results, with a different amplitude of oscillations. In addition to that, it remains more or less constant, as expected – small discrepancy with respect to the initial value is appreciable indeed. As it can been seen from Figure 2.6, increasing the contact stiffness, the energy content of the system increases as well, also with a higher peak in the response just after the impact between tube and barrier occurs.

### Z Momentum – SOFT = 0

The Z momentum is characterized by a lower oscillating trend, settling, after the impact between the tube and the barrier, to an almost constant value, as it was previously shown in Figure 2.3.

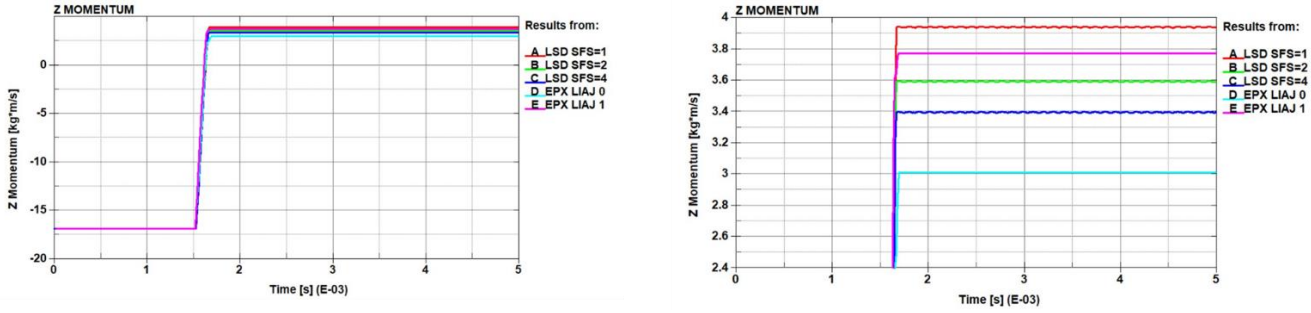


*Figure 2.7 – Time history plots of Z momentum with SOFT = 0*

As in the previous cases, increasing the Scale Factors leads to the movement of the curves towards the Liaj 0 option of EPX, even if all the results trends are coherent with the two reference curves – both Liaj 0 and Liaj 1 contact configurations.

### Internal Energy – SOFT = 2

This time, the Contact Penalty Formulation was changed to SOFT = 2, so that the pinball contact was used to test the system.

As it is visible from Figure 2.8 – and for the other results as well later on – this contact option seems to be not so suitable for low contact stiffness values, as there is any coherence with the results obtained with EPX.

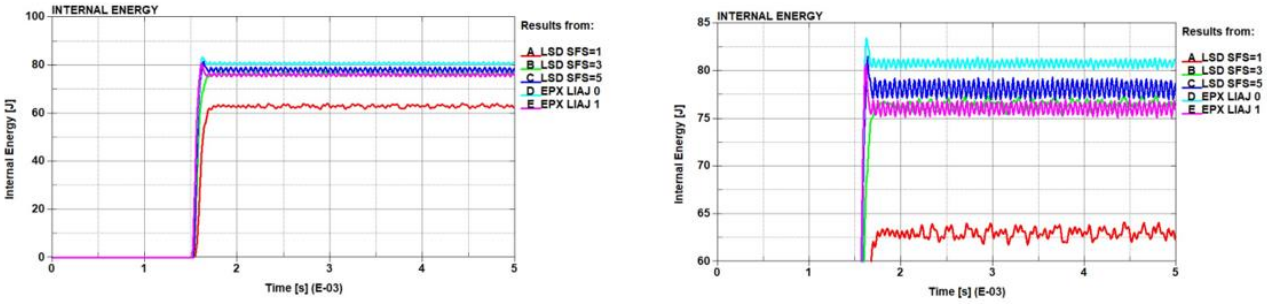


***Figure 2.8*** *– Time history plots of internal energy with SOFT = 2*

However, increasing the contact stiffness, the results become consistent with the reference curves of EPX, standing, with stationary oscillations, in between Liaj 0 and Liaj 1 curves. It is evident that, even from the other results, stiffer contacts imply a higher energy absorption of the system, so that a shift up of the curves is justified. Indeed, this is a consequence of the definition of *Segment-based Contact Penalty Formulation* (SOFT = 2) provided in section 1.2.2, according to which the contact is analysed by the solver as if there were springs at the interface between the slave segment and the master segment.

### Kinetic Energy – SOFT = 2

As for the previous contact option, also in this case, the kinetic energy has a specular trend with respect to the internal one, showing again a not acceptable behaviour until the contact stiffness is scaled with a higher SFS parameter – i.e. up to 5.

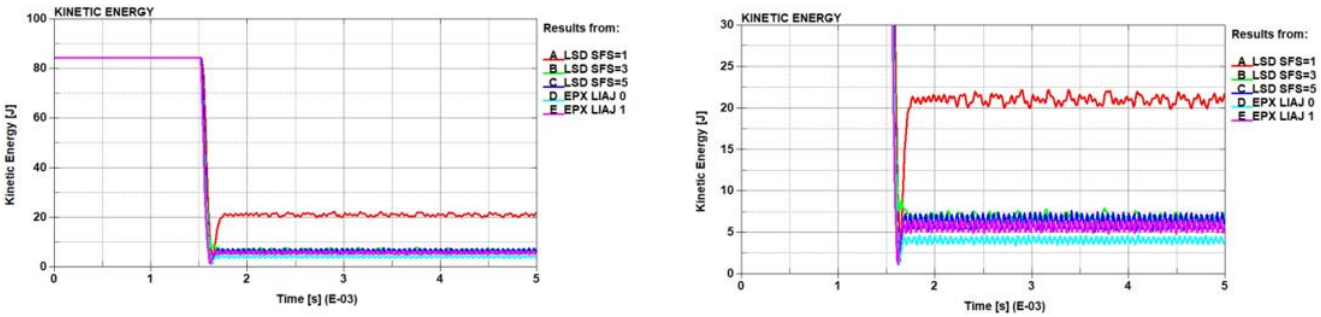


***Figure 2.9*** *– Time history plots of kinetic energy with SOFT = 2*

The evident difference here in Figure 2.9 is that the kinetic energy with the highest contact stiffness seems to be overlapped to the curve relative to the Liaj 1 contact option of EPX, differently from what it has been shown up to now.

**Total Energy – SOFT = 2**

In this case, the influence of the increment of the contact stiffness is higher with respect to the other contact option – i.e. SOFT = 0. Other than an increment in the amplitude of the oscillations, the total energy shows a higher peak, after the impact between the tube and the barrier, while increasing the SFS factors.

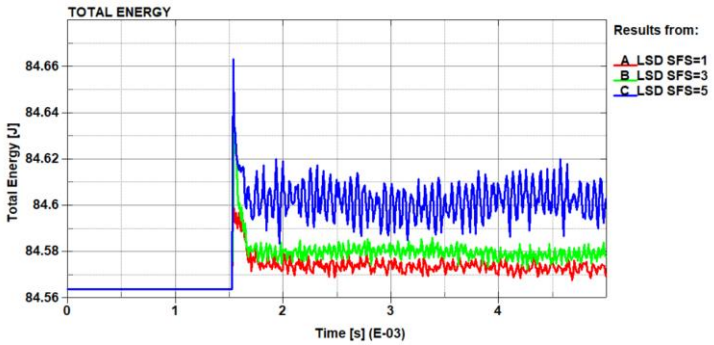


***Figure 2.10*** *– Time history plot of total energy with SOFT = 2*

Nevertheless, the oscillations relative to the blue curve (SFS = 5) of Figure 2.10 seem to be less stable than the other two, which are steadier relatively to their respective average values. This could be related to the definition of total energy, given in section 1.2.3 – so that the summation of kinetic and internal energy, other than contact energy as well. As it is visible from Figure 2.8 and Figure 2.9 indeed, the oscillations of the blue curves relative to SFS = 5 have higher amplitudes, both for kinetic and internal energy, with respect to the less stiff contacts.

**Z Momentum – SOFT = 2**

As far as the Z momentum is concerned, the case of SFS = 1 seems to be completely misleading with respect to the reference curves, while, increasing the contact stiffness, the results become more consistent with the ones obtained in EPX, as it is appreciable from Figure 2.11.

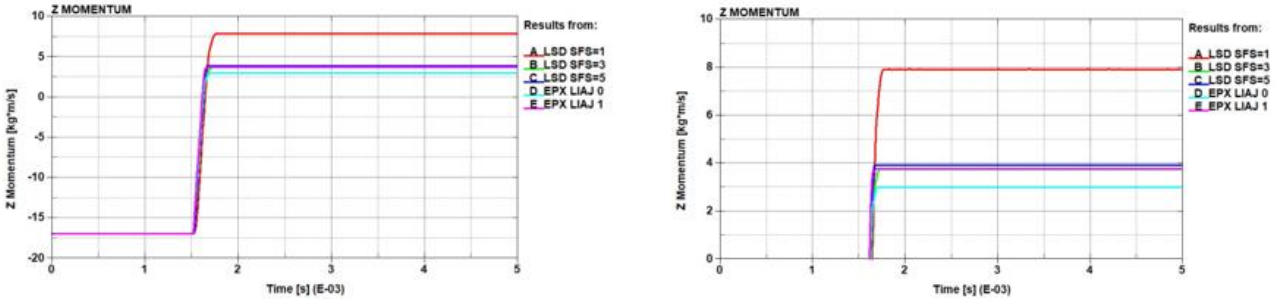


*Figure 2.11 – Time history plots of Z momentum with SOFT = 2*

As it was stated before, the curves relative to Z momentum are not oscillating, but they settle, right after the impact, to an almost constant value, thanks to their linear dependence on the tube velocity.

### 2.2.2 Statistical analysis on software comparison

Once having graphically compared the results in terms of energy components and Z momentum, it would be useful to compute a mean value of the curves, between 2 $ms$ and 5 $ms$, in order to understand the value around which the oscillations are concentrated, rather than the real difference – and as a consequence, the deviation – existing between LS-Dyna and EPX.

Table 2.6 and Table 2.7 show the mean value for each of the five curves, and for each contact option respectively.

| SOFT = 0 | INTERNAL ENERGY<br>Mean value between 2 ms and 5 ms | KINETIC ENERGY<br>Mean value between 2 ms and 5 ms | TOTAL ENERGY<br>Mean value between 2 ms and 5 ms |
|---|---|---|---|
| LSD SFS= 1 | 78.2 J | 6.37 J | 84.61 J |
| LSD SFS= 2 | 79.2 J | 5.47 J | 84.62 J |
| LSD SFS= 4 | 79.8 J | 4.89 J | 84.64 J |
| EPX LIAJ 0 | 80.8 J | 4.04 J | 84.84 J |
| EPX LIAJ 1 | 76.1 J | 5.74 J | 81.84 J |

| SOFT = 2 | INTERNAL ENERGY<br>Mean value between 2 ms and 5 ms | KINETIC ENERGY<br>Mean value between 2 ms and 5 ms | TOTAL ENERGY<br>Mean value between 2 ms and 5 ms |
|---|---|---|---|
| LSD SFS= 1 | 62.7 J | 21.5 J | 84.57 J |
| LSD SFS= 3 | 76.5 J | 6.28 J | 84.58 J |
| LSD SFS= 5 | 78.2 J | 6.29 J | 84.6 J |
| EPX LIAJ 0 | 80.8 J | 4.04 J | 84.84 J |
| EPX LIAJ 1 | 76.1 J | 5.74 J | 81.84 J |

*Table 2.6 – Mean values of curves btw 2 ms and 5 ms for SOFT = 0 and SOFT = 2*

Once having computed the mean values, the percentage differences of the results obtained from EPX, with respect to LS-Dyna total energy, are computed.

| SOFT = 0 | | %Difference* w.r.t. LSD Total Energy SFS = 1 | %Difference w.r.t. LSD Total Energy SFS = 2 | %Difference w.r.t. LSD Total Energy SFS = 4 |
|---|---|---|---|---|
| INTERNAL ENERGY | EPX LIAJ 0 | 2.1% | 1.9% | 1.2% |
| | EPX LIAJ 1 | 2.4% | 3.6% | 4.4% |
| KINETIC ENERGY | EPX LIAJ 0 | 2.8% | 1.7% | 1% |
| | EPX LIAJ 1 | 0.7% | 0.3% | 1% |
| TOTAL ENERGY | EPX LIAJ 0 | 0.27% | 0.25% | 0.23% |
| | EPX LIAJ 1 | 3.2% | 3.3% | 3.3% |

| SOFT = 2 | | %Difference w.r.t. LSD Total Energy SFS = 1 | %Difference w.r.t. LSD Total Energy SFS = 3 | %Difference w.r.t. LSD Total Energy SFS = 5 |
|---|---|---|---|---|
| INTERNAL ENERGY | EPX LIAJ 0 | 21.4% | 5.1% | 3.1% |
| | EPX LIAJ 1 | 15.8% | 0.5% | 2.5% |
| KINETIC ENERGY | EPX LIAJ 0 | 20.6% | 2.6% | 2.7% |
| | EPX LIAJ 1 | 18.6% | 0.6% | 0.7% |
| TOTAL ENERGY | EPX LIAJ 0 | 0.32% | 0.31% | 0.28% |
| | EPX LIAJ 1 | 3.2% | 3.2% | 3.3% |

*Table 2.7 – %Difference btw EPX and LSD total energy for SOFT = 0 and SOFT = 2*

As it is visible from Table 2.6 and Table 2.7, the percentage difference between EPX and LS-Dyna is quite high for the SOFT = 2 contact formulation, as it was expected from the analysis performed on the previous plots. In general, a difference always lower than 3% is appreciable for the Liaj 0 contact option in EPX, coherently to what it is shown in the plots, even though there is a not so high discrepancy with LS-Dyna, as far as EPX Liaj 1 is concerned instead.

In order to have a better view of this existing difference between the two software, some histograms are shown hereafter in Table 2.8 and Table 2.9, to give to these results a statistical representation as well.

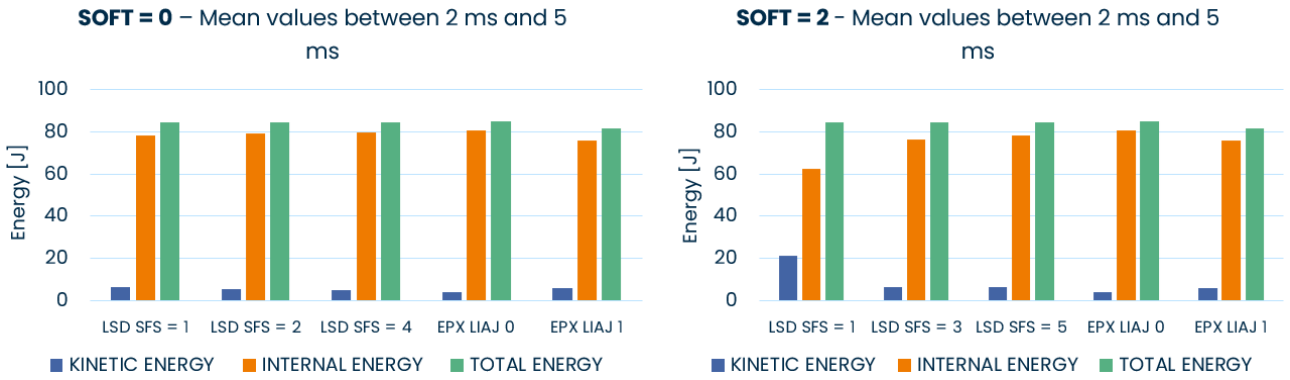


*Table 2.8 – Histogram mean values of curves for SOFT = 0 and SOFT = 2*

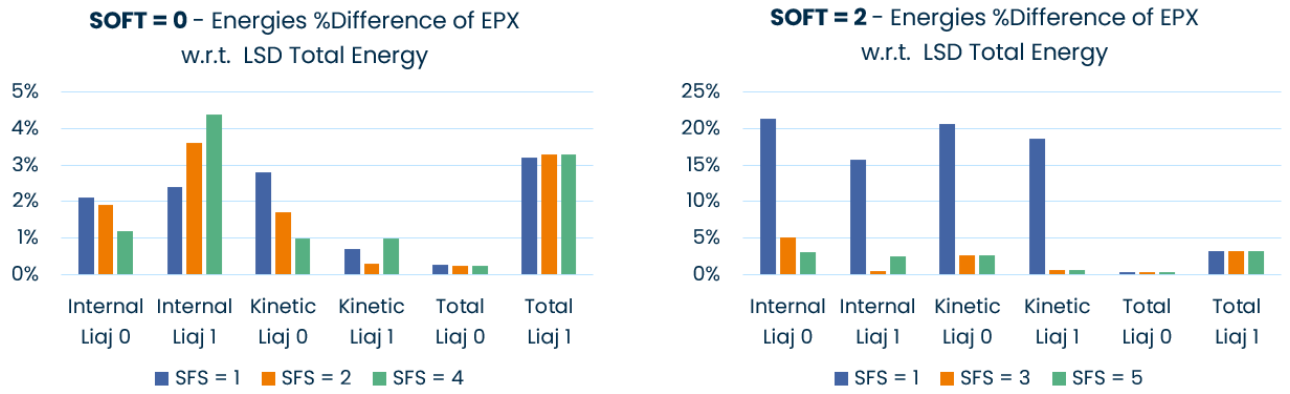


*Table 2.9 – Histogram %Difference btw EPX and LSD total energy for SOFT = 0 and SOFT = 2*

From the histograms, it is well appreciable the discrepancy between the default SOFT = 2 configuration (SFS = 1) and the reference Liaj 0. On the other hand, increasing the stiffness of the contact between the tube and the rigid barrier, the percentage difference between the two software is close to zero for all the evaluated configurations. This consideration is in accordance with what has been said in the previous section, so that contacts with higher stiffness cause higher energy absorption of the system. Indeed, going from SFS = 1 to SFS = 5, for the case SOFT = 2, the percentage difference between the two software drastically decreases.

As far as SOFT = 0 is concerned, the trend of the percentage difference seems to be the same, with a progressive decrease in difference between LS-Dyna and EPX, except for the case of Liaj 1, whose results look almost divergent from LS-Dyna ones. This is justified looking at the plots that have been produced up to now, since LS-Dyna curves are convergent with the Liaj 0 contact option in EPX, both for SOFT = 0 and SOFT = 2.

## 2.3 Time Step and Added Mass analysis

A connection between contact stiffness and time step has been already illustrated in section 1.2.2 through Equation 1.4. On the basis of this relation between time step and contact stiffness, it is expected that scaling the stiffness through the variation of the SFS parameters would lead to a variation of the time step as well. This could lead again to time instants in which the current time step would be lower than the critical one. As it was explained in section 1.2.4, to prevent this to occur, the code adds some mass to the system, causing a variation in energies and momentum.

### 2.3.1 Influence of Contact Penalty Formulation and SFS on Time Step

Similarly to what has been done up to now, a sensitivity analysis, varying the Contact Formulation and the SFS parameters, has been performed, in order to understand how much the time step is influenced by these variations. The plan for this analysis is always referred to Table 2.5 in the previous section 2.2.1.

**Time step – SOFT = 0**

Figure 2.12 illustrates the behaviour of the time step size, increasing the Stiffness Scale Factors, as it was done previously with energies and momentum.

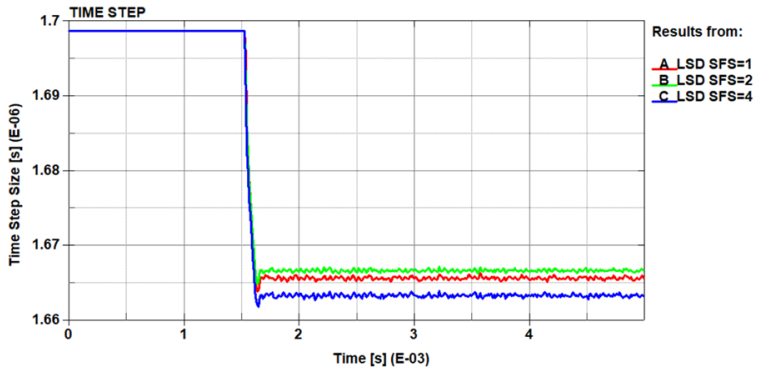


***Figure 2.12*** *– Time history plot of time step size for SOFT = 0*

The variation of the time step depends on the variation of the characteristic length of the shell element, computed as in Equation 2.1, and related to the time step through Equation 2.2:

$$L_c = \frac{2A}{\max side} \tag{2.1}$$

***Equation 2.1*** *– Characteristic length of the shell element*

Where $A$ is the area of the shell element and $max\ side$ is the maximum side length of the shell element.

$$\Delta t_e = \frac{L_c}{c} \tag{2.2}$$

***Equation 2.2*** *– Time step calculation for shell elements*

In Equation 2.2, $L_c$ is the characteristic length computed in Equation 2.1, while $c$ is the sound of speed, constant for definition.

The trend of the time step size in Figure 2.12 can be justified thanks to the following implications:

- Before the contact occurs, all the three curves are overlapped, since the time step is equal.
- After the contact occurs, a decrease of the time step can be appreciated while increasing the contact stiffness. This is due to the higher penalty force applied to the penetrating nodes, which implies a higher length of the maximum side of the shell element, and consequently a lower characteristic length. The decrease of the time step is also justified by the consequent increase of the internal energy of the system, which is a measure of the deformation of the system itself.
- Being the tube made of an elasto-plastic material, it permanently deforms, so after the time step drops, it stabilizes around a lower value than that one before the impact with the barrier.

**Time step – SOFT = 2**

The same procedure has been repeated varying the contact formulation to SOFT = 2, and the corresponding results are shown in Figure 2.13.

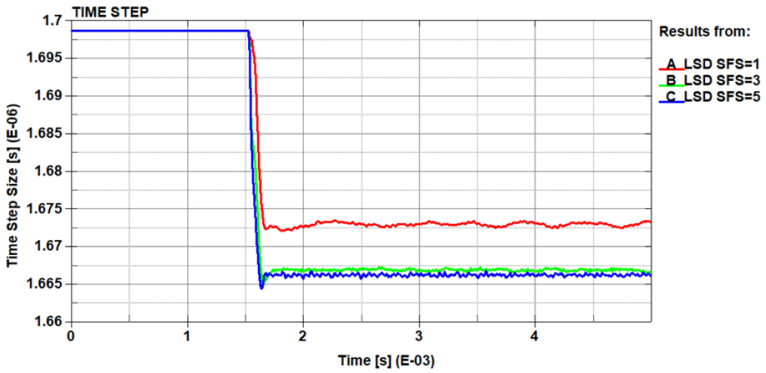


*Figure 2.13 – Time history plot of time step size for SOFT = 2*

The curves show a trend that is practically the same of the previous case with the Standard Penalty Formulation. It is worth underlining the trend of the red curve, corresponding to SFS = 1, which is unsuitable for this case study, as it was demonstrated in the previous sections. Indeed, increasing the contact stiffness, the elements will deform more, causing a higher length of the maximum side of the element and a consequent lower time step mean value after the impact with respect to the other curves.

### 2.3.2 Influence of "fixed" Time Step on results

Sometimes, it could be useful to "fix" the time step to a preset value. If the code detects time instants in which the element time step falls below this preset threshold, then it restores the time step of those elements to this limit value. In doing this, the code adds some mass to the penetrating nodes involved in the contact if the parameter *DT2MS* has been defined, as it was described in section 1.2.4.

It will be deeply explained that for this case of study the chosen value is equal to $\mathbf{-1.9e-06}$. This value is apparently negative, as it has been stated previously. Clearly, just the magnitude of this value is considered.

Obviously, setting a fixed value of time step causes a variation of all the results that have been analysed so far, as it will be shown hereafter. For this reason, it is worth showing the influence that the setting of this parameter has on the results.

### Internal Energy – SOFT = 0

Figure 2.14 shows how the fixed time step influences the internal energy, together with the variation of the SFS parameters.

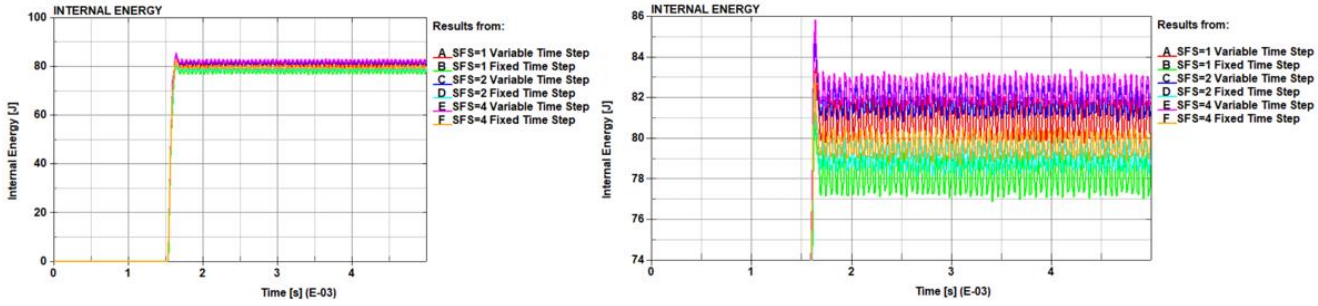


*Figure 2.14 – Time history plots of internal energy for fixed and variable TS and SOFT = 0*

As it is visible from the zoomed plot of Figure 2.14, the influence of the variation of the time step is evident. A consistent drop of the energy absorption capability of the system is visible when the time step is limited to a threshold value – at the same SFS factor – with respect to the variable time step case. This drop can be appreciated, for instance, from the blue and the light blue curves, which identify respectively the case of variable and fixed time step, for SFS = 2.

### Kinetic Energy – SOFT = 0

The trend of variation of the kinetic energy, differently from the internal one, is not so evident, with the curves that overlap one to each other, as it is shown in Figure 2.15.

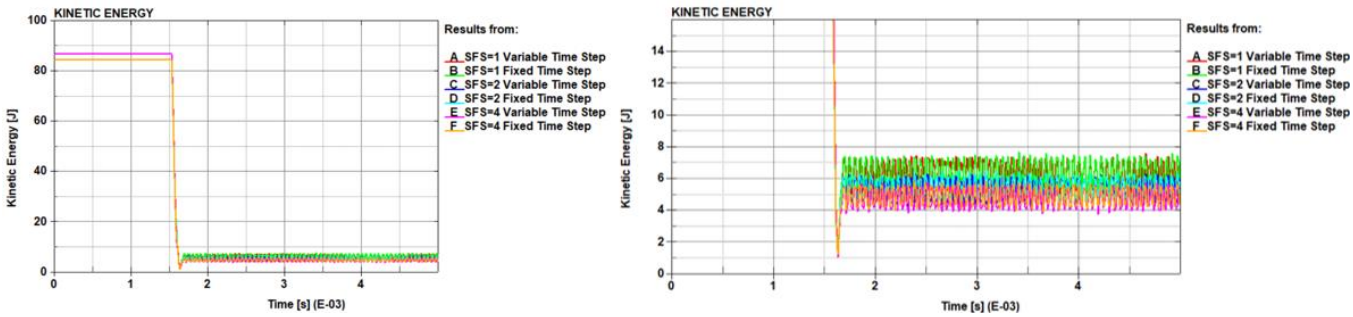


*Figure 2.15 – Time history plots of kinetic energy for fixed and variable TS and SOFT = 0*

The only noticeable difference here is that the initial value of the kinetic energy is not the same for fixed and variable time step cases. This could be due to some mass added by the code to the tube before the contact occurs, since the limit value that has been chosen for the *DT2MS* parameter is slightly higher than the found threshold, below which the code does not add mass to the system. The reason behind this choice will be better clarified in a dedicated section afterwards.

### Z Momentum – SOFT = 0

The Z momentum instead, shows the behaviour illustrated in Figure 2.16. Here the curves with variable time step shows slight oscillations, while the curves relative to the fixed time step are practically settled to a constant value.

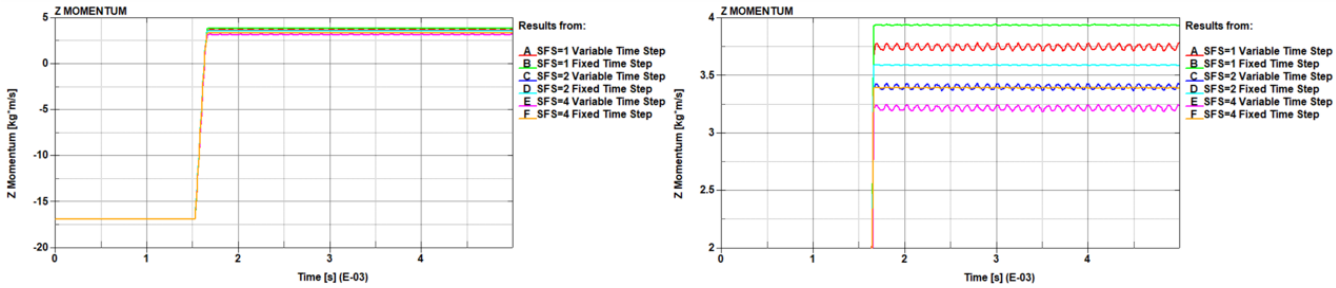


***Figure 2.16*** *– Time history plots of Z momentum for fixed and variable TS and SOFT = 0*

Here again, due to the increasing added mass for higher SFS, it is noticeable an increase of the momentum for all the three analysed cases.

### Internal energy – SOFT = 2

As it was for the case of SOFT = 0 contact formulation, as far as the internal energy is concerned, we have a greater energy absorption capability of the system and a consequently more deformed tube, with the curves shifted up for the "fixed" time step case, at the same SFS parameter, as it is shown in Figure 2.17.

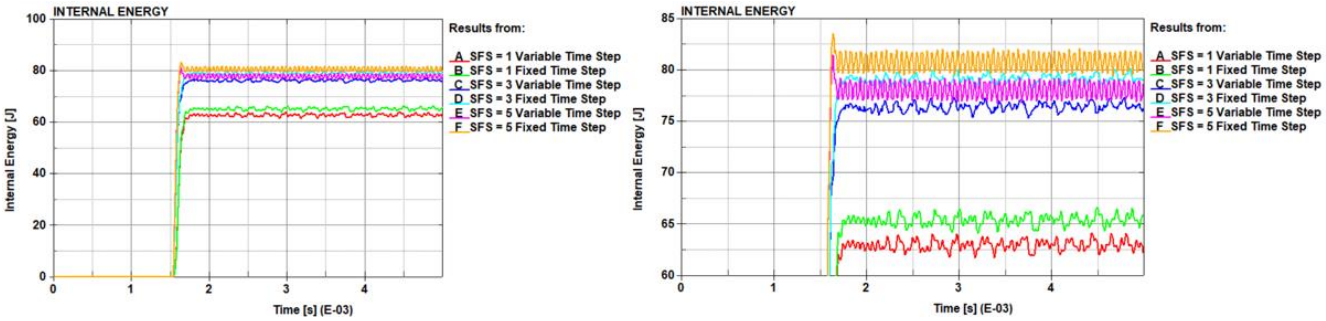


***Figure 2.17*** *– Time history plots of internal energy for fixed and variable TS and SOFT = 2*

It is clear as well that the variation of the time step size does not influence the trend of the curves, which remain unchanged.

### Kinetic energy – SOFT = 2

Also in this case, the kinetic energies are quite overlapped, with very slight variations with respect to the case of "variable" time step.

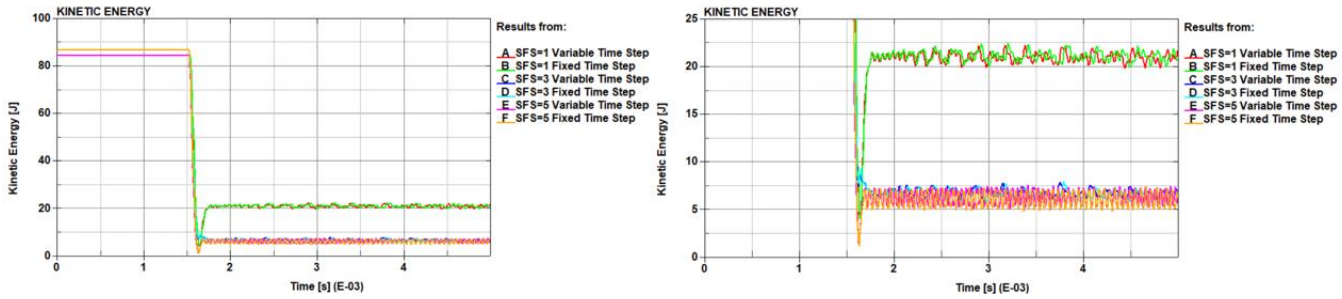


***Figure 2.18** – Time history plots of kinetic energy for fixed and variable TS and SOFT = 2*

Figure 2.18 shows the consistency that has been seen so far. Moreover, the curves of fixed and variable time step for SFS = 1 are not overlapped to the others, showing again that this contact stiffness, with the current contact formulation, does not fit this model, as in the previous cases.

### Z Momentum – SOFT = 2

Figure 2.19 shows instead a decrease in the Z momentum passing from "variable" to "fixed" time step, on the contrary to what it is appreciable in the other contact formulation.

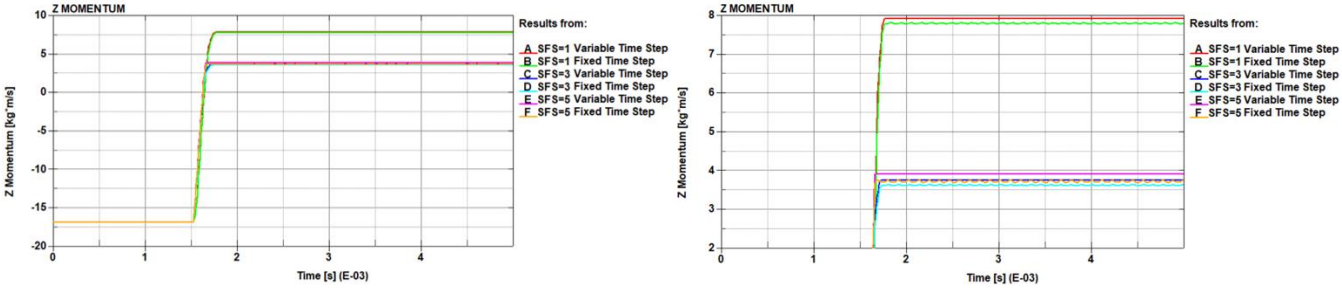


***Figure 2.19** – Time history plots of Z momentum for fixed and variable TS and SOFT = 2*

However, the overall trend of the curves remains the same of the previous case, with a higher value for less stiff contacts, which could be due to a higher velocity of the tube after the impact with the barrier. A not so evident discrepancy is instead appreciable for the other cases.

### 2.3.3 Influence of Time Step, SFS and Contact Penalty on Added Mass

The setup of the "fixed" time step is directly related to the definition of added mass, which has been provided in detail in section 1.2.4.

The analysis that has been performed on the added mass consists of an iterative process, able to find a threshold value of the parameter *DT2MS*, below which no mass is added to the system. Following this procedure, a limit value of the time step size, equal to $0.9 * \mathbf{1.85\ e-06} = 1.665\ e-$

$06\ s$ has been found, where 0.9 is a scale safety factor to prevent instability of the system and $1.85e-06$ is the *DT2MS* parameter.

In this section, the influence on the added mass behaviour of all the parameters, used to perform the sensitivity analyses so far, will be investigated.

**Added mass – SOFT = 0**

As explained in section 1.2.4, it is important that the highest value of added mass does not exceed the 5% of the total mass of the tube. For sake of completeness, the total mass of the tube is equal to $1.69\ kg$. It has to be underlined that mass is added just in case of fixed time step, mainly to the penetrating nodes of the lower half of the tube, whose time step falls below the provided threshold.

Table 2.10 illustrates the percentage value of the added mass in the three cases of SFS parameters, with respect to the total mass of the tube.

| ***SFS*** | *%Added mass FIXED time step* |
|---|---|
| ***1*** | 3.8% |
| ***2*** | 3.8% |
| ***4*** | 3.8% |

***Table 2.10*** *– %Added mass w.r.t. total mass of the tube for SOFT = 0*

Figure 2.20 instead, graphically shows the parts where the mass is added by the code, with two different modes of visualization.

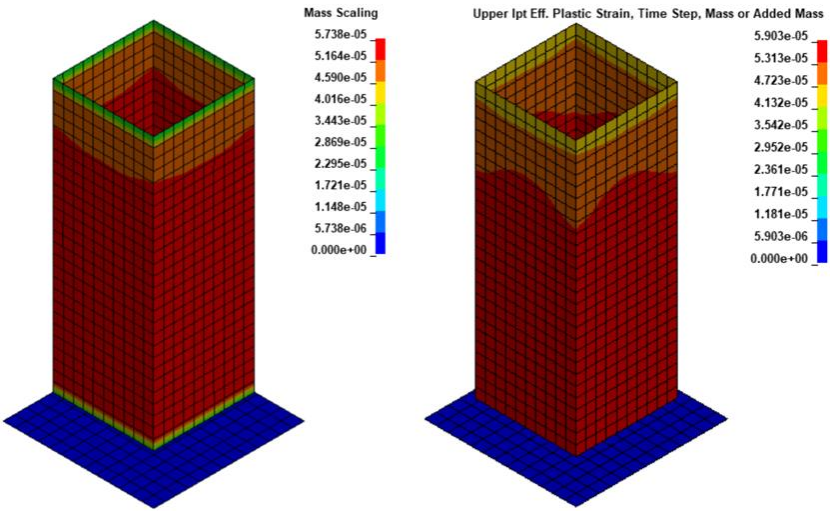


***Figure 2.20*** *– Added mass per node (left) and per element (right)*

In particular, the added mass *per node* is minimum in the upper and lower edges of the tube, while it is maximum just above the bottom border. The added mass *per element* instead is maximum on the elements of the lower edge that impacts with the barrier, while it is minimum on the upper

edge, which is not involved in the contact.

Figure 2.21 shows the trend of the added mass as a function of the increasing SFS parameters for the contact stiffness.

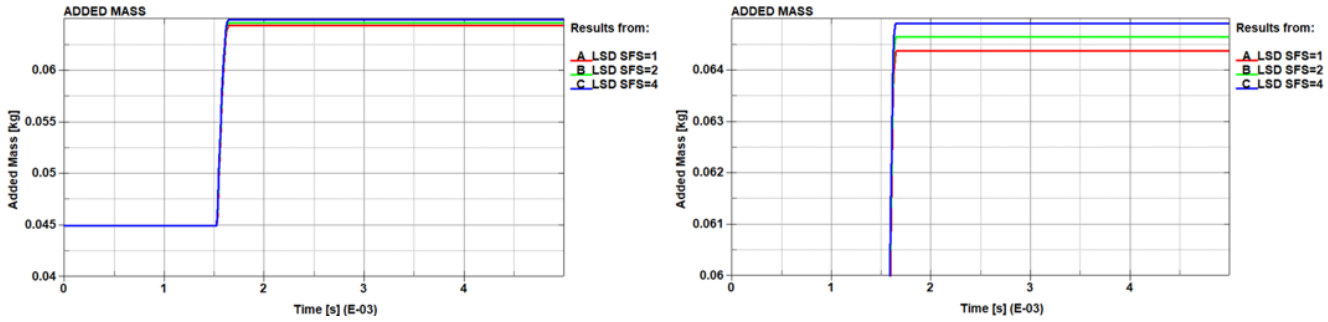


***Figure 2.21*** *– Time history plots of added mass for fixed TS and SOFT = 0*

As it is visible from Figure 2.21, increasing the contact stiffness, the mass added to the system increases as well. This increasing trend of the added mass justifies the decreasing trend of the time step for higher contact stiffness. Indeed, when the contact time step becomes lower, for stiffer contacts, the elements need to be adjusted with a higher added mass, in order to restore their time step value to the chosen threshold.

Moreover, from the left plot of Figure 2.21, it is visible that the code adds mass to the tube also before the impact, and this is due to the fact that the time step threshold that has been used is slightly higher than the one found with the iterative procedure, below which no mass is added to the system. The used value corresponds to $0.9 * \mathbf{1.90\,e-06} = 1.71\,e-06\,s$, since it has been observed that this choice prevented some variabilities of the results.

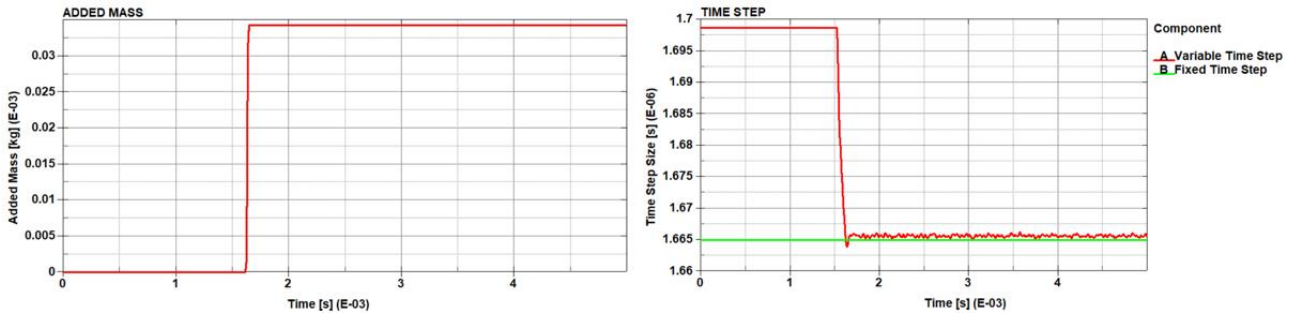


***Figure 2.22*** *– Time history plots of AM and comparison btw fixed and variable TS for SOFT = 0*

The left plot of Figure 2.22 shows the added mass computation for the value of $DT2MS = 1.85e-06$, in fact any mass is added to the system before the impact between parts occurs. The right plot instead, related to the time step, shows the discrepancy between the threshold value, found with the iterative procedure described before, and the time step trend when no limitations are used. Here, considering the order of magnitude of the plot, the difference between the two values is contained in a very narrow interval. Nevertheless, it is substantial to provoke important results variations with respect to the cases of "variable" time step.

### Added mass – SOFT = 2

When SOFT = 2, the trend of the added mass is the same as it was for the previous case, as it is shown in Figure 2.23.

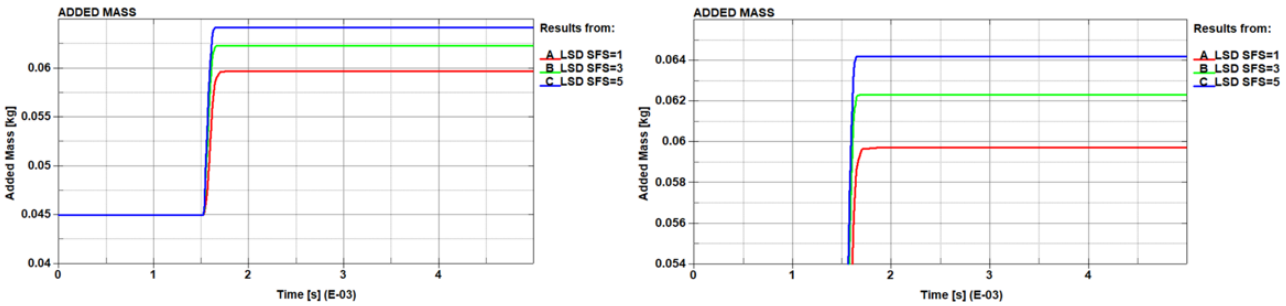


***Figure 2.23*** *– Time history plots of added mass for fixed TS and SOFT = 2*

The shifting up of the curves is more evident than the previous contact formulation, but the trend is coherent with what has been said up to now. Also the percentage of added mass is lower than the 5% of the mass of the tube, as it is shown in Table 2.11.

| ***SFS*** | *%Added mass FIXED time step* |
|---|---|
| ***1*** | 3.5% |
| ***3*** | 3.7% |
| ***5*** | 3.8% |

***Table 2.11*** *– %Added mass w.r.t. total mass of the tube for SOFT = 2*

Again, the percentages are similar to the previous ones, so the mass added to the system does not cause any type of instability or uncertainty of the final results, in terms of energies and momentum.

## 2.3.4 Influence of Contact Penalty Formulation and SFS on Contact Energy

As deeply explained in section 1.2.3, the contact energy is fundamental to understand if there are compenetrating elements during the contact between the two parts. As it has been clarified, it should not be negative and for cases not including friction, it has to be null, or lower than the 10% of the internal energy of the system.

### Net Contact Energy – SOFT = 0

Figure 2.24 shows the influence of the contact formulation, rather than that one of the SFS parameters, on the net contact energy, with respect to the threshold value, represented by the 10% of the internal energy.

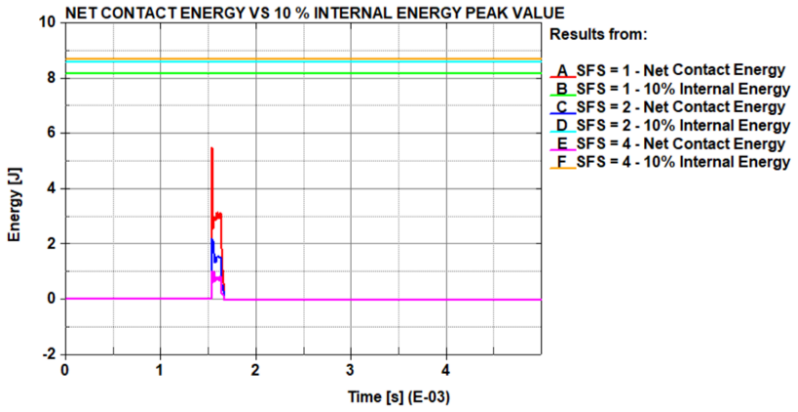


***Figure 2.24*** *– Time history plot of contact energy w.r.t. 10% of internal energy for SOFT = 0*

The first point to highlight here is that the contact energy is not negative, so there are no compenetrating elements involved in the contact. Moreover, making the contact stiffer, the highest peak of the contact energy becomes lower, never overcoming the limit value of 10% of the internal energy.

| ***SFS*** | *%Peak value of the Net Contact Energy w.r.t. Internal Energy peak value* |
|---|---|
| ***1*** | 6.7% |
| ***2*** | 2.6% |
| ***4*** | 1.2% |

***Table 2.12*** *– %Peak value of contact energy w.r.t. total internal energy for SOFT = 0*

Table 2.12 highlights the percentage value of the contact energy peaks with respect to the internal energy of the system. These percentages decrease while increasing the SFS value, meaning that for stiffer contacts, the net contact energy becomes closer to the 10% of the internal energy.

### Net Contact Energy – SOFT = 2

Changing the contact penalty formulation, the values of contact energy arise. This condition indeed was expected since it has been demonstrated in this chapter that this contact formulation does not fit the numerical problem for low stiffness contacts. Figure 2.25 illustrates the trend of the contact energy for the three different cases of SFS parameters.

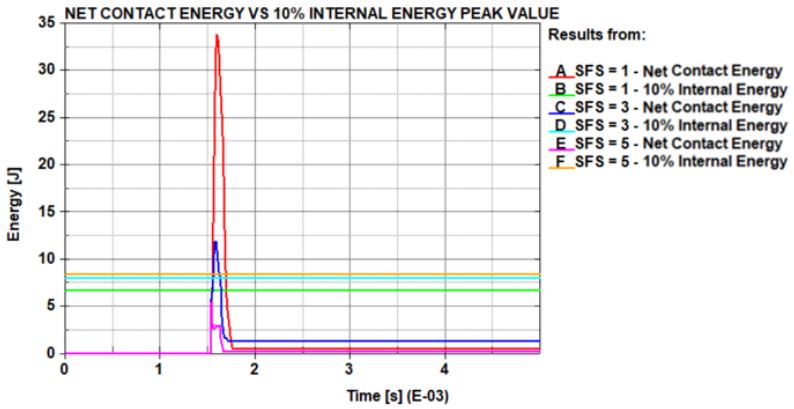


***Figure 2.25*** *– Time history plot of contact energy w.r.t. 10% of internal energy for SOFT = 2*

It is clearly visible that low stiffness contacts do not respect the threshold value of 10% of the corresponding internal energy, in accordance with the results obtained up to now, while the case of SFS = 5 is instead compliant with this limit. Nevertheless, no compenetrating elements are detected since any negative value appears in the plot of Figure 2.25.

Again, in Table 2.13, the percentage values of the contact energy peaks, with respect to the internal energy, are listed.

| ***SFS*** | *%Peak value of the Net Contact Energy w.r.t. Internal Energy peak value* |
|---|---|
| ***1*** | 52.3% |
| ***2*** | 15% |
| ***4*** | 6.7% |

***Table 2.13*** *– %Peak value of contact energy w.r.t. total internal energy for SOFT = 2*

It is evident that the case of SFS = 1, for the contact formulation SOFT = 2, is not suitable for this application, since it presents several criticalities, as far as the contact between the tube and the barrier is concerned. These criticalities can be appreciated in the representation of the deformed state of the tube, in Figure 2.26, showing a comparison between the two contact options with the same SFS = 1.

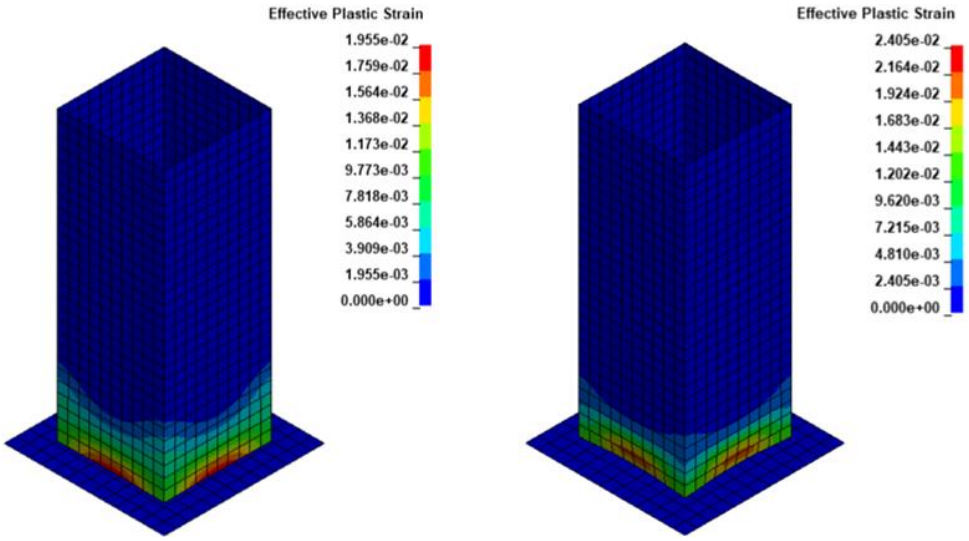


***Figure 2.26*** *– Effective plastic strain for SOFT = 0 (left) and SOFT = 2 (right) with SFS = 1*

For SOFT = 2, the deformation of the tube is higher than for SOFT = 0, after the contact with the barrier. This leads to instability of the results, as it has been shown and deeply explained up to now.

## 2.4 Case of study conclusions

Considering all the cases that have been analysed so far, it is worth noting that, even in LS-Dyna there are several factors that influence the results, such as the contact formulation, the contact stiffness, rather than the time step. Here, the value of contact stiffness heavily influences the quality of the results, and these differences can be appreciated also in those extracted from EPX. Scaling the stiffness, it was possible to get closer to the Liaj 0 contact option, which corresponds to the case of infinite stiffness.

It has been noted that the contact formulation SOFT = 2 was not suitable for this case of study, since it provided unreliable results in terms of contact energy, overcoming the limit of the 10% of the total internal energy of the system.

In conclusion, it can be stated that this case of study strongly depends on several parameters that influenced the oscillating trend of the plots. Anyway, regarding the hypothesis of solver independence that has been done at the beginning of this work, it can be affirmed that the overall behaviour of the results was satisfactory, and this assumption will also be verified in other cases of study that will be analysed later on, in order to establish a benchmark between LS-Dyna and EPX.

# Chapter 3. Tube shock-crush analysis

In this section, a tube impacting against a rigid barrier, and crushed from the top by an added mass distributed on the nodes, will be analysed. As it was done before, the same model has been tested in EPX in order to understand the differences between the two software. The results that will be compared are the energy components – i.e. internal and kinetic – rather than the momentum along the vertical direction and the velocity of the mass added on the top border nodes of the tube.

Here, this case can be considered as a strong simplification of a vehicle beam, and the objective is also to verify how it behaves during a possible accident, and how good this beam is in terms of energy absorption capability, to absorb the energy of that crash.

## 3.1 Model and contact setup: Tube, Rigid Barrier and Added Mass

**Model setup**

The model that will be analysed, shown in Figure 3.1, is composed by:

- A *tube*, with a particular section, in order to provide a direction to the folds, made of a *plastic deformable steel*.
- A *rigid barrier*, made of *rigid steel*, with the same material characteristic of the tube.
- An *added mass*, evenly distributed on the top nodes of the tube, which is responsible of the folding behaviour of the tube itself.

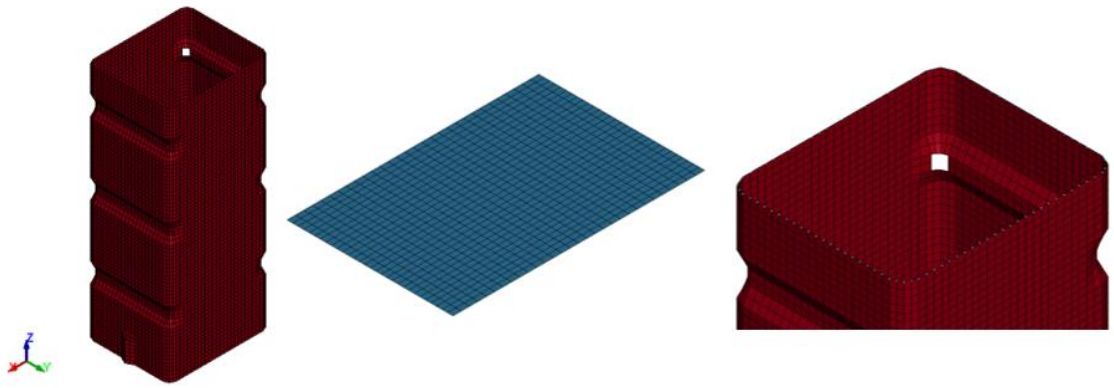

***Figure 3.1*** *– Tube, rigid barrier and added mass model representation*

For this case of study, the material of the tube has been modelled with the card *024_PIECEWISE_LINEAR_PLASTICITY,* behaving as a *plastic deformable steel* with the same characteristics shown in Table 2.1 and Figure 2.2 of the previous Chapter 2.

The material of the barrier instead has been set to be a *rigid steel*, using the card *020_RIGID*, with the characteristics shown in Table 3.1 below.

Again, like in Chapter 2, the material used to model the two parts is the same, exception made

for their density, adjusted to set the mass of the two parts, and for their behaviour.

More in detail, a mass of 80 $kg$ has been evenly distributed among the nodes of the top border of the tube, shown in Figure 3.1. Having 104 nodes on the top border, the distributed mass on each single node will be $0.76925\,kg$. This added mass has been configured using the card *ELEMENT_MASS_NODE_SET*. Different cards could have been used to configurate this added mass, like *RIGIDWALL_PLANAR_MOVING_FORCES*, but it will be demonstrated later on that this solution heavily influences the results, so that the condition of same tested model for the two software would not been satisfied.

| ***PARAMETER*** | *SYMBOL* | *VALUE* |
|---|---|---|
| ***YOUNG'S MODULUS*** | $E\ (MPa)$ | 200000 |
| ***POISSON'S RATIO*** | $\nu\ (-)$ | 0.3 |
| ***DENSITY*** | $\rho\ (kg/\mathrm{m}^3)$ | 476190.476 |

***Table 3.1*** *– Rigid steel parameters*

As far as the shell elements of the two parts are concerned, they have different dimensions and thickness, as indicated in Table 3.2. In particular, the plate is realized using rectangular elements, differently for the squared elements of the tube, in order not to have critical responses of the code when the two parts come in contact.

| ***PART*** | *MESH SIZE (mm)* | *SHELL THICKNESS (mm)* |
|---|---|---|
| ***TUBE*** | 4 | 2 |
| ***RIGID BARRIER*** | $4\ x\ 6$ | 20 |

***Table 3.2*** *– Mesh size and shell elements thickness of the two parts*

It is important to underline that this high value of thickness for the plate could be suitable just because it is modelled as non-deformable, so that this thickness will not cause deformation effects, otherwise it should not fit the definition of shell element.

Differently from the case of study of Chapter 2, the element formulation has been set equal for the two parts, using the *Fully Integrated Shell Element Formulation* (ELFORM = 16) for two main reasons:

- The elements are very deformed since the tube is crushed down by the added mass.
- It is not necessary to save computational cost and effort because the model is not so heavy in terms of complexity, otherwise it would have been effective to use ELFORM = 2.

A deeper analysis on the influence of the element formulation on the results will be anyway performed in the following sections.

Regarding boundary conditions, the top and bottom node sets of the tube have been constrained with the card **NODAL_RIGID_BODY*, in order not to be allowed to move in other

direction than Z, as it is shown in Figure 3.2. This time, an initial velocity of $-10\ m/s$ is applied to the top added mass towards the Z direction, while a velocity of $5\ m/s$ is applied to the bottom added plate, in order to crush the tube from the bottom. The duration of the simulation has been set to $20\ ms$, so that a crushing of the tube of $100\ mm$ is expected.

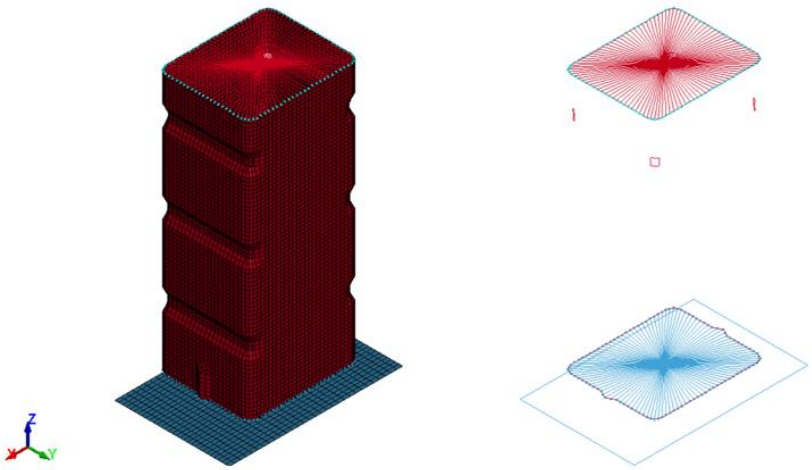

***Figure 3.2*** *– Nodal rigid body representation for top and bottom node sets*

These constraints allow to track the added mass velocity, taking one node of the top border, as it will be shown in the following sections.

**Contact setup**

Due to the presence of the top added mass, the card **AUTOMATIC_SURFACE_TO_SURFACE* is not sufficient to setup all the contacts in this model, so it is necessary to use the card **AUTOMATIC_SINGLE_SURFACE* as well, in order to define the auto-contact of the tube, as it was stated in the dedicated section 1.2.1.

The contact penalty formulations used for this case of study, for both contact cards, are the following ones:

- **SOFT 0**: Standard Penalty Formulation
- **SOFT 2**: Segment-based (Pinball) Contact Penalty Formulation

Even if it will be demonstrated that varying the contact formulation will not influence the results, and as a consequence, only the SOFT = 0 contact algorithm will be used for the comparison purpose of this analysis, while SOFT = 2 will be deeply studied in another work.

For each of the contact formulations, the results will be compared to the ones obtained in EPX, varying the SFS parameters from 1 to 4, as it will be better explained in the Table 3.3, which lists the test plan, in the following sections.

For this case of study, neither static nor dynamic friction will be considered, so the surfaces that come in contact are free to slide one with respect to the other.

## 3.2 Results and comparison with EPX

From now on, the results obtained in LS-Dyna will be compared with those obtained in EPX, as it has been done in the previous Chapter 2, regarding the *tube shock* analysis, in terms of internal and kinetic energies, rather than momentum along the Z axis and velocity of the top added mass along the Z direction. This will be done in order to check again the consistency between the two codes, which use the same model to test.

As it has been done for the previous case of study, a preliminary calculation has been performed, with the Standard Contact Penalty Formulation (SOFT = 0) and default contact stiffness (SFS = 1), to check if the overall trend of the results is coherent. These results are shown in Figure 3.3.

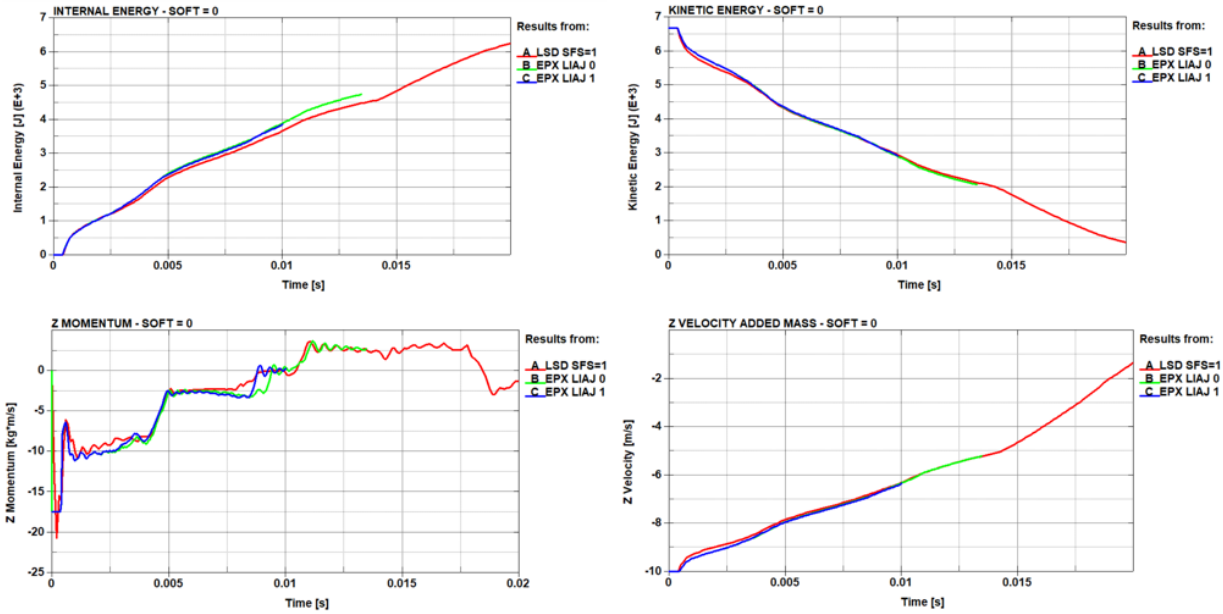


*Figure 3.3 – Preliminary results comparison of tube shock-crush with SOFT = 0*

As it is clearly visible, the results are already well coherent one with each other, with the only clearly visible difference in the Z momentum plot. It is worth noting that EPX results, for both contact options Liaj 0 and Liaj 1, experienced convergence problems, so that it was not possible to run simulations up to 20 $ms$, as it was done for LS-Dyna calculations. Indeed, in the following analyses, all the plots will be zoomed up to 10 $ms$, in order to check the trends of the curves, using the same simulation time.

### 3.2.1 Influence of Contact Penalty Formulation and SFS

In this section, the influence of the contact parameters – i.e. contact algorithm and contact stiffness – will be analysed. In this case of study, it is expected that scaling the contact stiffness between the tube and the rigid plate would not have a huge impact on the results, as it was for the tube shock case, because the shock is not the main event of the simulation, so that the crush is predominant.

Moreover, only the SOFT = 0 contact formulation will be analysed, since, as it will be shown

afterwards, even the variation of the contact algorithm will not produce noticeable differences in all the results, so that just the standard penalty formulation will be deeply analysed.

The following Table 3.3 shows the plan of the analysis, with the values of the SFS parameters that will be investigated.

| ***CONTACT PENALTY FORMULATION*** | *SFS VARIATION* | | |
|---|---|---|---|
| ***SOFT = 0*** | 1 | 2 | 4 |
| ***SOFT = 2*** | 1 | – | – |

***Table 3.3*** *– Plan of the analysis on SFS factors*

It can be noticed that the plan is similar to that one used in Chapter 2 for the tube shock analysis, since it is expected that the trend of the results will always be coherent with the previous case of study. Nevertheless, as it was stated before, for the Pinball Contact Formulation (SOFT = 2), only the default value of the contact stiffness will be tested, since it will be proven that results are not significantly influenced by this variation.

**Internal Energy – SOFT = 0**

The following Figure 3.4 shows the plot of the internal energy of the system, for each stiffness scale factor that has been listed in Table 3.3, with a zoomed view on the right.

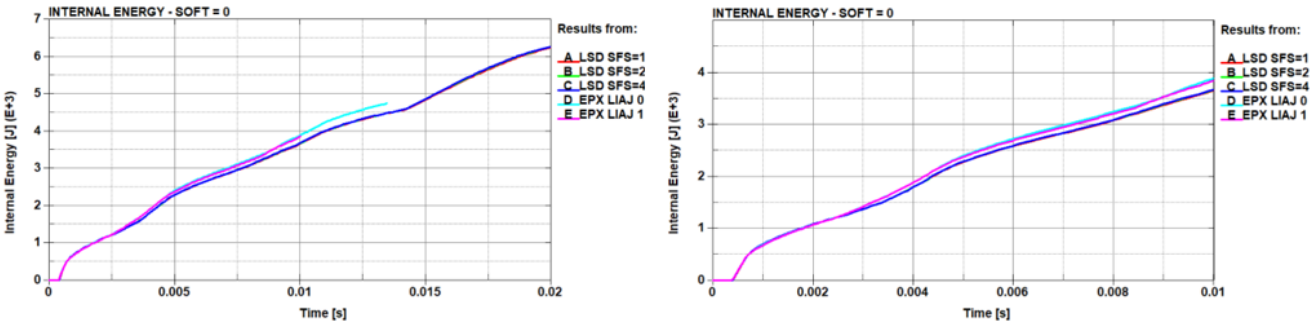


***Figure 3.4*** *– Time history plots of internal energy with SOFT = 0*

At first sight, it is worth affirming that the zoomed view of the plot has been made between 0 $ms$ and 10 $ms$, due to a convergence issue of the EPX solver. Indeed, it is visible on the left plot of Figure 3.4 that the duration of simulations is even different between Liaj 0 and Liaj 1 – i.e. 13.5 $ms$ and 10 $ms$. So, in order to produce a reliable comparison between the two software, this zoomed view has been used for the other results too.

Differently from the previous case of study, the variation of the SFS parameters seems to have a not so heavy influence on the results, since the curves obtained in LS-Dyna are practically overlapped one with each other. Nevertheless, also the curves representing the two contact options of EPX are well coherent.

### Kinetic Energy – SOFT = 0

The considerations done for the internal energy hold also for the kinetic energy, since it has a specular trend. As it was said in the previous case of study, before the impact all the energy of the system is kinetic. When the impact between the tube and the added plate occurs, the energy content of the system starts to become internal, as the tube deforms when crushed down by the top added mass. Figure 3.5 shows the comparison in terms of kinetic energy content of the system.

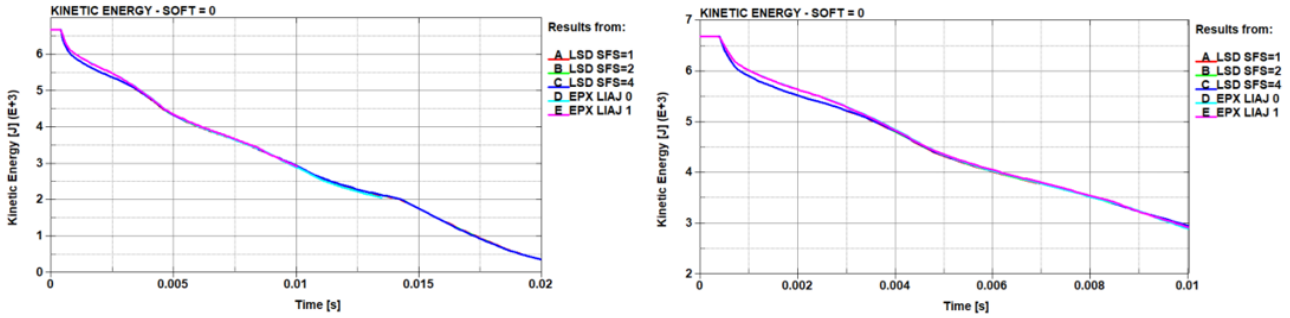


*Figure 3.5 – Time history plots of kinetic energy with SOFT = 0*

The trend of the kinetic energy shows an even more overlapping behaviour of the five curves, confirming the coherence between the results. As it is visible, the impact between the tube and the added plate occurs after about 4 $ms$, noticeable from the flat trend of the curves from the beginning of the simulation to that time instant.

### Z Momentum – SOFT = 0

As far as the Z momentum is concerned, the most evident difference between results is visible, as it is shown in Figure 3.6.

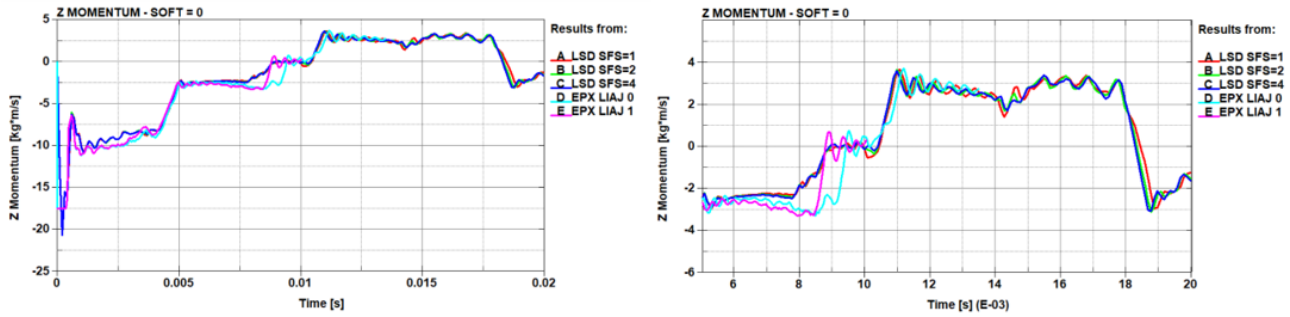


*Figure 3.6 – Time history plots of Z momentum with SOFT = 0*

Apart from the other results, the plot of the Z momentum has been zoomed between 5 $ms$ and 20 $ms$, since the clearest difference between the curves obtained in LS-Dyna can be appreciated into this time interval. Nevertheless, the Z momentum plot is the only one in which clear evidence of the influence of the contact stiffness scaling on the results is present.

Moreover, it is appreciable that the first value of the momentum is different between the two software. In LS-Dyna indeed, the initial Z momentum is computed as the product between the velocity

and the mass of the elements to which this velocity is applied, apart from the added mass distributed on the nodes, as indicated in Equation 3.1.

$$\rho = \frac{m^*}{2} \cdot v = \frac{0.0242\ kg}{2} \cdot 10\ {}^{m}/_{s} = 0.121\ {}^{kg \cdot m}/_{s} \tag{3.1}$$

***Equation 3.1*** *– Initial Z momentum calculation in LS-Dyna*

In Equation 3.1, $m^*$ is the mass of the top *elements* of the tube, without the added mass on top, while $v$ is the initial velocity applied to each node. Being the initial velocity $v$ applied just on the top nodes of the elements, half of the mass of the elements has been considered. In EPX instead, the first value of the Z momentum is equal to $17.47\ kg \cdot m/s$. Clearly, all these momentum values have to be considered in negative sign, since the tube moves downward with respect to the reference coordinate system.

Generally, from $10\ ms$ onward, even if is not visible on the plots, the curve relative to Liaj 0, corresponding to the ideal case of infinite contact stiffness, appears to be consistent with the other results.

### Z Velocity Added Mass – SOFT = 0

To extract the Z velocity of the added mass, a node from the top border has been selected randomly, since the top nodes are rigidly constrained to move only toward the Z direction, and so they also have the same vertical velocity.

The comparison between the Z velocity results obtained in LS-Dyna and EPX is shown hereafter in Figure 3.7.

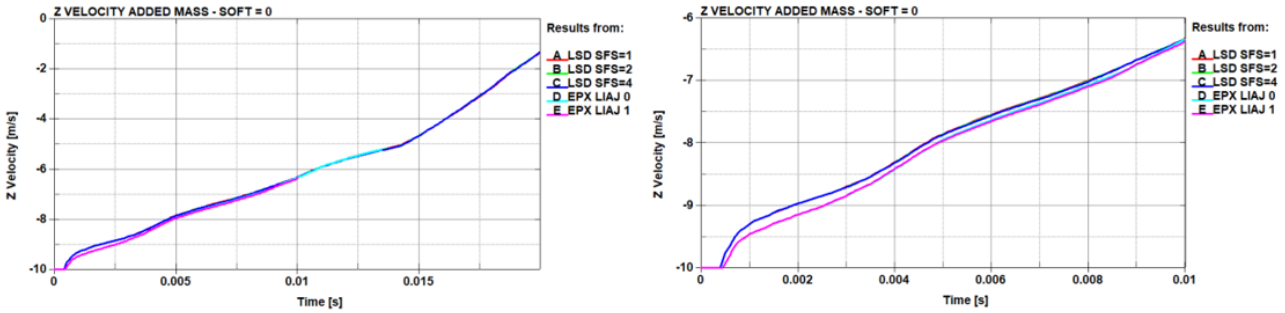


***Figure 3.7*** *– Time history plots of Z velocity of added mass with SOFT = 0*

All the curves are well coherent one with each other, also in the initial time instants, in which the vertical velocity of the added mass is constant at $-10\ m/s$, until the impact between the tube and the plate occurs at $4\ ms$. Then, after the contact, this velocity starts to decrease – in absolute value – until the end of the simulation.

### Internal Energy – SOFT = 2

By changing the contact formulation, it is expected that results do not undergo evident

changes, even between different contact stiffnesses. For this reason, Figure 3.8 puts in evidence the comparison between the curves obtained in LS-Dyna, with the two contact formulations, and those obtained in EPX, in terms of internal energy. This is done in order to demonstrate that there is any evident influence of the contact formulation on the results.

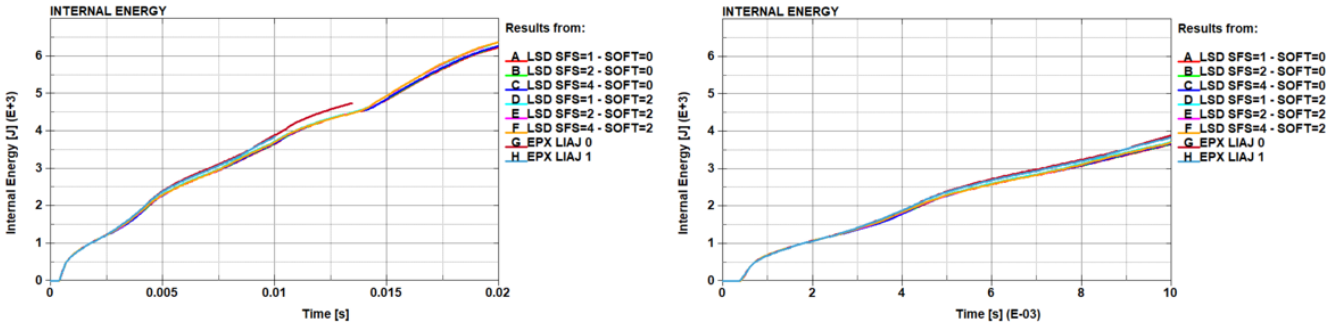


***Figure 3.8*** *– Time history plots of internal energy with SOFT = 2*

Results do not evidently change, even between contact formulations, and also between different contact stiffnesses, as it was stated for the same energy component for SOFT = 0. For this reason, it is useless to analyse results for SOFT = 2, because also the other results in terms of kinetic energy, Z momentum and Z velocity of the added mass undergo negligible variations between contact formulations, letting this different analysis to another work.

### 3.2.2 Influence of Added Mass configuration: Rigid Wall and Mass Node Set

As it was specified in the introductory section of this Chapter 3, the added mass on top of the tube can be set using two different types of card:

- *ELEMENT_MASS_NODE_SET*
- *RIGIDWALL_PLANAR_MOVING_FORCES*

If the first setup has been deeply studied up to this point, now it is useful to understand if a different configuration of the added mass has an influence on all the results. For this first case, only the contact for SOFT = 0 and with the default contact stiffness – i.e. SFS = 1 – will be investigated.

#### Internal Energy

Figure 3.9 shows the comparison between the two solutions of added mass in LS-Dyna, together with the reference curves of EPX.

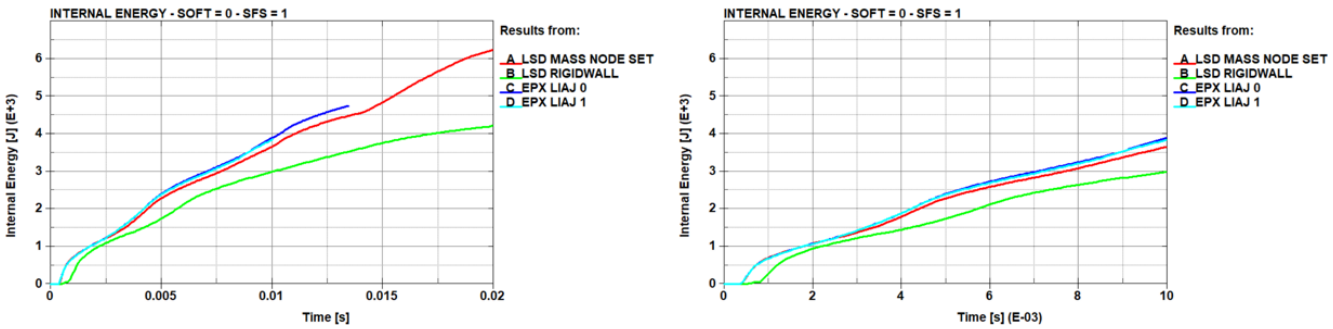


***Figure 3.9*** *– Time history plots of internal energy comparison btw added mass configurations*

The difference between the curves is well appreciable, with the green one, relative to the *RIGIDWALL* configuration, which seems to be completely misleading with respect to the other ones. This is certainly an indication that perhaps this configuration is not very comparable with the model setup of EPX, since it appears to be distant from the curves relative to Liaj 0 and Liaj 1.

This leads to the conclusion that this added mass setup provokes a completely different deformation mechanism, and moreover, a less deformed tube too, as the highest value of the internal energy of the green curve is much lower than the highest value of the red curve, relative to the **MASS_NODE_SET* configuration.

## Kinetic Energy

As expected, kinetic energy should have a specular trend of the internal one, with a rapid decrease after the impact, when the tube is completely and permanently deformed.

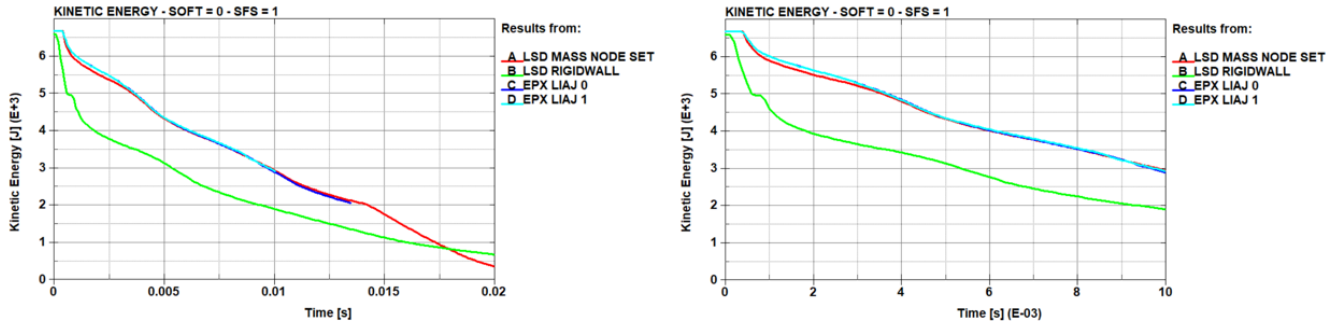


***Figure 3.10*** *– Time history plots of kinetic energy comparison btw added mass configurations*

As it was for the internal energy, Figure 3.10 shows that the kinetic energy not only has a different trend, but also it is not specular with respect to the internal one. This could be due to the fact that other energy components play a not negligible role in the system energy balance with this configuration. However, these components have not been analysed so far, and so they will not be considered in this case neither.

## Z Momentum

Figure 3.11 illustrates instead the comparison in terms of Z momentum of the tube, highlighting even more differences of the results, in terms of initial momentum and oscillatory trend.

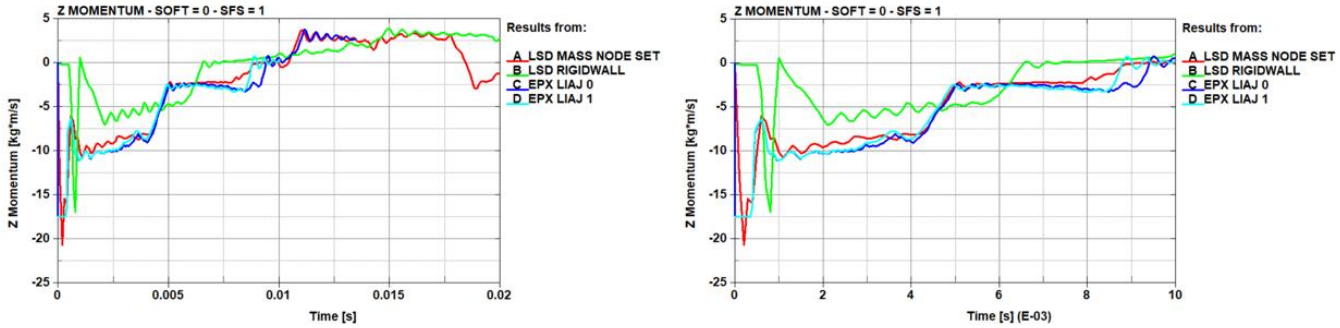


***Figure 3.11*** *– Time history plots of Z momentum comparison btw added mass configurations*

Here, the unsuitability of the *RIGIDWALL* configuration is clearly visible. If the first value of the Z momentum is equal, with the *RIGIDWALL* configuration there is not the same drop of the red curve, perhaps due to a small gap existing between the planar moving wall and the top border of the tube, since the drop occurs after about 0.5 $ms$. Apart from that, the overall trend of the curve, if compared to the red curve of the **MASS_NODE_SET* configuration is almost the same.

## Z Velocity Added Mass

Provided that there is a gap between the planar moving wall and the top border of the tube, substantial differences in the Z velocity plot are expected as well.

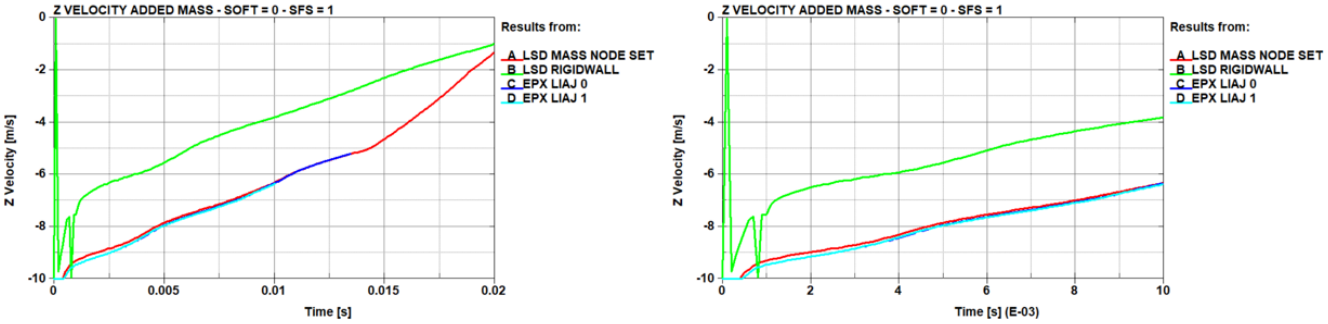


***Figure 3.12*** *– Time history plots of Z velocity comparison btw added mass configurations*

The completely different behaviour of the green curve shown in Figure 3.12, noticeable in the first 1.5 $ms$, is certainly due to this gap, present between the planar force wall and the tube. Nevertheless, the tube is first impacted by the added plate from below, and only after it is crushed down by the rigid wall, originating these sudden changes in sign of the Z velocity of the top border.

In conclusion, this added mass configuration is not suitable for this case of study, since it is not representative of the model tested in EPX. For this reason, this configuration does not fit the goal of this analysis and will not be considered anymore.

### 3.2.3 Influence of Contact Penalty Formulation on Plastic Deformation

More visible differences between the two software calculations are present in the plastic deformation that the tube undergoes during different time instants of the simulation. For sake of completeness, it is worth highlighting that only results without scaled contact stiffness will be shown, since any evident deviation between results has been appreciated during the whole analysis.

Figure 3.13 and Figure 3.14 show the plastic deformation of the tube, caught at $5\,ms$ and $10\,ms$, compared to the deformation seen in EPX.

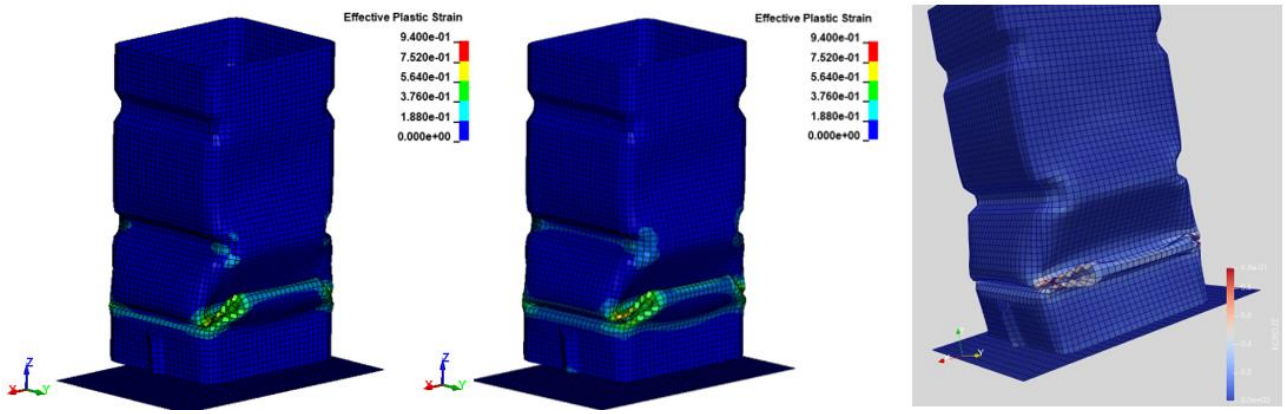


***Figure 3.13*** *– Plastic deformation of tubes at 5 ms for SOFT = 0 (left) and SOFT = 2 (right)*

Visually, it can be immediately appreciated that the formation of the folds follows a completely different path in LS-Dyna with respect to EPX. This effect becomes even more evident when the tube continues to crush down, pushed by the top added mass.

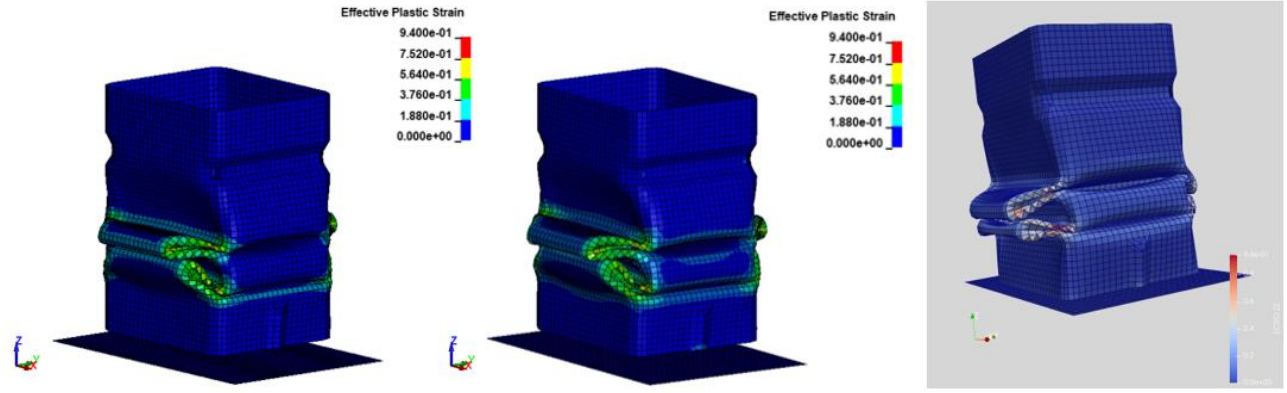


***Figure 3.14*** *– Plastic deformation of tubes at 10 ms for SOFT = 0 (left) and SOFT = 2 (right)*

Apart from the magnitude of the plastic strain, which seems to be consistent between the three pictures, the fold mechanism appears to be completely different, with a more upward inclination for the LS-Dyna results, compared to the tube used in EPX simulations.

### 3.2.4 Influence of Shell Element Formulation

As it was said in the previous chapter, the shell element formulation has a great influence on the results. To this purpose, in order to demonstrate this influence, a deeper analysis on the element

formulation has been performed for this case of study. Provided that a variation of the contact stiffness, as it has been shown in the previous sections, does not have an appreciable impact on the results, just the default value of the stiffness will be considered throughout this analysis. Table 3.4 illustrates the plan that has been set for this investigation.

| ***CONTACT PENALTY FORMULATION*** | *ELEMENT FORMULATION* | | |
|---|---|---|---|
| ***SOFT = 0*** | 2 | 16 | −16 |
| ***SOFT = 2*** | 2 | 16 | −16 |

***Table 3.4*** *– Plan of the analysis on Element Formulation*

If ELFORM = 2 and ELFORM = 16 have already been introduced, ELFORM = –16 can be defined as a modification of ELFORM = 16, with a higher accuracy, and which can be used for very complex models, when the higher computational effort is not difficult to be managed. Generally speaking, ELFORM = 2, used by LS-Dyna by default, is suitable for very simple models, since it is a very fast calculation method. As far as ELFORM = 16 and ELFORM = –16 are concerned, they are used in very complex cases, when the deformations are expected to be high, but above all when the required computational effort is high enough, since they are very precise.

**SOFT = 0**

Figure 3.15 shows the comparison between curves relative to different element formulations, obtained in LS-Dyna, and the two curves Liaj 0 and Liaj 1 of EPX, always in terms of internal and kinetic energy, rather than Z momentum and Z velocity of the top added mass.

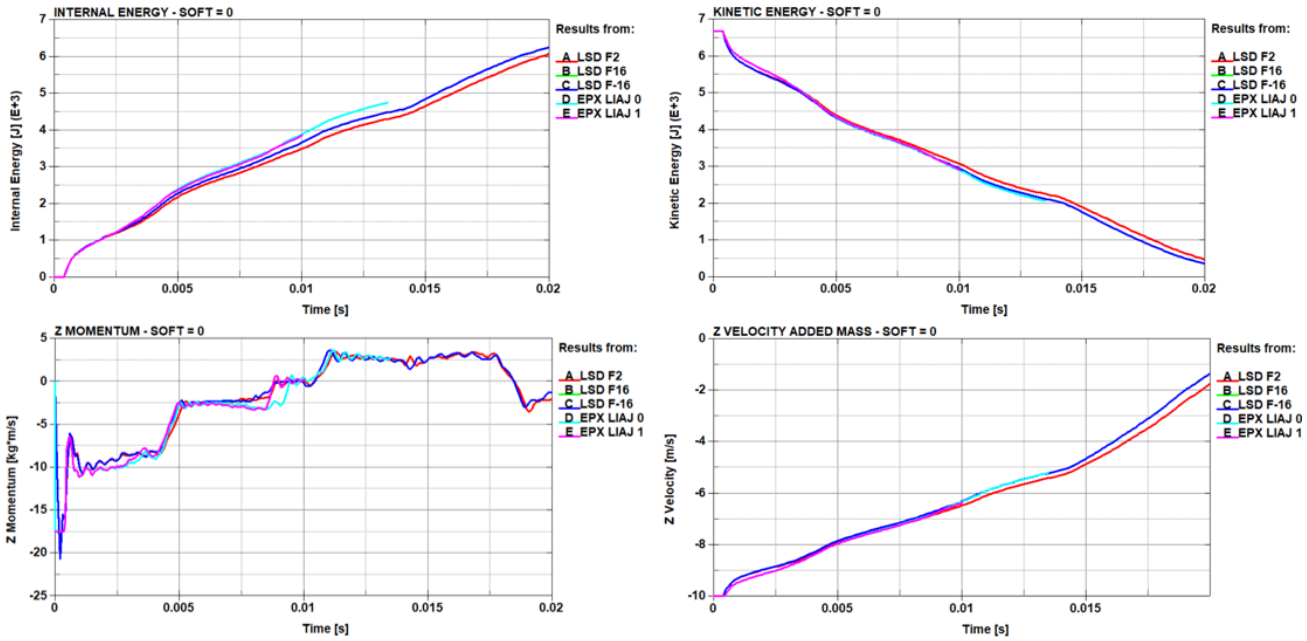


***Figure 3.15*** *– Results comparison between element formulations with SOFT = 0*

Taken ELFORM = 2 as the reference curve for this comparison, it is clearly visible that element formulation has a great impact on the results. Indeed, ELFORM = 16 seems to be more consistent with the EPX results. Nevertheless, the curve relative to ELFORM = –16 is not visible at all since it is completely overlapped to ELFORM = 16. This could be due to the relatively simple case of study that has been analysed so far, so that a higher accuracy of calculation is not necessary.

As far as SOFT = 2 is concerned, the same considerations made up to now hold, so for this reason the element formulation for this contact option will not be analysed.

## 3.3 Case of study conclusions

Having analysed all the previous cases, it can be concluded that results are quite the same, and no evident differences between the two software have been highlighted. Moreover, even the contact formulation, rather than the element formulation, does not affect the overall trend of the curves, both for LS-Dyna and EPX. In conclusion, given the same model to be studied, the behaviour of the two software can be stated coherent as well, and the scope of the analysis can be considered achieved.

# Chapter 4. N2/N3 generic vehicle model

Once a solid benchmark between EPX and LS-Dyna has been established, the aim of the work can be moved to the modelling of a real impact, in order to understand how the model of a vehicle behaves when impacting against a rigid barrier. The model to be analysed will be a generic N2/N3 vehicle, realized by SVS FEM [7] and shown in Figure 4.1.

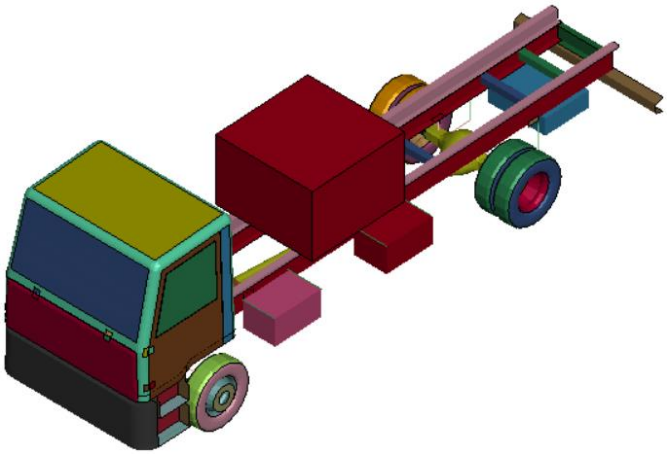

***Figure 4.1*** *– Generic N2/N3 vehicle model*

This model is defined as "generic" since it can be adapted to many cases of interest, representing several vehicle categories, of different dimensions. The adaptation can be made by manually adjusting some parameters, such as:

- Vehicle speed
- Vehicle length
- Wheelbase
- Wheel track
- Wheel dimension
- Cargo length
- Cargo position
- Vehicle mass

Acting on these parameters it is possible to obtain a wide range of vehicles, like illustrated in Figure 4.2.

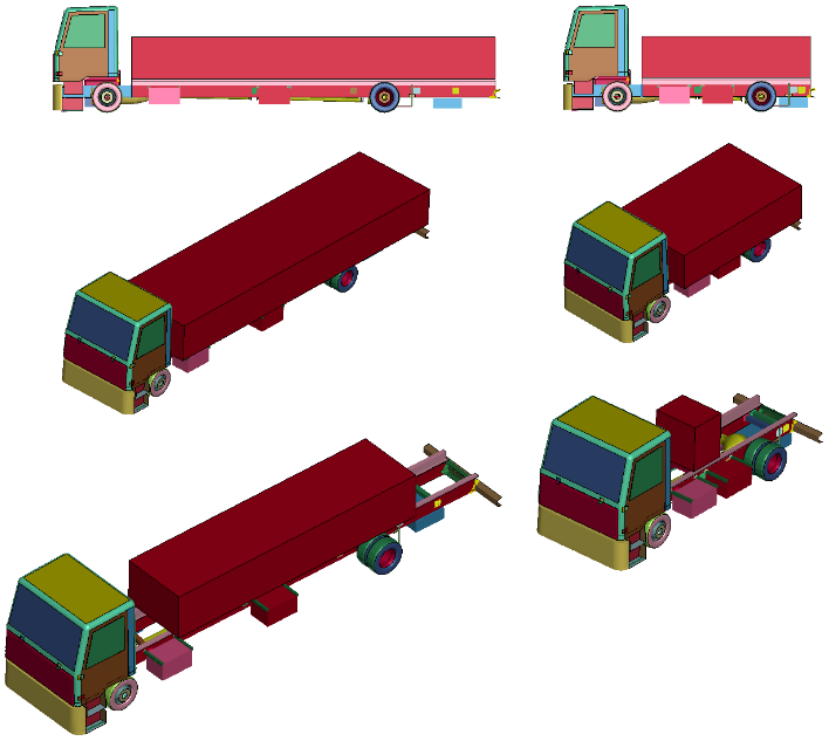

*Figure 4.2 – Different vehicle dimensions derived from the same generic model*

The boxes attached to the trailer should be representative of additional masses, such as the tank, rather than other mechanical components, rigidly connected to the trailer itself.

Proceeding in this way, it is possible to adapt the model to the experimental test of interest, validating it and then analysing the influence of some modifications on the results, like the barrier position with respect to axis of symmetry of the vehicle.

The analysis on the model will proceed with a first validation of the "generic" model, in order to understand if it is consistent and robust enough to be used for further investigations. The validation consists of a comparison with an experimental test, from which the main geometrical parameters will be extracted and set into the model. Then, with a video analyser software named *Tracker* [8], the kinematic parameters of several points of the vehicle will be obtained and compared to the results of the FEM analysis. This will confirm or deny whether the model is suitable to be used for sensitivity analyses.

## 4.1 Generic N2/N3 model validation

A validation activity on the generic model has already been performed by the SVS FEM in a dedicated report [9], but for sake of completeness, the same validation procedure has been repeated in order to have a double check whether the model is robust enough or not. The reference experimental test [10] on which the model has been validated is the following one:

- **Test Standard**: IWA 14-1:V/7200[N2A]/48/90:0.3
- **Vehicle mass**: 7200 $kg$

- **Vehicle type**: DAF LF 45 (*N2A*)
- **Vehicle speed**: 48 $km/h$
- **Angle of impact**: 90°
- **Vehicle penetration**: 0.3 $m$
- **Barrier type**: Bollard
- **Bollard dimensions**: $\phi 160\ mm \times 1000\ mm$

For this test, the vehicle is placed in front of a rigid bollard, securely fixed to the ground. Then vehicle is given the initial velocity, and the global response of the model is observed after the collision with the barrier.

The first comparison between FEM model and experimental test will be done evaluating the animations in some key time instants, to check also if there is visual consistency between the two cases.

To this scope, four different markers have been selected on the vehicle, in order to track the position of those points and to get their velocities. Then these pieces of information will be compared with the results obtained from four accelerometers, placed in the corresponding points of the vehicle model, in order to check consistency and coherence with the experimental results. The markers selected on the vehicle are shown in Figure 4.3.

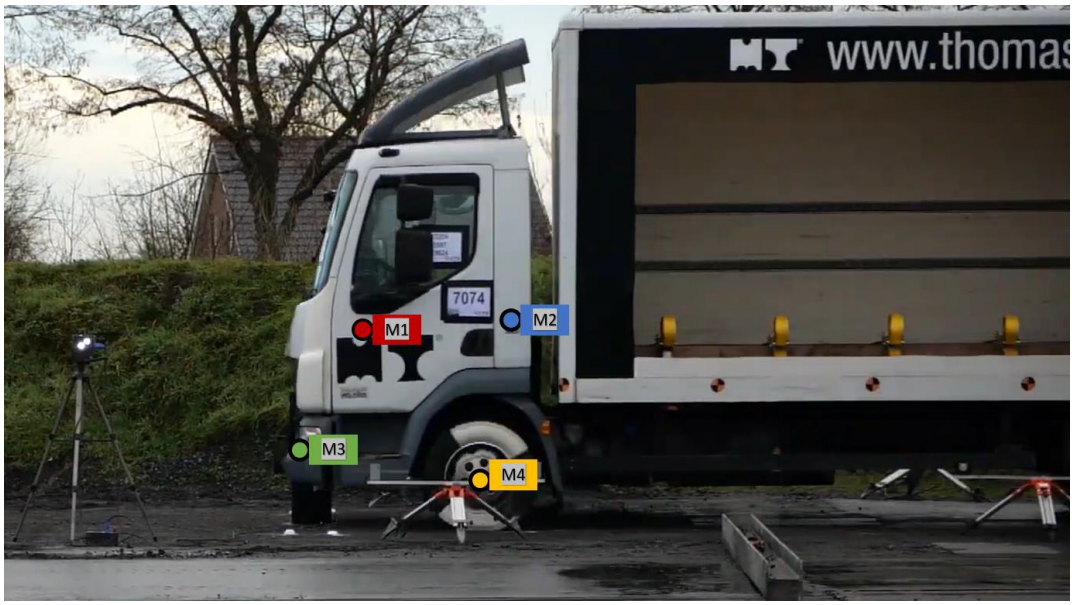


***Figure 4.3*** *– Position of the markers used to track positions and velocities*

For sake of completeness, Figure 4.4 shows instead the accelerometers positioned on the vehicle model. As far as results are concerned, the most relevant energy components, like internal or kinetic energies, will be analysed too, in order to determine whether the energy is well distributed on the whole system.

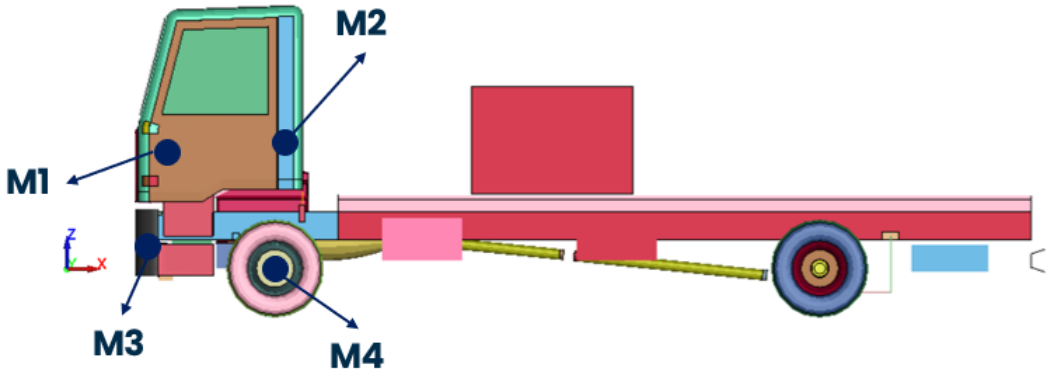


*Figure 4.4 – Position of the accelerometers used to track positions and velocities*

### 4.1.1 Animations comparison

A first check for the validation purpose could be to compare the animation obtained through the numerical calculation with the video of the experimental test, taking some important time instants to check if the FEM simulation mirrors the video of the real test. This comparison is shown in Figure 4.5 and Figure 4.6, both for side and front views of the vehicle.


*Figure 4.5 – Animations comparison front view*

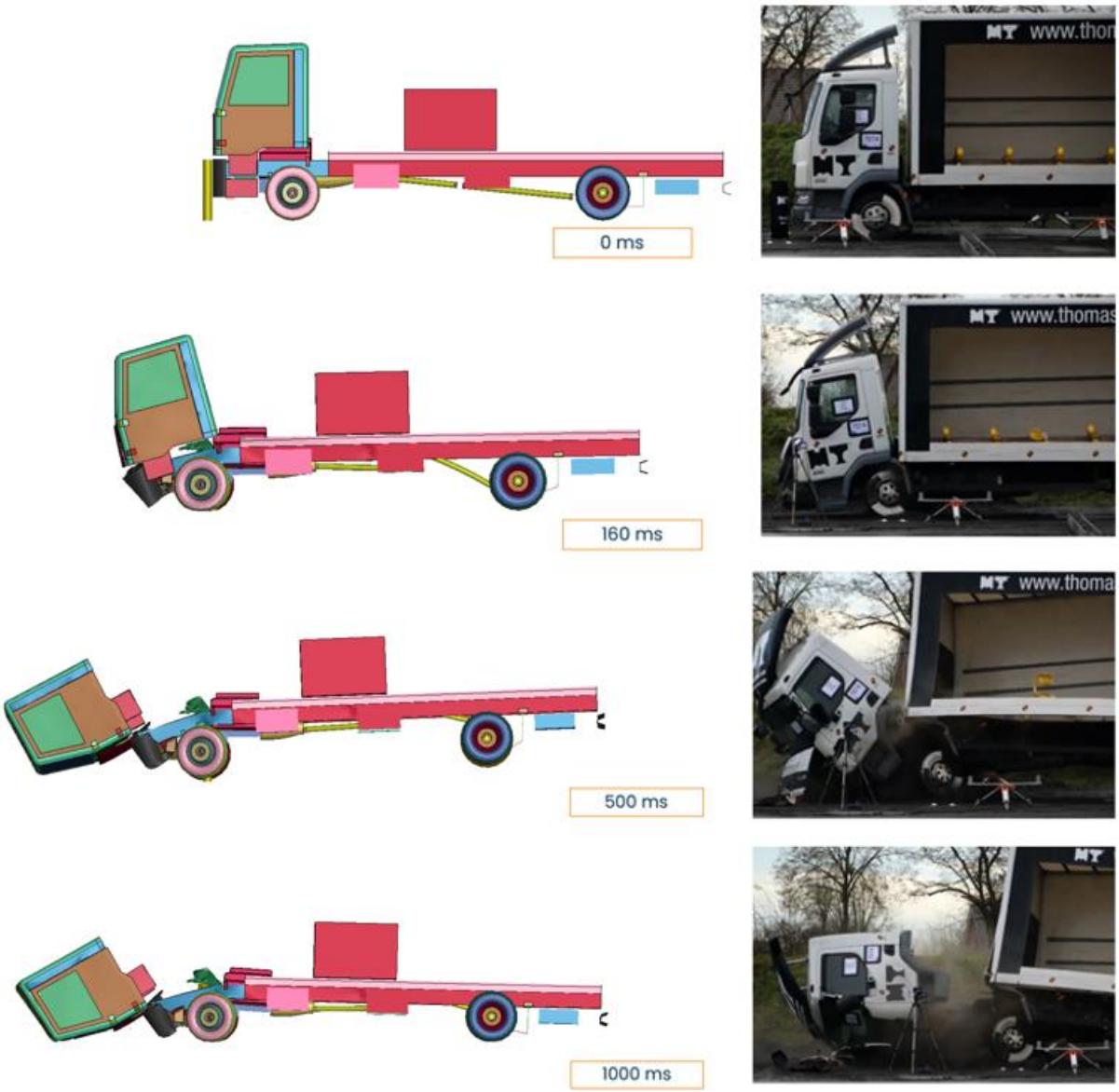


***Figure 4.6*** *– Animations comparison side view*

From the comparison between the FEM animations and the video of the real experimental test, a misalignment of the bollard with respect to the central axis of the vehicle is clearly visible since the cabin of the real vehicle points to the right after the impact with the bollard. Also for this reason, a deeper sensitivity analysis on the bollard position will be performed later on, in order to investigate whether this is the cause of asymmetry of the impact and what is the influence of this bollard misalignment on positions and velocities of the four chosen markers.

Nevertheless, to connect this analysis with the previous cases of study – i.e. tube shock and tube shock-crush – it could be useful to investigate how the vehicle model behaves when the bollard is placed in some remarkable positions, such as for instance, in front of the longitudinal beam of the frame, rather than in front of the engine. This verification will be performed in later sections.

### 4.1.2 Energy components

Since the scope of a protective barrier is to absorb the kinetic energy coming from an impact with a hostile vehicle, it is fundamental to analyse the energy distribution of the system, rather than the energy ratio, as it is illustrated in Figure 4.7 and Figure 4.8.

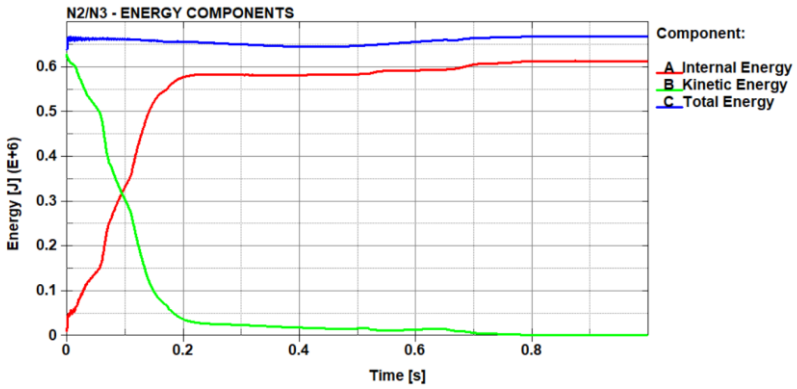


*Figure 4.7 – N2/N3 generic model energy components*

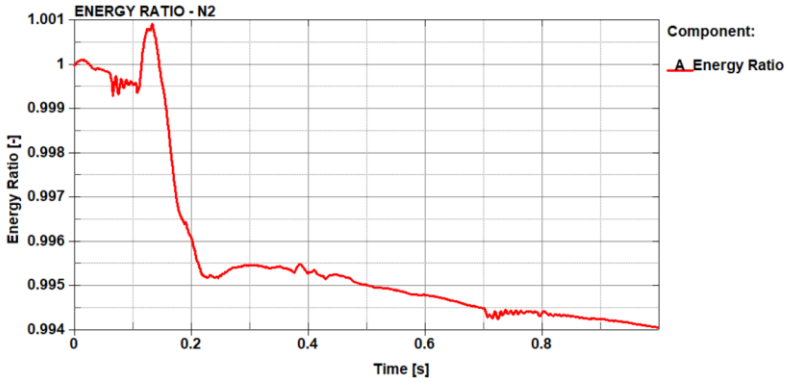


*Figure 4.8 – N2/N3 generic model energy ratio*

The energy results show a good stability of the model, since the energy ratio seems to be quite stable around the unity value. As it was expected, internal and kinetic energies are perfectly symmetric, so that the total energy is almost constant. It is worth noting that the total energy is not perfectly constant, due to some other energy components, like hourglass or sliding interface energies, which are not shown here, since they seem to be not so relevant in the system energy balance, as it was for the previous cases of study.

### 4.1.3 Kinematic parameters

The kinetic parameters, namely positions and velocities of the four selected points of interest, are directly extracted from the software *Tracker*, which has been adjusted and calibrated to the adequate unit of measurement, rather than to the real frame rate of the video, key parameter to obtain the points velocities, and above all if the video of the experimental test is time-lapsed. It is worth highlighting that velocities are extracted from Tracker using the *finite difference scheme*, which, for sake of complexity, will not be discussed in detail.

Figure 4.9 to Figure 4.12 show the comparison between the experimental test and the FEM numerical simulation, in terms of X and Z displacement of the four markers previously shown in Figure 4.3 and Figure 4.4.

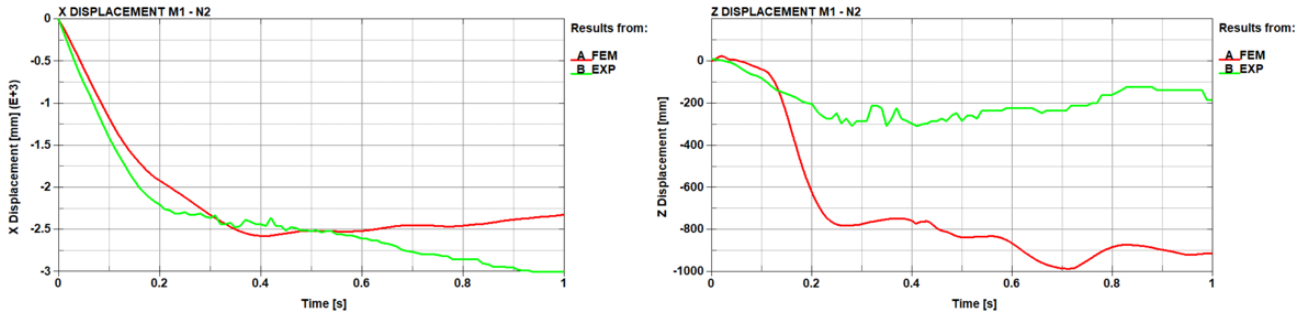


***Figure 4.9*** *– Time history plots of X and Z displacements of M1*

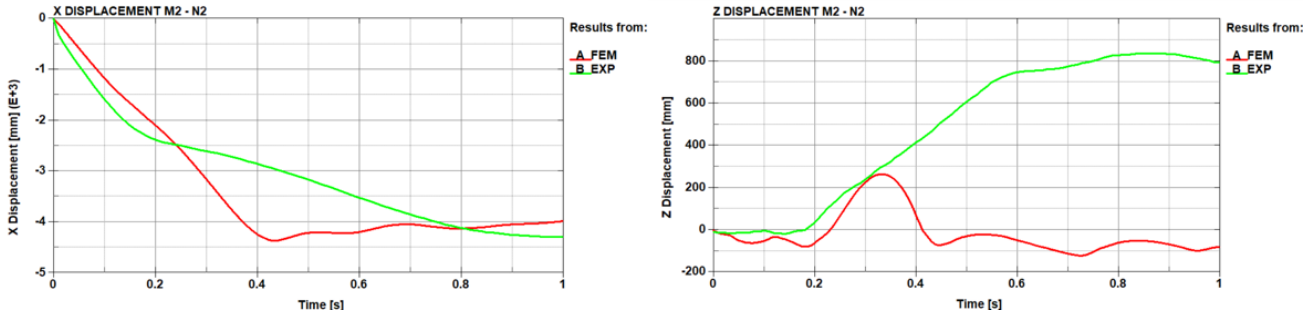


***Figure 4.10*** *– Time history plots of X and Z displacements of M2*

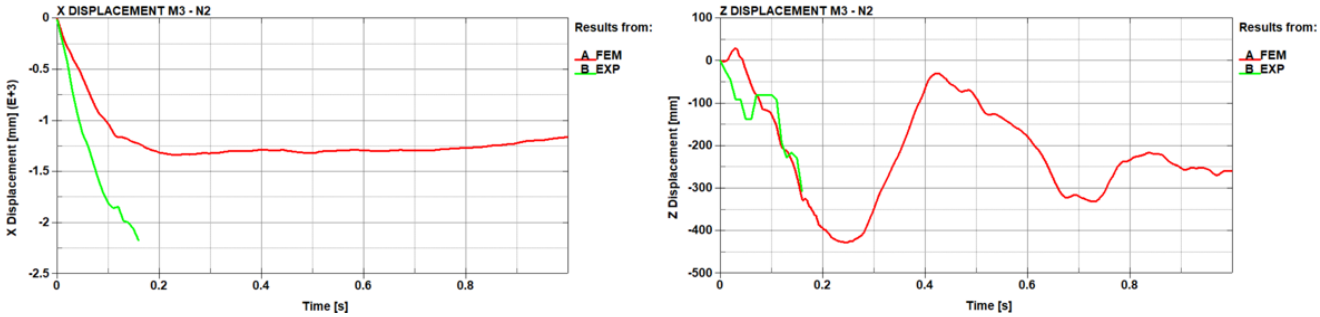


***Figure 4.11*** *– Time history plots of X and Z displacements of M3*

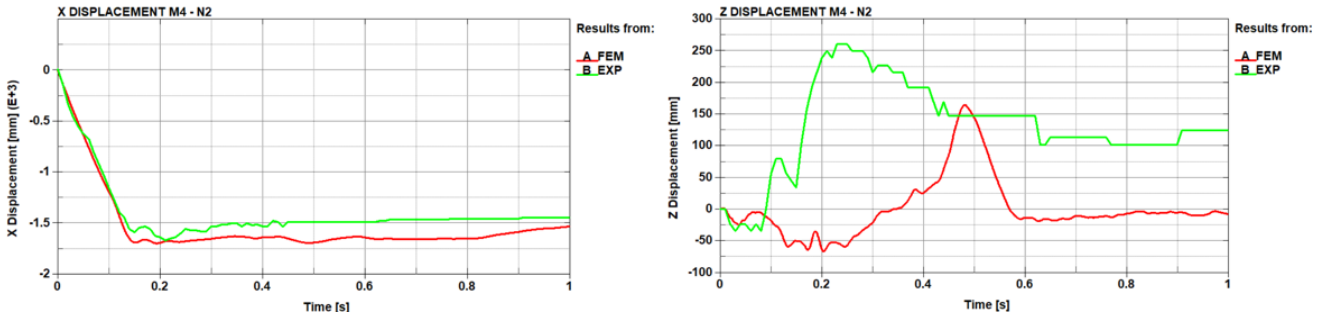


***Figure 4.12*** *– Time history plots of X and Z displacements of M4*

Looking at the plots of Figure 4.9 and Figure 4.10, it is evident that positions of the markers M1 and M2 along the Z direction are well far away from the corresponding accelerometers positioned on the vehicle model. This is certainly due to the different motion that the FEM cabin undergoes after the impact with the bollard, as it is shown in Figure 4.5 and Figure 4.6. However, the overall trends of all the curves look coherent one with each other, understanding that the model is absolutely representative of a real vehicle of the same category.

It is worth noting that positions of marker M3 are traceable only for about 200 $ms$ of the experiment, since the marker itself, located at the front bumper of the vehicle, has been destroyed after the impact. Also in this case, the trace of the positions is not completely overlapped to the FEM curves, because the movement of the front bumper looks quite different, even from the comparison between the animations.

The motion of the front axle of the model, controlled by marker M4 in the video, and located in the FEM model in the centre of rotation of the front wheel, is well overlapped to the experimental curve, as far as the X direction is concerned. Regarding the Z displacement instead, the front axle of the experimental test goes a bit more upward than the one of the numerical model.

Figure 4.13 to Figure 4.16 show instead the comparison between numerical and experimental curves related to the velocity of the four markers. The same type of analysis will be performed on the following plots.

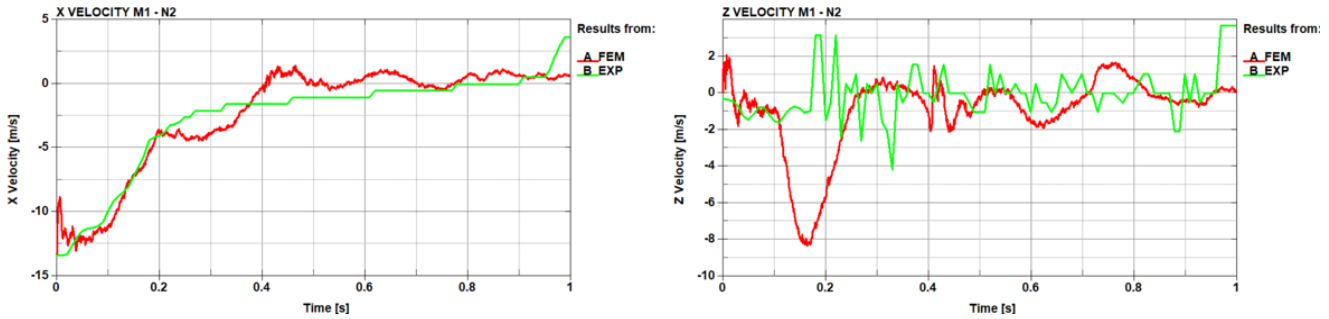


***Figure 4.13*** *– Time history plots of X and Z velocities of M1*

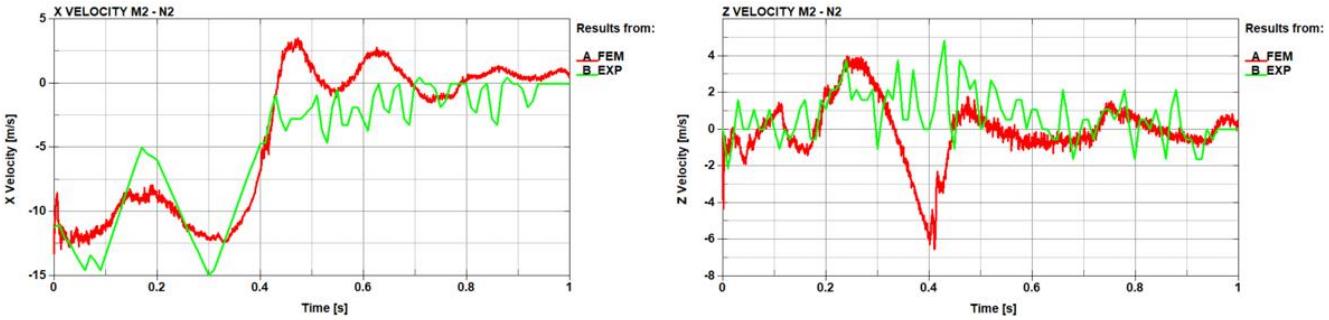


***Figure 4.14*** *– Time history plots of X and Z velocities of M2*

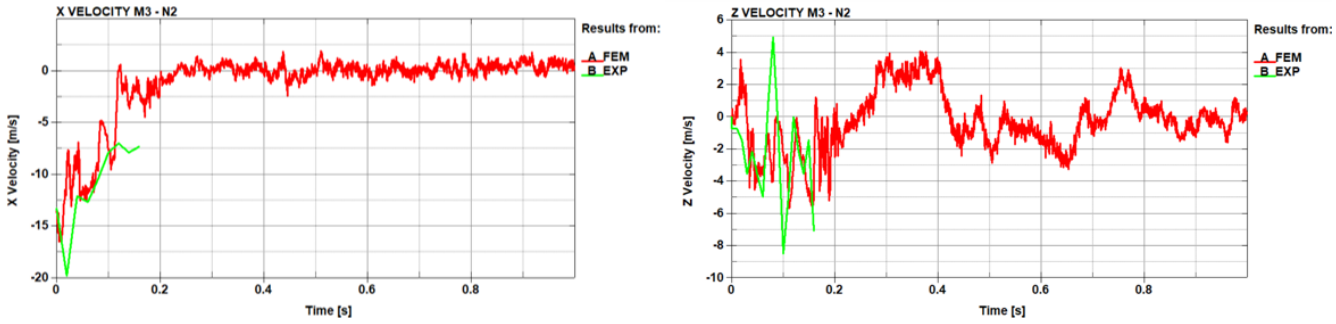


***Figure 4.15*** *– Time history plots of X and Z velocities of M3*

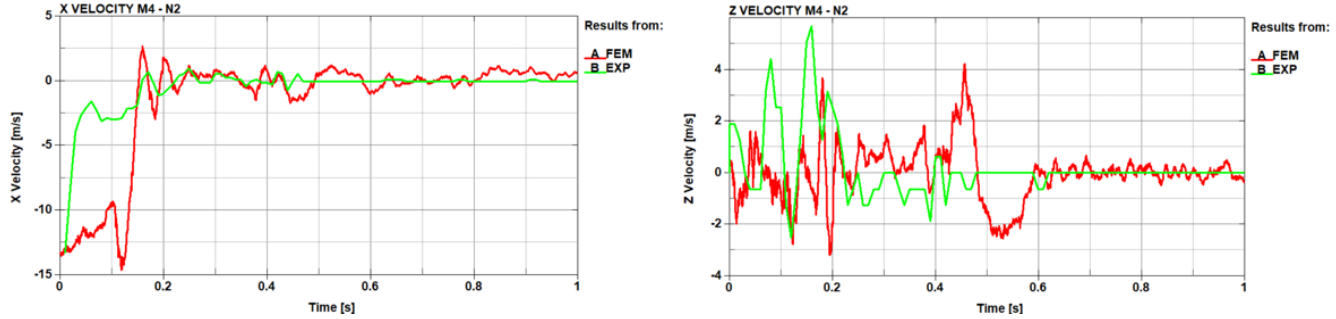


***Figure 4.16*** *– Time history plots of X and Z velocities of M4*

If compared with the displacement results, velocities seem to be in general more consistent between FEM and experimental test. In particular, markers M1 and M2, representative of the movement of the vehicle cabin, have a velocity comparable with the results obtained from the accelerometers placed on the FEM model. The only noticeable difference regards Z velocity, with a downward peak in the first 400 $ms$ for the FEM red curve, since the cabin is shattered to the ground right after the impact. Indeed, it has been appreciated that the Z displacement of M1 and M2 is very different from the correspondent accelerometers of the model because the cabin of the experimental vehicle remains stuck on the bollard.

As it was said in the section regarding displacements, it was not possible to track marker M3 after 200 $ms$, since, being positioned on the front bumper, it is destroyed after the impact. Nevertheless, up to 200 $ms$, the trend of tracked velocity seems to be coherent with the red curve, both for X and Z velocities.

As far as marker M4 is concerned, velocities of the center of the wheel front axle are coherent with the red curves. In particular, X velocity stabilises around 0 $m/s$ since the vehicle remains stuck after the impact with the bollard, and as a consequence, the front axle is completely stopped. The Z velocity trend, instead, looks similar between the two curves, with slightly higher peaks in the experimental response with respect to the FEM results. This could be due to more vertical oscillations observed in the experimental video and justified in Figure 4.12, looking at the Z displacement.

Considering the overall quality of the results, it can be rightly affirmed that the generic N2/N3 model can be considered valid and robust enough to perform further investigations. More in detail, looking at both the animations comparison and all the plots, there are sufficient differences between the experimental test, chosen to validate the model, and the FEM model itself. Even though the model has been stated as robust, a further analysis on why these differences exist can be performed.

## 4.2 Bollard position sensitivity analysis

From the analysis of the animations, it is well appreciable a not negligible asymmetrical behaviour of the experimental vehicle right after the impact with the central bollard. In particular, it is evident that the cause of this asymmetry is a non-perfect positioning of the vehicle in front of the barrier. For this reason, provided that the test is always performed with the same boundary conditions as before, different bollard positions will be tested, in order to understand the influence of this variations on the results, rather than whether this is the cause of asymmetry in the outcomes of the experimental test or not.

For sake of completeness, the positions of the bollard that will be tested are the following ones, expressed with respect to the Y axis of the coordinate reference system:

- **0 *mm***: centered with respect to the X axis
- **150 *mm***: in correspondence of ¾ of the engine
- **400 *mm***: in correspondence of the frame longitudinal beam
- **750 *mm***: between the longitudinal beam and the front right wheel

These remarkable positions are shown in Figure 4.17 below, which illustrates both the top views of the vehicle and of the frame only.

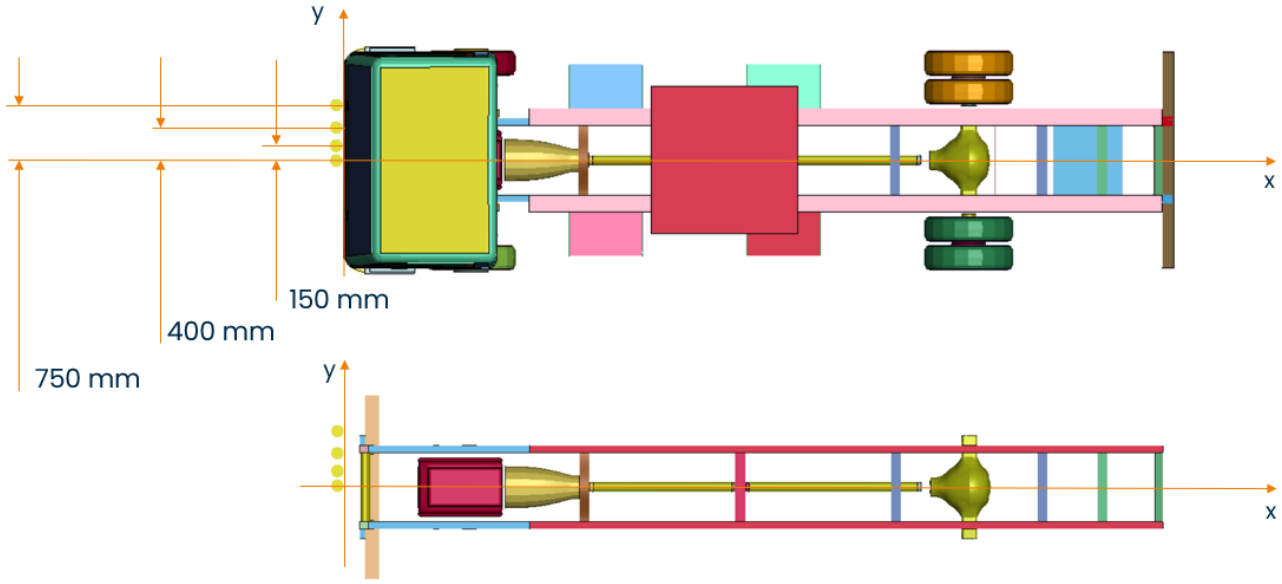


***Figure 4.17*** *– Vehicle and frame top view with bollard positions*

In particular, the frame will be analysed by its own, since it is interesting to understand how the vehicle longitudinal beams behave when crushed by the bollard, trying to connect this analysis to those performed for the tubes cases of study investigated in the previous chapters. More in general, it could be appealing to investigate the deformation of some internal components as well, such as the engine or the front axle.

Table 4.1 shows the boundary conditions in which the analysis will be conducted, identified by several parameters, such as cargo mass, vehicle dimensions and vehicle speed.

| *PARAMETER* | *VALUE* | | | |
|---|---|---|---|---|
| ***IMPACT VELOCITY*** | $48\ km/h$ | | | |
| ***VEHICLE MASS*** | $7200\ kg$ | | | |
| ***VEHICLE LENGTH*** | $8.5\ m$ | | | |
| ***CARGO MASS*** | $2936.84\ kg$ | | | |
| ***BOLLARD POSITIONS (Y)*** | $0\ mm$ | $150\ mm$ | $400\ mm$ | $750\ mm$ |

***Table 4.1*** *– Test key parameters and vehicle setup*

To the aim of the test, a first comparison between key time instants will be performed, then the curves will be analysed, to understand the influence of the bollard position on energies, X momentum, which corresponds to the traveling direction of the vehicle, and contact force between the vehicle and the barrier.

### 4.2.1 Bollard offset: 0 *mm*

This bollard position corresponds to the one used for the model validation, and now it will be used as reference for the comparison between all the cases. As it was written before, this particular case has a multiple scope, since it will be useful to double check if the misalignment of the bollard, evidently present in the experimental test used for the validation of the model, is responsible for the slight deviation of the results.

For sake of completeness, Figure 4.18 shows the centered position of the bollard. The results of this case, in terms of energy components and kinematic parameters, have already been shown in sections 4.1.2 and 4.1.3, but for the general purpose of this analysis, also results regarding X momentum and contact force with the bollard, along the traveling direction, will be shown hereafter in Figure 4.21.

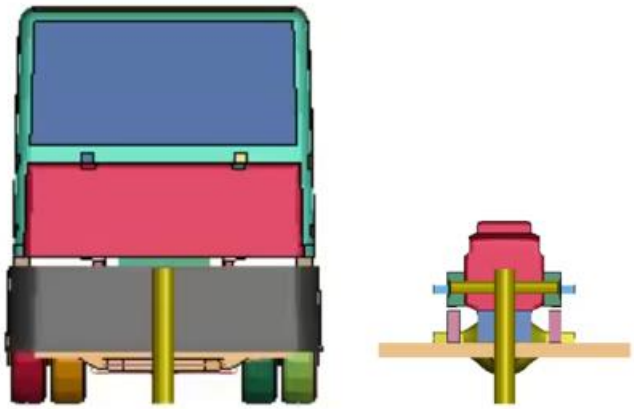

***Figure 4.18*** *– Centered bollard position for complete vehicle and frame*

The deformation of the whole vehicle can be appreciated in Figure 4.19 and the one relative only to the frame is visible in Figure 4.20.


***Figure 4.19*** *– Bollard offset: 0 mm – impact at 160 ms and 1000 ms*

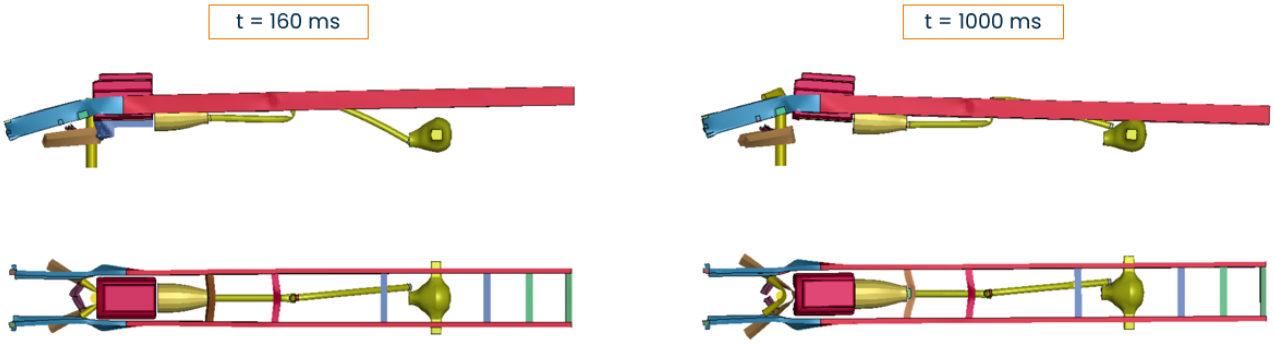


***Figure 4.20*** *– Bollard offset: 0 mm – frame detail of impact at 160 ms and 1000 ms*

It is possible to see that the impact with the engine is quite severe, while the two longitudinal beams bend inward and downward. As it was previously said regarding the validation in section 4.1.1, the behaviour of the vehicle cabin, which is already tilted down in the first instants of the simulation, perhaps could be due to a not so efficient connection with the frame.

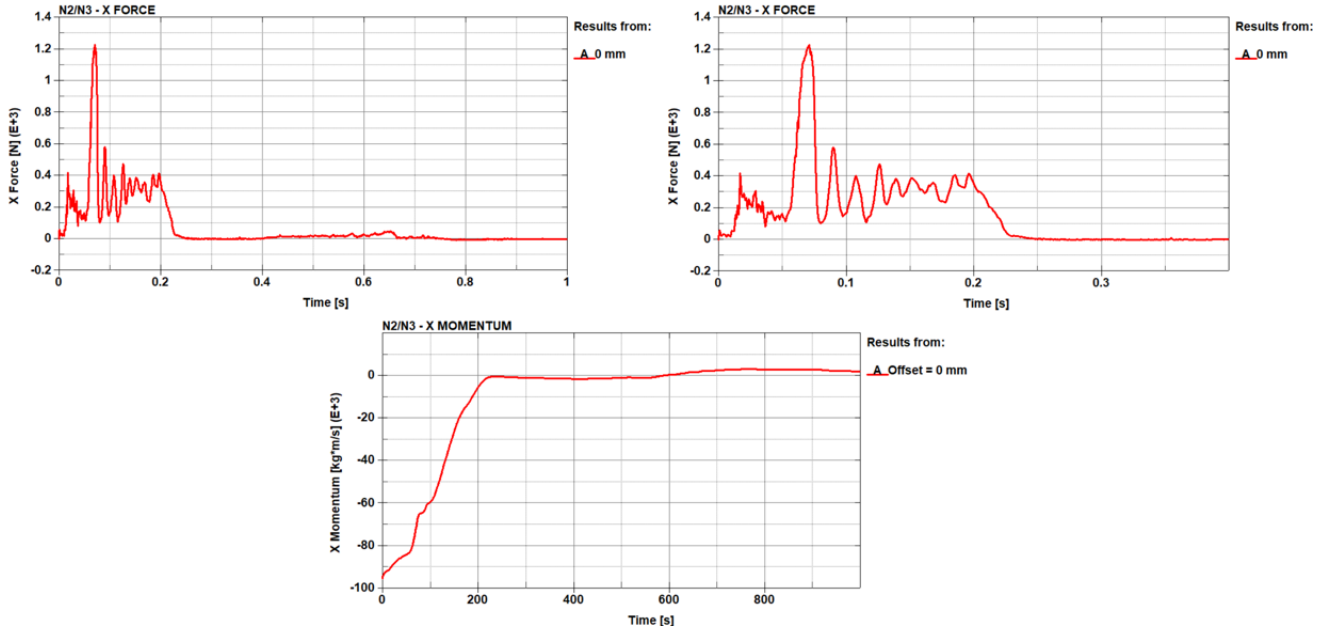


***Figure 4.21*** *– Results for bollard offset 0 mm*

Considerations about the energy components have already been done in section 4.1.2 regarding the validation of the vehicle model.

The contact force instead shows a peak in the first 10 $ms$, probably due to the strong reaction that the engine provides when it comes in contact with the bollard. As it will be explained later, in this case the engine heavily contributes to the total internal energy of the system, as it will be for the case of bollard offset of 150 $mm$, where the engine will be even more deformed. To conclude, the X momentum gives the highest contribution to the resultant momentum of the system, being X the travel direction of the vehicle, stabilizing around 0 $kg \cdot m/s$ once the vehicle has completely stopped on the bollard after the impact.

### 4.2.2 Bollard offset: 150 $mm$

For this case, the bollard is placed at ¾ of the engine, in order to understand which could be the role of such a stiff component on the behaviour of the vehicle after the impact with the barrier. Figure 4.22 shows the position of the barrier for this case of study.

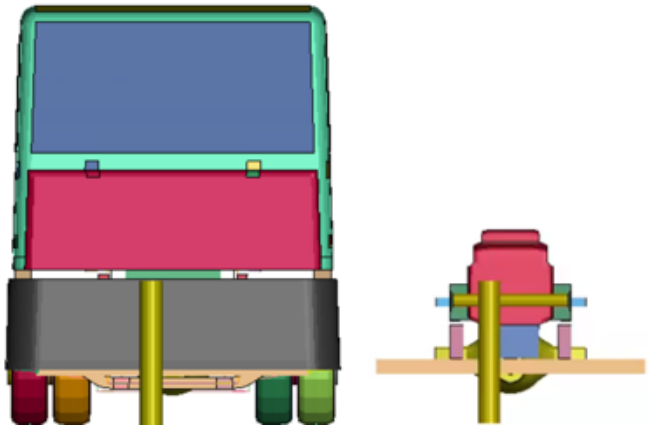

***Figure 4.22*** *– ¾ engine bollard position for complete vehicle and frame*

Hereafter, vehicle and frame deformations for this bollard offset are shown in Figure 4.23 and Figure 4.24.

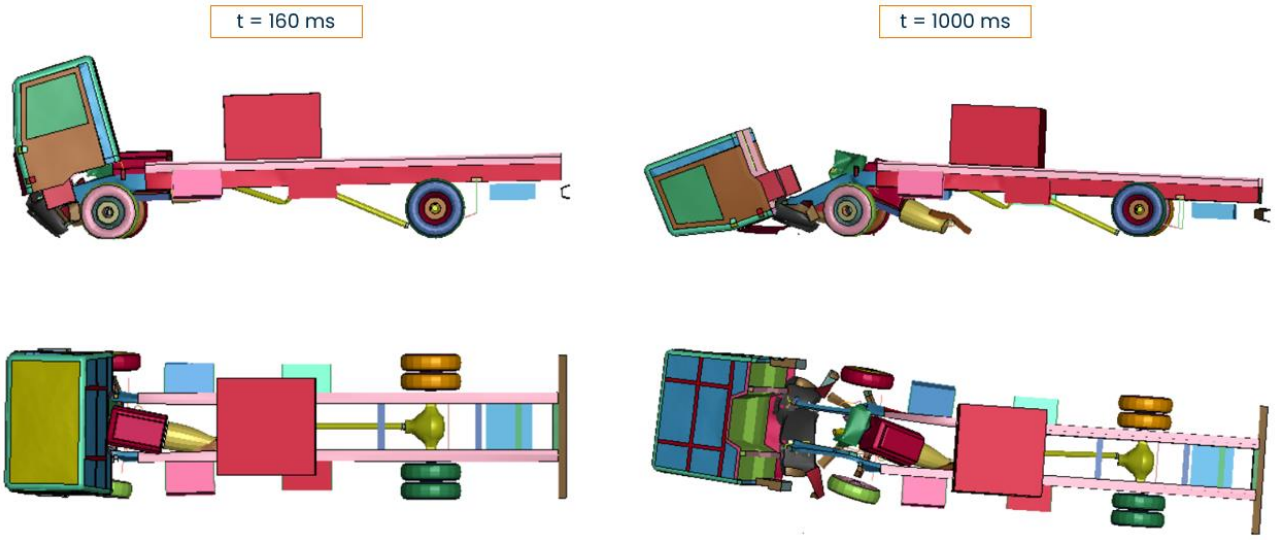


***Figure 4.23*** *– Bollard offset: 150 mm – impact at 160 ms and 1000 ms*

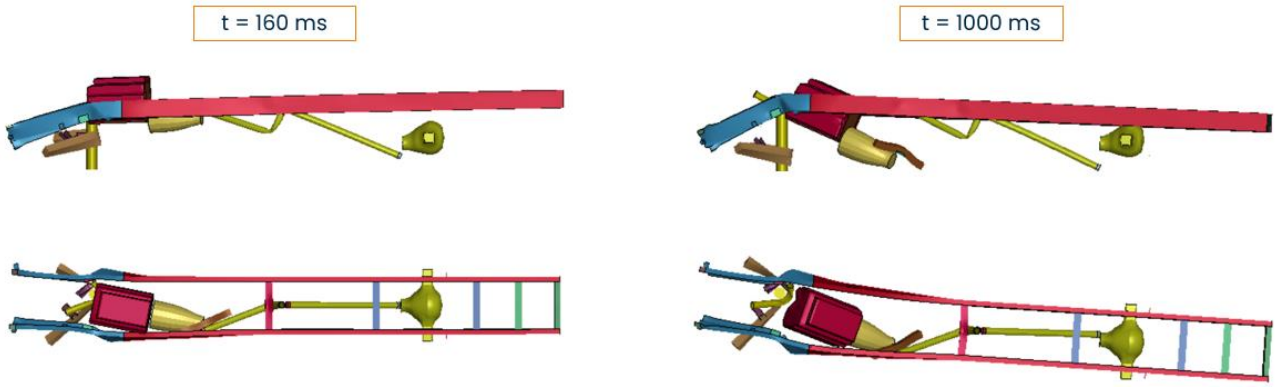


***Figure 4.24*** *– Bollard offset: 150 mm – frame detail of impact at 160 ms and 1000 ms*

Even though the variation of the bollard position could look small, it has a heavy influence on

the vehicle deformation, very evident in the bending of the drivetrain, rather than the engine, which, as it will be shown afterwards, provides a consistent contribution to the internal energy of the system.

Before going ahead with the asymmetry check of the validation, results relative to this bollard position case are shown in Figure 4.25.

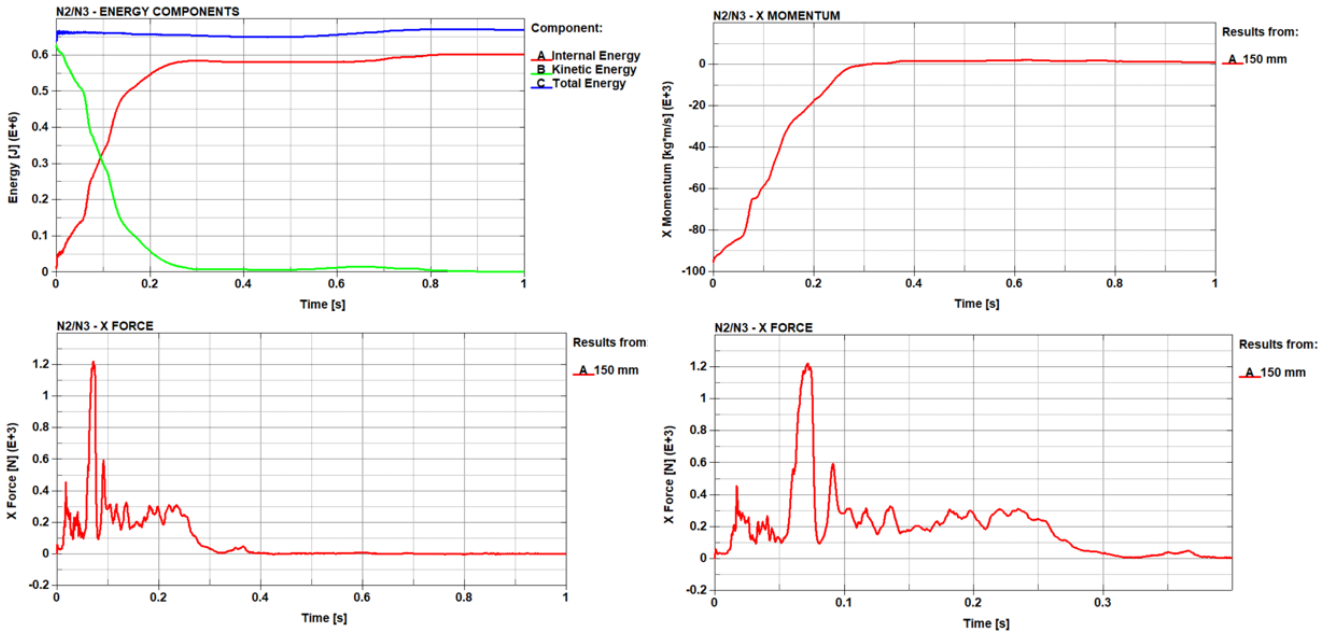


***Figure 4.25*** *– Results for bollard offset 150 mm*

Energy components show a good stability of the model, internal and kinetic energies are specular, as expected, while total energy is almost constant. This is due, as in the previous cases, to other energy components, like the hourglass one, which have never been analysed in this work. At the end, results seem to be quite similar to the reference case of centered bollard, so that the same considerations previously done hold also in this occasion.

In this case, the bollard is placed at ¾ of the engine, as it is clearly visible in Figure 4.22 showing only the frame of the vehicle. But, being the other offsets a bit too large, the asymmetry of the experimental test will be checked only in this case, in Figure 4.26 and Figure 4.27.

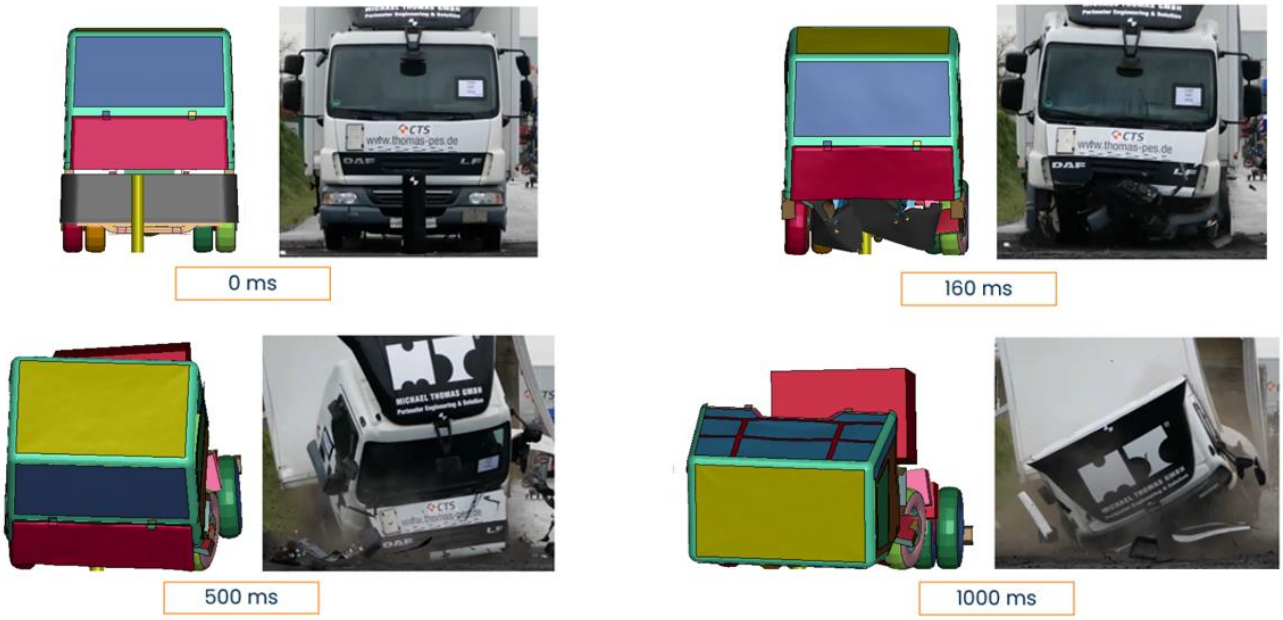


***Figure 4.26*** *– Bollard at ¾ engine animations comparison front view*


***Figure 4.27*** *– Bollard at ¾ engine animations comparison side view*

From the front view visible in Figure 4.26, the time frame corresponding to 160 $ms$ shows a similar behaviour between FEM and experimental vehicles since the FEM cabin seems to rotate in the same direction of the experimental one.

Anyway, it is evident from the other images of Figure 4.27 that moving the bollard from the centered position does not create the expected effect on the motion of the entire vehicle visible in the experimental test. Figure 4.28 tries to figure out which could be the possible reason behind the strong asymmetry present in the experiment.

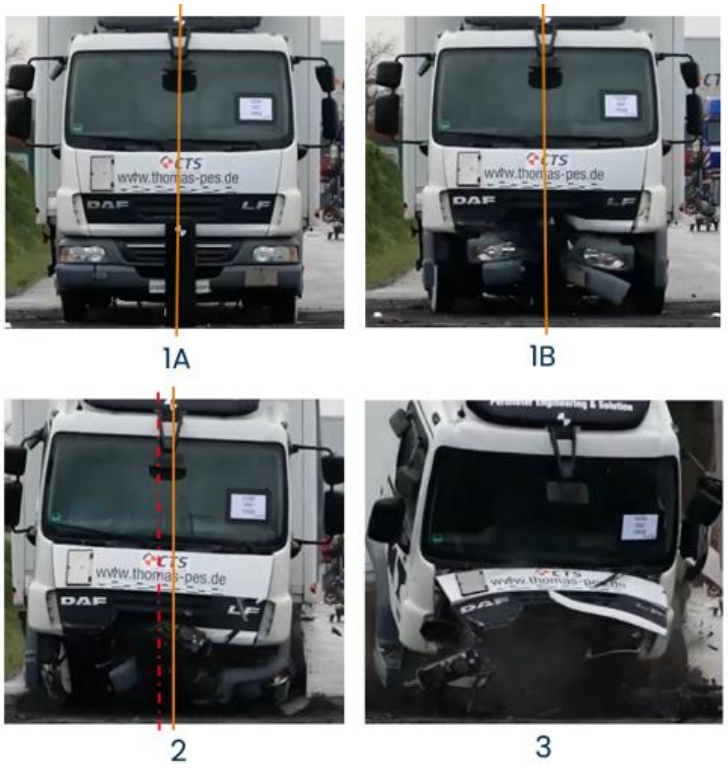


***Figure 4.28*** *– Possible reasons of the asymmetry of experimental test*

Based on these initial time instants, reported in Figure 4.28, it is possible to make the following assumptions:

- Looking at the markers placed above the vehicle cabin and on the bollard (1A), it is visible that, except for few centimetres, the vehicle and the bollard seem to be almost aligned, and they remain in the same condition also right after the impact (1B).
- Some milliseconds after the impact has occurred (2), a misalignment starts to become evident, since the symmetry axis of the bollard, highlighted by the dotted line, is not coincident with the symmetry axis of the vehicle, represented by the solid line. At this point, the experimental cabin starts to rotate towards left.
- Once the vehicle has penetrated the bollard, it starts to move in the opposite direction. This effect could be due to the inertia of the semitrailer, which pushes the cabin, which is no more centered with the bollard, triggering its rotation as well.

Provided that these assumptions hold, it can be concluded that there certainly is a slight misalignment of the bollard with respect to the symmetry axis of the vehicle, which provokes the clear asymmetry of the results, but perhaps the generic N2/N3 vehicle model is not able to properly reproduce the interaction between the vehicle and the bollard, appreciated in the video of the experimental test.

### 4.2.3 Bollard offset: 400 $mm$

For this case, the bollard was moved of 400 $mm$ with respect to the Y axis of the reference coordinate system and placed in front of the vehicle longitudinal beam. This is an important case to

study, since it can be directly connected to the analyses previously carried out with the tubes of Chapter 2 and Chapter 3, which have been considered as a strong simplification of a vehicle beam undergoing a crash. Figure 4.29 shows the position of the bollard with respect to the whole vehicle and to the frame.

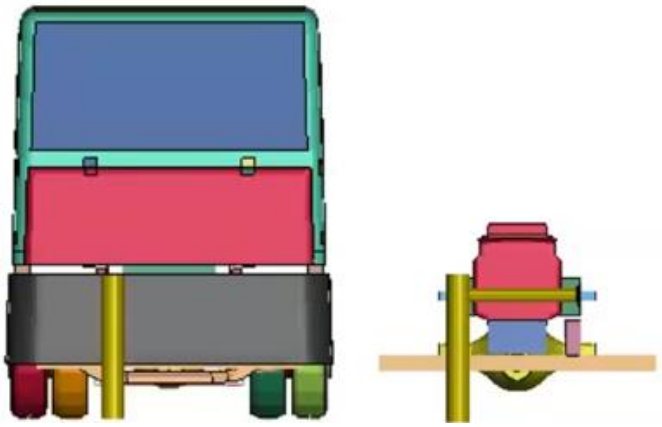

***Figure 4.29*** *– Longitudinal beam bollard position for complete vehicle and frame*

In this case, the component that plays a key role in the crash is certainly the longitudinal beam, so that it is expected that it will be the highest contribution to the internal energy of the system, since it is a measure of the global deformation shown for the whole vehicle and for the frame in Figure 4.30 and Figure 4.31.


***Figure 4.30*** *– Bollard offset: 400 mm – impact at 160 ms and 1000 ms*

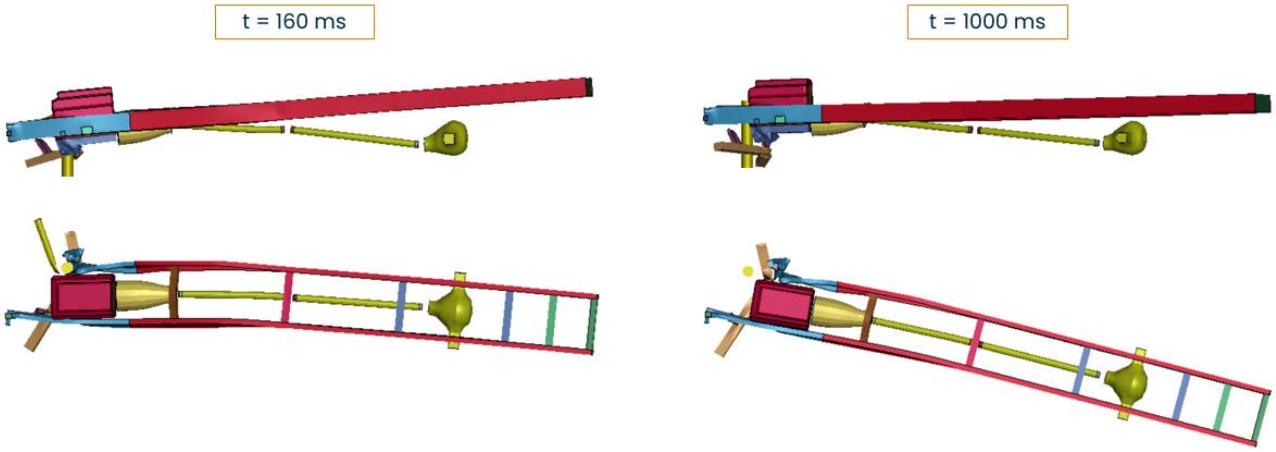


*Figure 4.31 – Bollard offset: 400 mm – frame detail of impact at 160 ms and 1000 ms*

In this case, the rotation of the vehicle is more pronounced, due to the bending behaviour of the longitudinal beams, which play a key role in the deformation mechanism of the system. As it will be explained in the dedicated section, even if because it is clearly visible from the image of the frame, the longitudinal beams provide, in this case, almost half of the total internal energy.

Figure 4.32 instead, illustrates the results relative to this case.

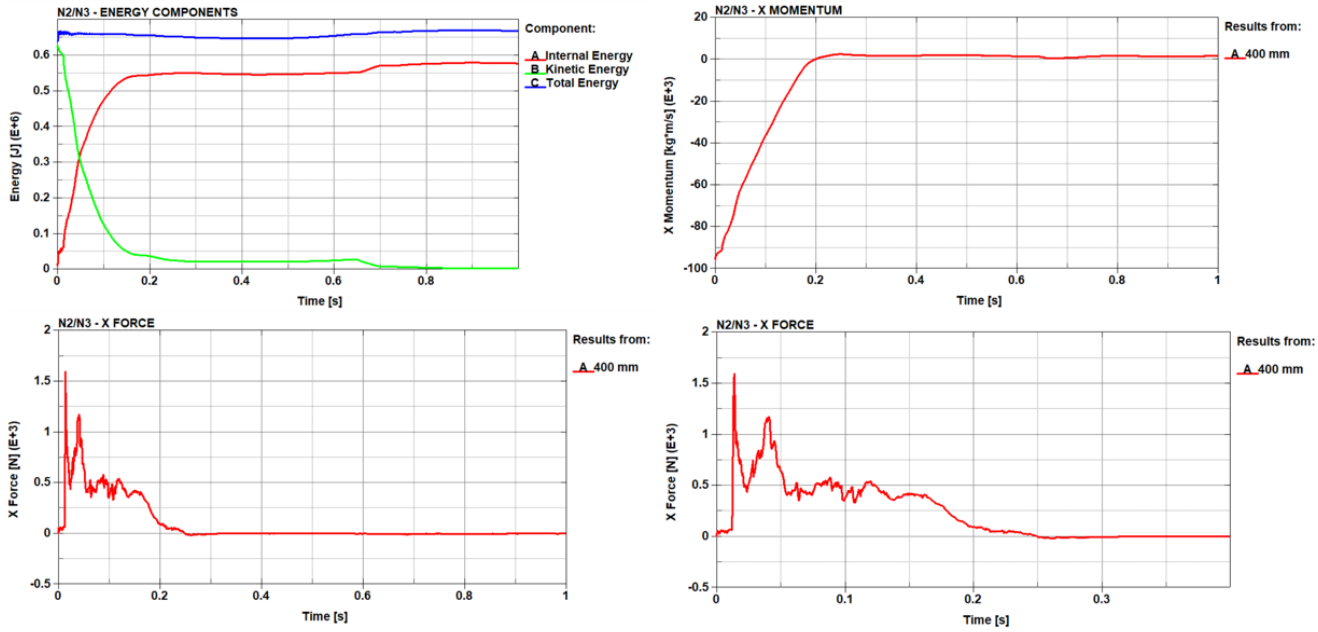


*Figure 4.32 – Results for bollard offset 400 mm*

The most evident difference with the previous cases is that the peaks of the contact force come earlier, due to the anticipated contact between the vehicle longitudinal beam and the bollard. Anyway, results in terms of energy are coherent with the previous analysed cases, and also the X momentum trend has the usual behaviour.

In this circumstance, the engine does not come in contact with the bollard anymore, as it was for the previous situations, and so it does not absorb so much energy because it is not directly involved in the impact. It is important to highlight that even the contact force between the vehicle and the

barrier undergoes important variations from case to case. The results that will be shown afterwards will justify the hypotheses that have been made up to now.

### 4.2.4 Bollard offset: 750 $mm$

Now the bollard is moved in between the longitudinal beam and the front right wheel, just to see how the vehicle front axle behaves when it is directly involved in the impact. In this case, it is expected that the vehicle will remain stuck to the bollard due to the front wheel, rotating around the Z axis of the reference system. Figure 4.33 shows the last case of bollard position that will be analysed.

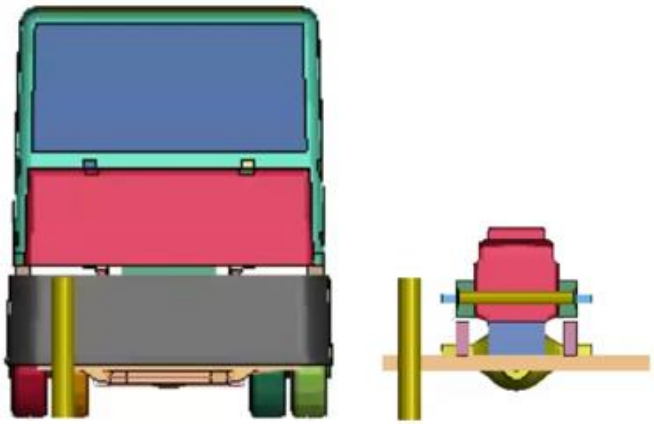

***Figure 4.33*** *– Btw longitudinal beam and wheel bollard position for complete vehicle and frame*

As it was said, in this case the key component is expected to be the front axle, which should also provide the highest contribution to the total internal energy of the system, as it will be shown later on. The deformation of the system is appreciable in Figure 4.34 and Figure 4.35, followed by the results relative to this case shown in Figure 4.36.


***Figure 4.34*** *– Bollard offset: 750 mm – impact at 160 ms and 1000 ms*

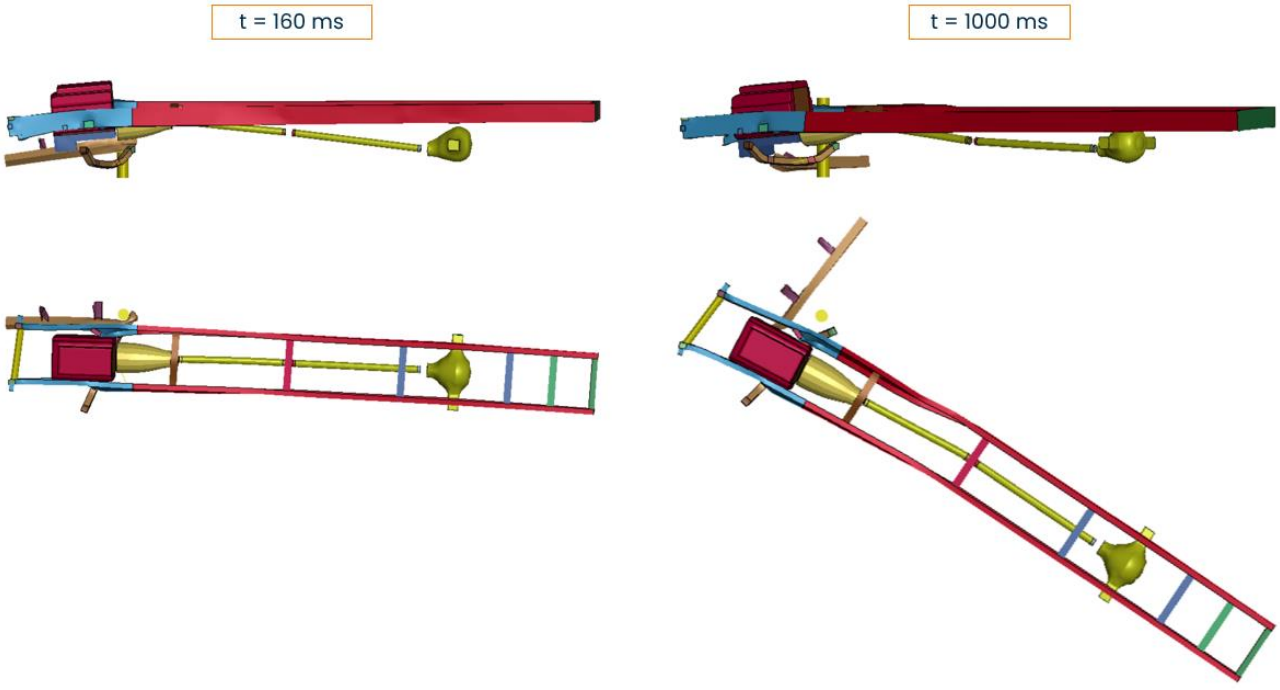


***Figure 4.35*** *– Bollard offset: 750 mm – frame detail of impact at 160 ms and 1000 ms*

The key component here is the front axle that causes the huge rotation of the vehicle around the bollard. Just on this occasion, the front axle has been showed in the animations in order to appreciate its role in the deformation mechanism of the vehicle. All the front-end components, such as the engine, the gearbox or the fan, are not directly involved in the impact and, as it will be seen afterwards, they do not highly contribute to the total deformation as they did for the other cases.

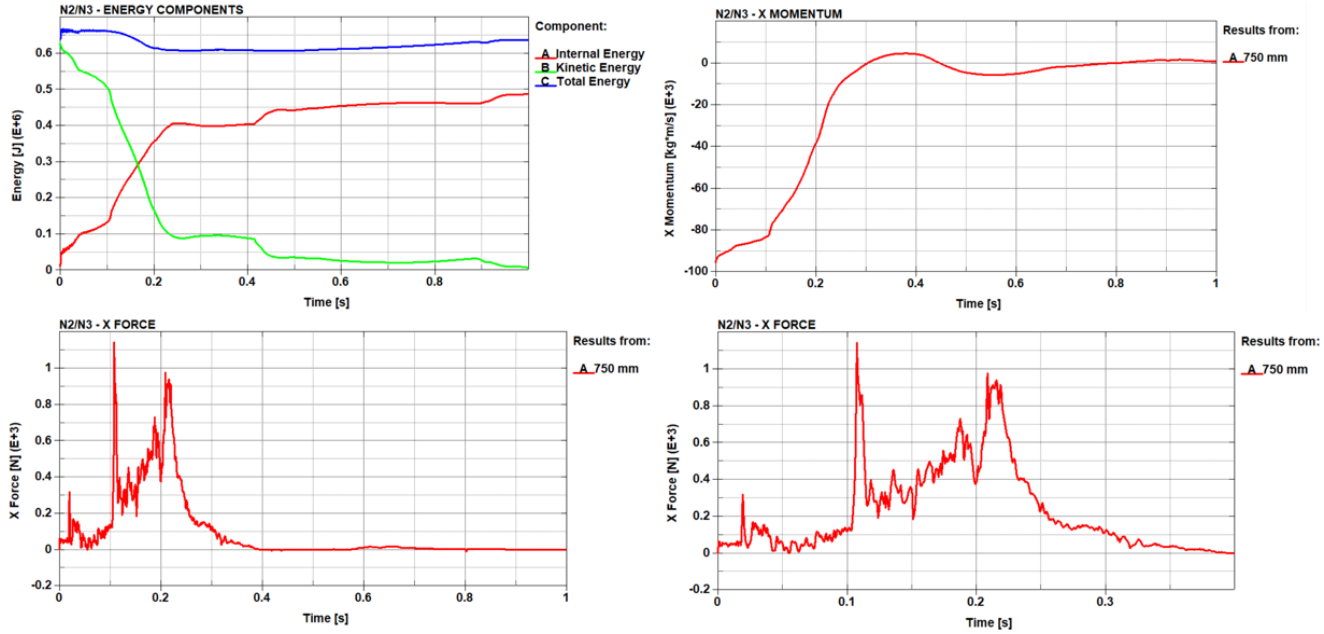


*Figure 4.36 – Results for bollard offset 750 mm*

The biggest difference, highlighted in Figure 4.36, between these results and the other ones is represented by the energies trends, which seem to have a discrepancy with those of the other cases. In particular, it is evident that the system has a much lower energy absorption capability, and also the total energy behaves to be less constant than before, maybe due to the contribution of the other energy components, like the hourglass or the sliding ones.

Even the X momentum is slightly different than before, with a kind of oscillating behaviour due to the accentuated rotation, and the consequent not negligible lateral velocity, that the vehicle undergoes once the impact has occurred. Nevertheless, the contact force has a different behaviour as well, and it will be compared to the other cases in the following sections.

## 4.3 Results comparison

Once each of the remarkable positions has been identified and deeply described, it is worthwhile making a comparison between all the results that have been shown up to now, in order to understand which is the influence of the variation of the bollard position on the results, which are the vehicle parts with the highest energy absorption capability and so on.

Nevertheless, for each case, an internal energy threshold has been chosen and set to 5% of the total internal energy of the system, so that the components whose contribution overcomes this threshold will be identified and compared to the rest of the system.

### 4.3.1 Internal energy

Internal energy is for sure the key energy component, since it is a measure of the system deformation. In this particular case, it measures how much the vehicle is deformed by the bollard

after the impact. As a consequence, it is also able to measure how much energy the bollard can absorb in order to stop the hostile vehicle during a possible terroristic attack. In particular, this aspect classifies, as it has been explained in the introductory section 1.1.2, the level of protection of a specific barrier.

Figure 4.37 shows the comparison between all the internal energies that have been shown for each of the analysed cases.

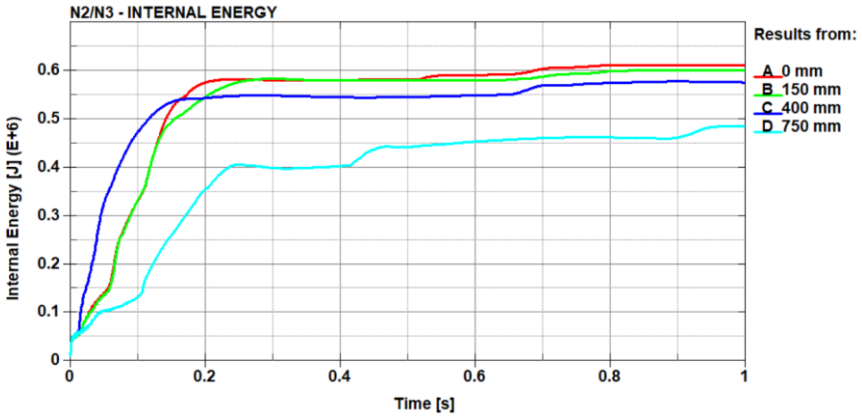


*Figure 4.37 – N2/N3 bollard impact internal energy comparison*

From the previous plot, the less deformed state is identified by the light blue curve, referred to the case of bollard moved of 750 $mm$, in between the front right wheel and the longitudinal beam. This is justified by the fact that the vehicle does not fully catch the bollard, and the consequences of the impact are reflected just on the front axle, which, on this occasion, will be the most deformed component. Other parts present in the front-end of the vehicle are not involved in the impact at all, such as the engine, the fan or the front longitudinal beam, which is just bent due to the inertia of the vehicle that makes it rotate around the Z axis, creating a not negligible yaw angle.

On the other hand, the most severe case remains the centered bollard, since all the front-end parts are damaged by the impact. From the plot of Figure 4.37, it is also possible to understand that the first two cases are characterized by an almost equal behaviour of the whole system, since the level of final deformation can be considered practically the same.

In conclusion, moving the bollard to an even more evident decentralized position will cause less damages to the vehicle. This is the reason why it is mandatory to fix a maximum distance between two consecutive bollards, in order not to allow a hostile vehicle to enter a protected area, but also to produce a significant level of damage to make the vehicle inoffensive, as deeply explained in section 1.1.2.

### 4.3.2 Kinetic Energy

Being specular to the internal energy, the same considerations done in the previous section 4.3.1 hold on this occasion. Once the impact has occurred, all the energy of the system, stored as kinetic, starts to become internal, because of the increasing deformation that the vehicle undergoes. This deformation causes a drop of the kinetic energy, which at the end of the simulation is asymptotical to zero, caused by the abrupt decreasing velocity of the vehicle after the impact. All

these considerations can be appreciated in Figure 4.38.

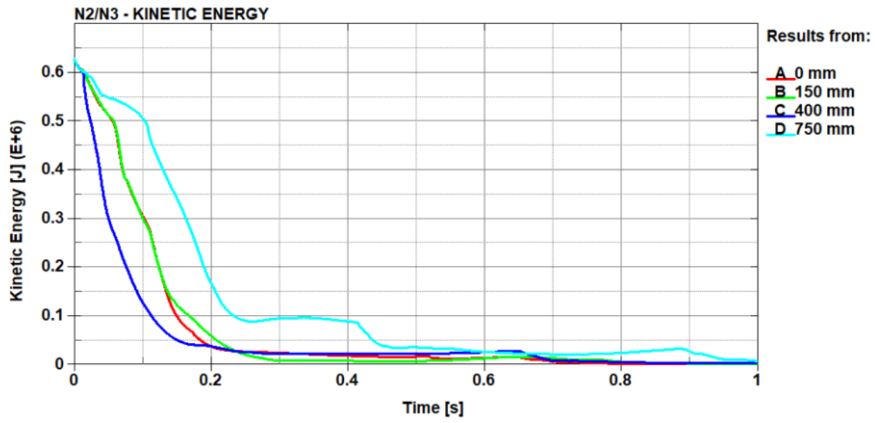


*Figure 4.38 – N2/N3 bollard impact kinetic energy comparison*

As it is visible here in Figure 4.38, the highest value of kinetic energy is appreciable for the light blue curve, corresponding to the case of bollard moved of 750 $mm$. The motivation could be searched in the great rotation that the flatbed is subjected to, which increases the lateral speed of the vehicle.

As far as the other cases are concerned, the vehicle rotation looks similar, so that the kinetic energy content of the system appears to be almost the same.

### 4.3.3 Total Energy

Regarding the total energy instead, looking at the internal and kinetic components, it is expected that the energy content of the cases of bollard moved of 150 $mm$, 400 $mm$ and 750 $mm$ respectively, will almost be the same. For the case of bollard placed in between the front right wheel and the longitudinal beam instead, being the impact marginal, the level of total energy should clearly be lower than the other cases. Figure 4.39 shows what has been said up to now.

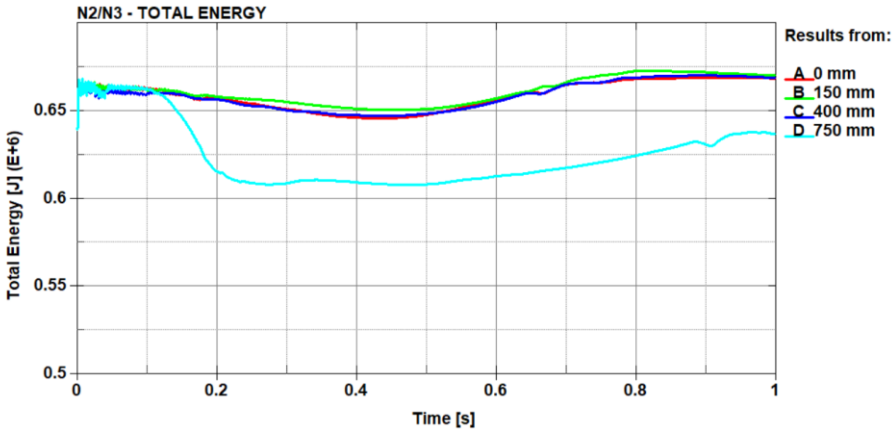


*Figure 4.39 – N2/N3 bollard impact total energy comparison*

As expected, the energy content of the first three cases is coherent to the previous results, and

above all, almost constant, showing a good energy distribution among the parts that make up the system. The light blue curve instead, always referred to the case of bollard moved of 750 $mm$, shows much lower values because of an inferior general deformation of the system. This could be due to an evident marginal impact that occurs between the vehicle and the bollard, where most of the front-end components do not actively participate in the incident, as it was pointed out in the previous section 4.3.1.

Anyway, a detailed analysis on the most deformed components per each of the considered cases will be performed, in order to understand which is the contribution of the parts to the total deformation of the system.

### 4.3.4 Contact Force

An interesting result to discuss is the contact force, along the travelling X axis, which is generated when the vehicle and the bollard come in contact one with each other. This is remarkable because the components of the front-end of the vehicle that impact the bollard are different from case to case, but above all, they are made of very different materials. For this reason, the distribution of the contact force between the vehicle and the barrier looks very different from case to case, as it is shown in Figure 4.40.

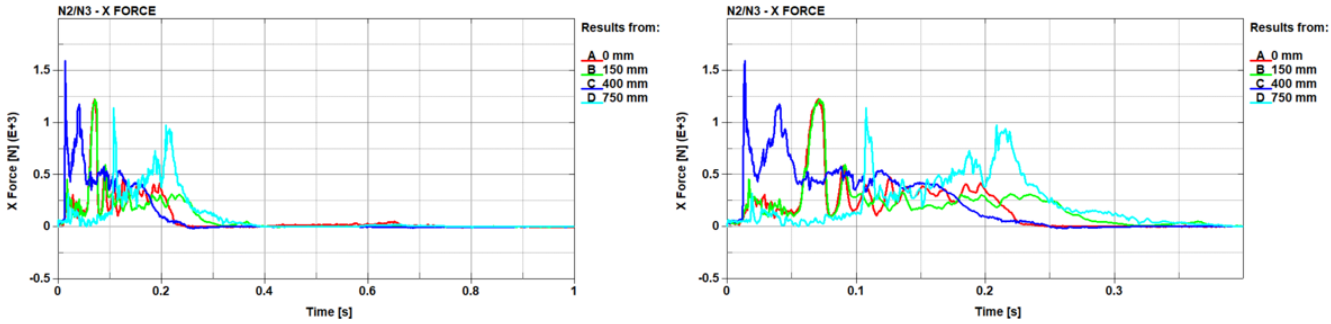


***Figure 4.40*** *– N2/N3 bollard impact contact force comparison*

For sake of completeness, the plot has been cut at 400 $ms$, in order to better recognize the different curves, but also because once the impact has occurred, there is any force generated at the interface between the barrier and the vehicle, so it is useless to look at the complete plot.

In order to have a clear understanding of the previous plot of Figure 4.40, it is worthwhile making a comparison between each curve of the graph and the corresponding animations, in order to understand how this contact force is exploited and which components are involved in the successive phases of the contact with the bollard.

If, for instance, the case of bollard offset of 150 $mm$ is taken into account, the force peaks arise at 15 $ms$, 70 $ms$ and 90 $ms$ respectively, and the corresponding behaviour of the model is hereafter shown in Figure 4.41.

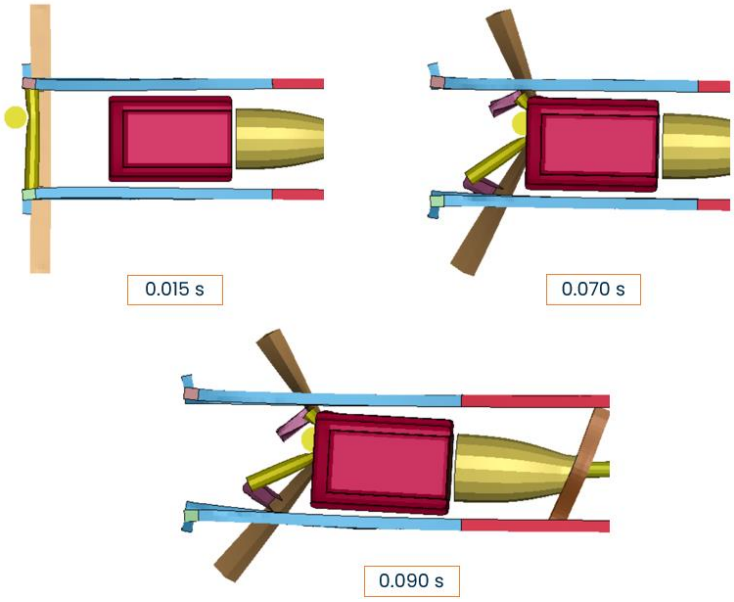


***Figure 4.41*** *– Comparison between X force plot and animations with bollard at 150 mm*

Looking at the three key time instants, it is possible to understand the reason why the three corresponding peaks of the contact force arise. In detail, the first one is addressed to the impact with the front bumper and the front cross member, the second one is addressed to the impact with the fan – not shown here for visualization purposes – and the engine, while the third one can be addressed to the detachment of the first frame cross member, shown at the right of the last image of Figure 4.41.

Given that the highest contact force peak has been registered in the case of bollard moved of 400 $mm$ from the centered position, it is interesting to analyse the correlation between the animation of the crash and the corresponding blue curve of Figure 4.40.

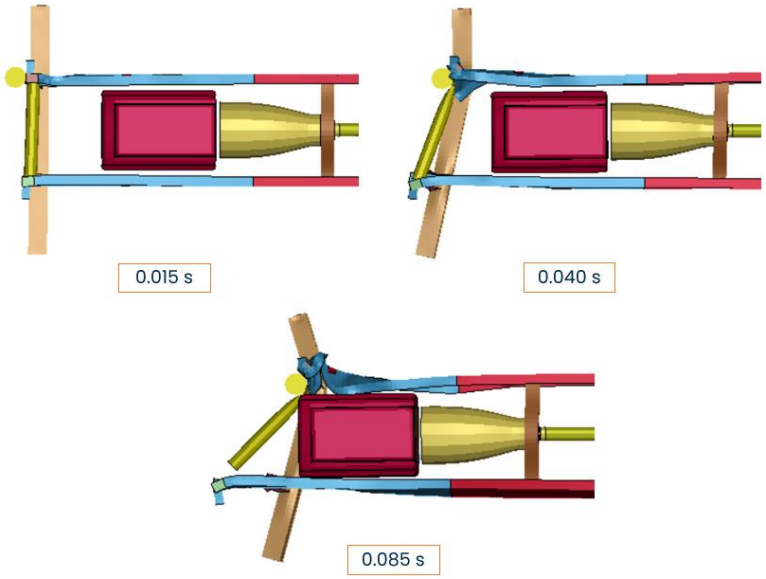


***Figure 4.42*** *– Comparison between X force plot and animations with bollard at 400 mm*

The key time instants are respectively 15 $ms$, 40 $ms$ and 85 $ms$, as reported in Figure 4.42. In particular, the first one corresponds to the very first impact between the bollard and the front cross

member, which generates the highest peak of the contact force, suddenly followed by the crushing of the front part of the longitudinal beam at 40 $ms$, which causes a second high peak of the force appreciable in Figure 4.40. Then, the third peak, visible at 85 $ms$ from the plot, corresponds to the marginal impact between the barrier and the engine. In this case, the longitudinal beam undergoes a very large deformation, which will be quantified and compared to the total deformation of the system, in terms of internal energy, in the following sections. For this reason, the amount of deformation of the system is quite high, even though the impact between the vehicle and the bollard is a bit marginal.

When the bollard is moved of 750 $mm$ from the central position, the resulting deformation is obviously lower – as it was shown in Figure 4.37 – than the other cases, as well as for the total energy content. This is due, as it was previously said, to the minor impact that occurs between the vehicle and the bollard.

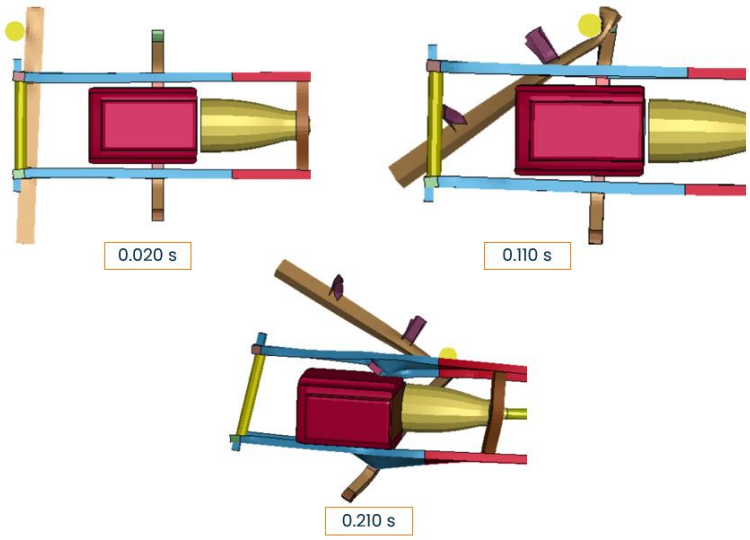


***Figure 4.43*** *– Comparison between X force plot and animations with bollard at 750 mm*

In this case, at 20 $ms$ the bollard hits the front bumper bar, resulting in the first contact force peak in the plot. The highest point of the light blue curve of Figure 4.40 can be found at 110 $ms$, once the bollard hits the front axle that, as it will be explained afterwards, will be the component that contributes more to the total deformation of the system, in this specific case. Then at 210 $ms$ the third peak arises, once the vehicle is completely stuck, with the bollard placed in between the front right wheel and the whole front axle.

### 4.3.5 X Momentum

It is worthwhile to analyse the trend of the X momentum too, even if it is expected that it will have almost the same behaviour for all the four analysed cases.

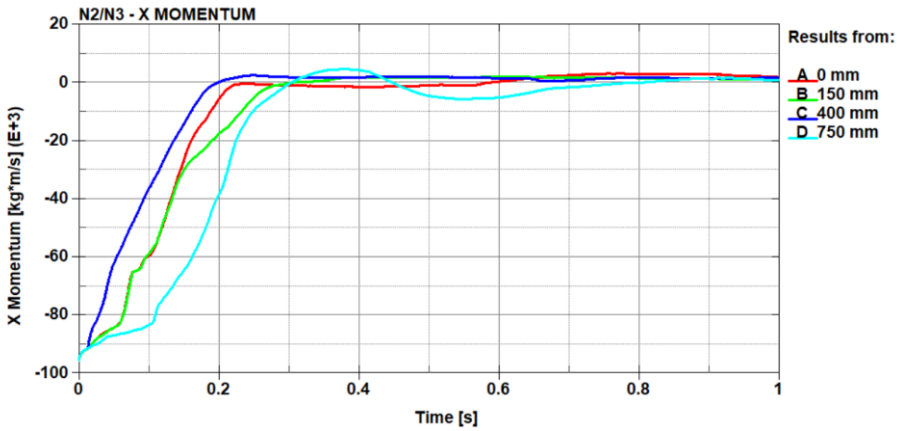


*Figure 4.44 – N2/N3 bollard impact X momentum comparison*

Being linearly proportional to the vehicle speed, all the curves tend to 0 $kg \cdot m/s$ since the vehicle is stopped by the bollard. If the trends of the curves relative to the cases of 0 $mm$, 150 $mm$ and 400 $mm$ are coherent with each other, the one relative to the case of 750 $mm$ has a kind of oscillatory behaviour because, as it was explained in the previous section 4.2.2, the vehicle still has a residual speed along X direction, due to its accentuate rotation around the bollard.

Nevertheless, the initial values of the X momentum are negative, since the vehicle is proceeding in the negative direction of the X axis during the simulation.

## 4.4 Deformed components

On the basis of what has been affirmed up to now, it is worth analysing which are the most deformed components in each of the four considered cases for the current investigation. Starting with that, a deeper statistical investigation on the influence of these components on the total deformation of the system will be conducted, trying to get some interesting considerations and conclusions.

For sake of completeness, a threshold of 5% of the total internal energy of the system has been chosen, and only components whose internal energy overcomes this threshold will be considered, since they sufficiently contribute to the overall deformation of the vehicle coming from the impact. Figure 4.45 shows which are the components involved in the impact, whose internal energy overcome the limit of 5% of the total internal energy of the system.

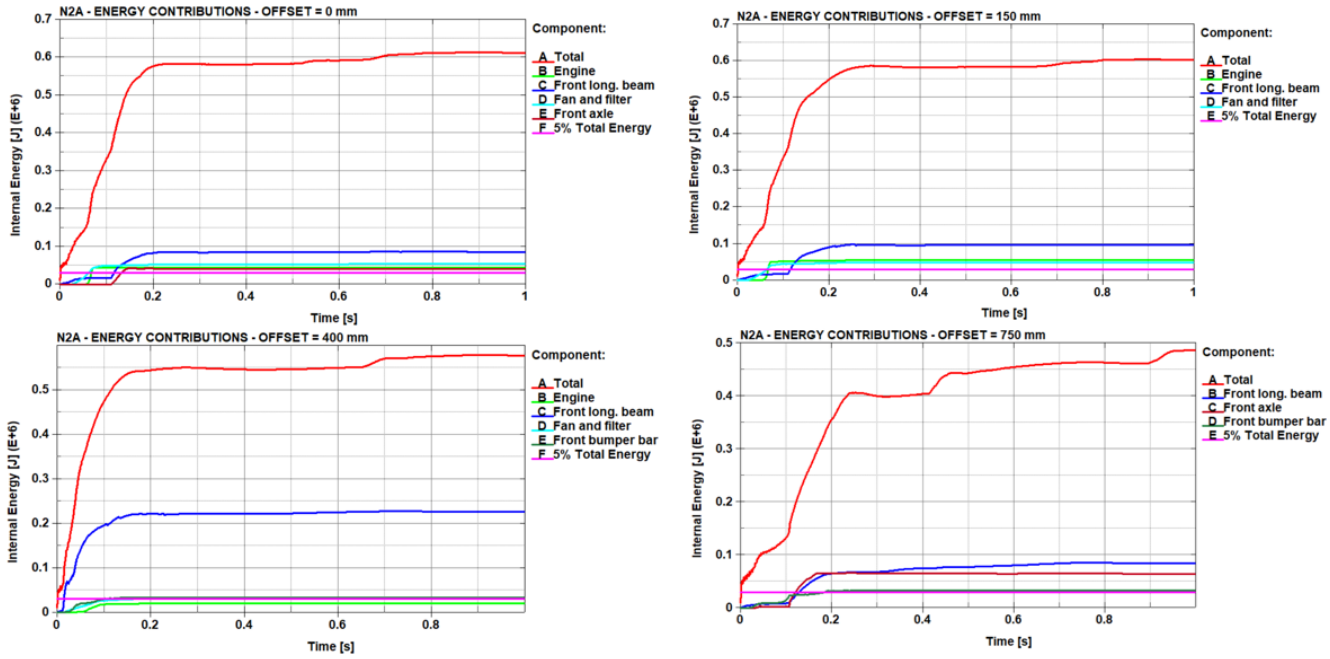


***Figure 4.45*** *– Components energy contributions for each case*

Provided that the 5% of the total internal energy is calculated on its maximum value at the end of the simulation for each case, the threshold for the four cases of interest stands around 25-30 $kJ$, indicated in the above plots of Figure 4.45 by the purple line.

As it is visible, the most involved components in the impact are always the following ones:

- Engine
- Front longitudinal beam
- Fan and filter
- Front axle
- Front bumper bar

However, it is possible to notice that the engine does not overcome the limit value of 5% of the total internal energy in the case of 400 $mm$, even if it will be analysed anyway, as it will be explained afterwards in the engine dedicated section.

The differences between the last case of 750 $mm$ and the other ones are clearly evident. Being the impact between the vehicle and the bollard marginal, the parts placed in central position inside the vehicle are not directly involved anymore, so that the front axle and the front bumper bar overcome the threshold, rather than the front longitudinal beam, always responsible of the heavy rotating motion of the vehicle after the contact. But this time, the contribution given by the engine, or the fan, is very negligible.

At the end, as it was done in Chapter 2, a statistical analysis will be carried out, in order to understand the influence of each component on the system deformation, in percentage terms, taking the maximum energy value in the final deformed state, so that at the end of the simulation.

### 4.4.1 Deformable Engine

One of the key components of the front-end of the vehicle, which is also actively involved in the impact, is the engine. In this generic vehicle model, the engine has been realized in two distinct parts, the inner one modelled as rigid steel, while the outer one made of a crushable foam that covers the rigid part. Given that every rigid part does not undergo neither plastic nor elastic deformation, just the deformable part of the engine was considered for this type of evaluation.

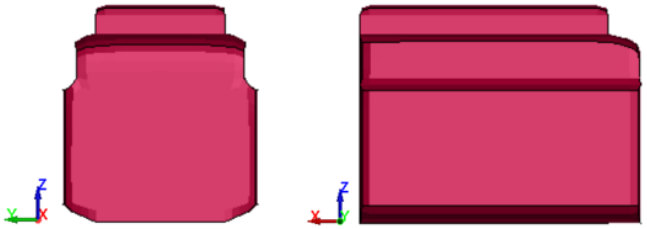

***Figure 4.46*** *– Front and side views of deformable engine*

The reason behind the choice of realizing the engine in two different parts lays in the need of avoiding a rigid shock between the part and the barrier, since the rigid impact may have caused significant peaks in the contact force. So that, it has been decided to cover the rigid part with a deformable part, in order to mimic the deformable behaviour of the softer parts located nearby the engine.

Figure 4.46 shows the front and the right views of the part of the engine that will be considered, and of which the relative displacements will be analysed. The reason why it is not so effective to analyse the plastic strain of this component stands in the material properties. In fact, the material of this part has been modelled with the card **CRUSHABLE_FOAM*, with the following stress-strain curve shown in Figure 4.47, and the parameters listed in Table 4.2.

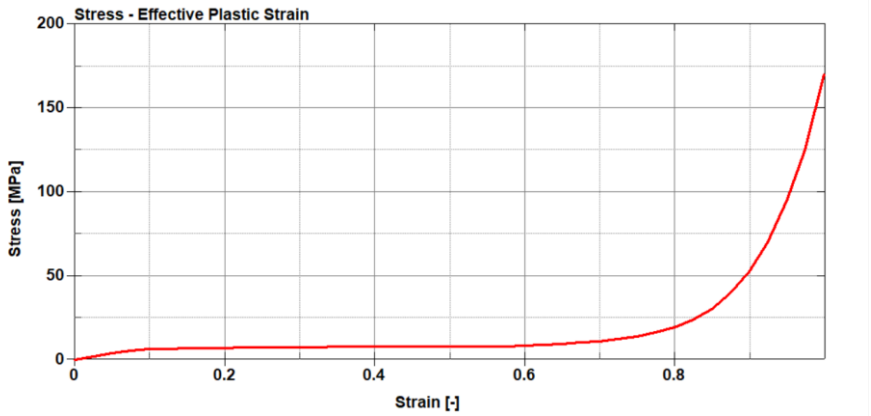


***Figure 4.47*** *– Characteristic of a crushable foam material of the engine deformable*

| ***PARAMETER*** | *SYMBOL* | *VALUE* |
|---|---|---|
| ***YOUNG'S MODULUS*** | $E\ (MPa)$ | 20 |
| ***POISSON'S RATIO*** | $\nu\ (-)$ | 0.30 |
| ***DENSITY*** | $\rho\ (kg/\mathrm{m}^3)$ | 2437 |
| ***TENSILE STRESS CUTOFF*** | $\sigma_{CO}$ (MPa) | 100 |
| ***DAMPING COEFFICIENT*** | $\zeta\ (-)$ | 0.20 |

***Table 4.2*** *– Crushable foam parameters*

As it is visible from the material characteristic, the curve can be divided in three distinct parts. The first one, up to $\varepsilon = 0.1$, describes the *elastic* behaviour of the material, the second one, from $\varepsilon = 0.1$ up to $\varepsilon = 0.6$, describes the *plastic* behaviour, while the last part of the curve, from $\varepsilon = 0.6$ to $\varepsilon = 1$, is the *densification* region, where the material gets harder and dense due to the high level of tension to which it is subjected.

From the above Table 4.2, it is suddenly evident that the Young's modulus of this material is particularly low, since it is much less rigid than a common steel, used to model the majority of the vehicle components, and moreover it has a much lower density. The cutoff stress instead, represents the point where the material characteristic enters the plastic field, acquiring a residual deformation.

For the reason described above, showing the effective plastic strain of the deformable engine could not be suitable to provide a hint of how much the part is deformed after the impact. A more effective way consists of "depurating" the component from the motion due to the impact between the bollard and the vehicle, showing its relative displacements with respect to a reference system that should be fixed to the engine itself. Figure 4.48 provides, in the final deformed states of each of the four analysed cases, the relative displacements of the deformable engine, expressed in $mm$.

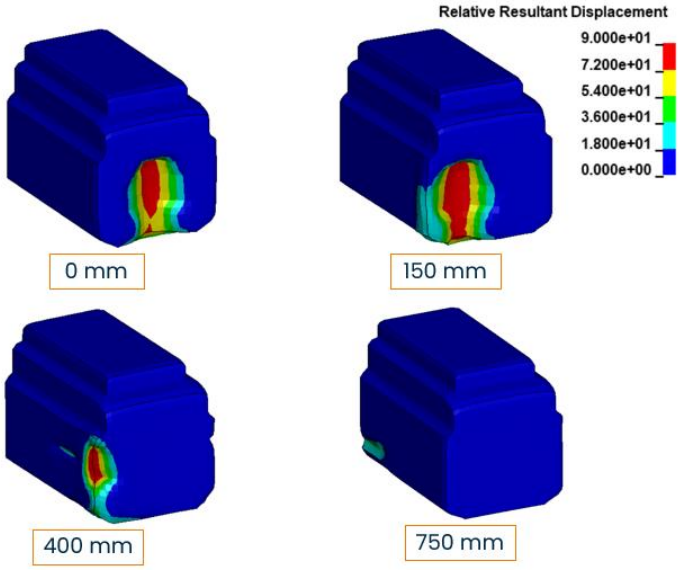


***Figure 4.48*** *– Relative resultant displacements of deformable engine in final deformed state*

Nevertheless, it is useful to make a comparison between the images and the relative curves of the internal energy.

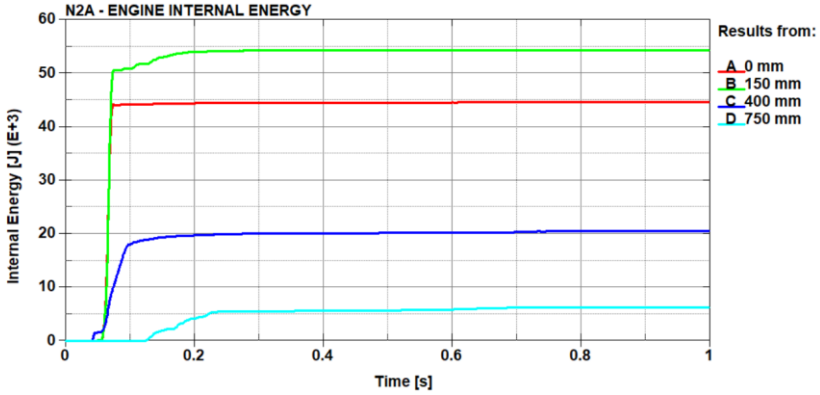


***Figure 4.49*** *– Deformable engine internal energy for each case*

The plot shown in Figure 4.49 indicates that the engine participates with a very high contribution to the total deformation of the system in the case of 150 $mm$. Coherently to the resultant displacements shown in Figure 4.48, the elements and the nodes of the deformed face of the engine are well compressed in the case of 150 $mm$, justifying the increase of internal energy of the green curve.

### 4.4.2 Front Longitudinal Beam

As far as the longitudinal beam is concerned, this is the part that is deformed the most in each case analysed so far. For this purpose, only the front part of the longitudinal beam will be considered, since in the model the longitudinal beams have been split in two different parts, in order to better simulate the connection between the cabin and the frame.

As it was said up to now, the most evident contribution that the front longitudinal beam gives to the total internal energy has been observed in the case of bollard moved of 400 $mm$ from the centered position of the running vehicle, so that when the bollard is placed in front of the longitudinal beam itself. This is indeed the closest example to the tube crush-shock case, studied in Chapter 3. Figure 4.50 illustrates top, side and isometric views of the current component under investigation.

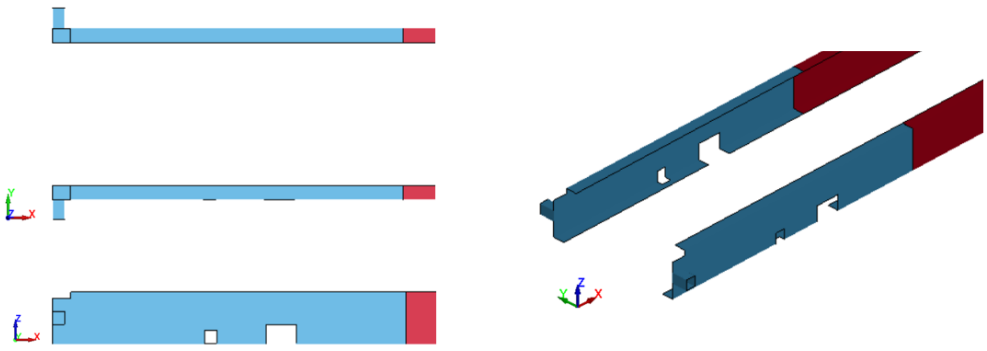

***Figure 4.50*** *– Front, side and isometric views of front longitudinal beam*

This time, the longitudinal beams are modelled using a plastic deformable steel, so that analysing the effective plastic strain, in order to give an idea of their deformation, would be effective in this case. This is done in Figure 4.51.

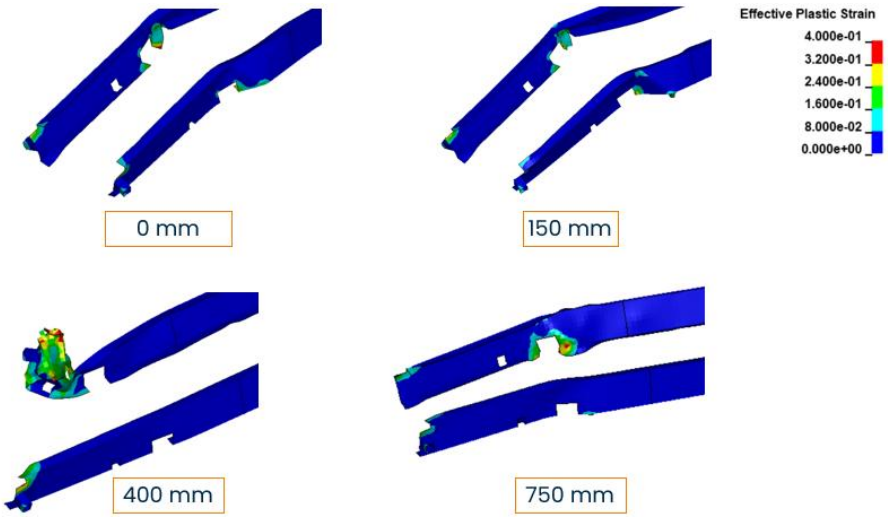


***Figure 4.51*** *– Effective plastic strain of front longitudinal beam in final deformed state*

Also in this case, it is clear that the case of 400 $mm$ is the very critical as well, with the front longitudinal beam that contributes to almost half of the total internal energy of the vehicle, as it is visible in the plot of Figure 4.52.

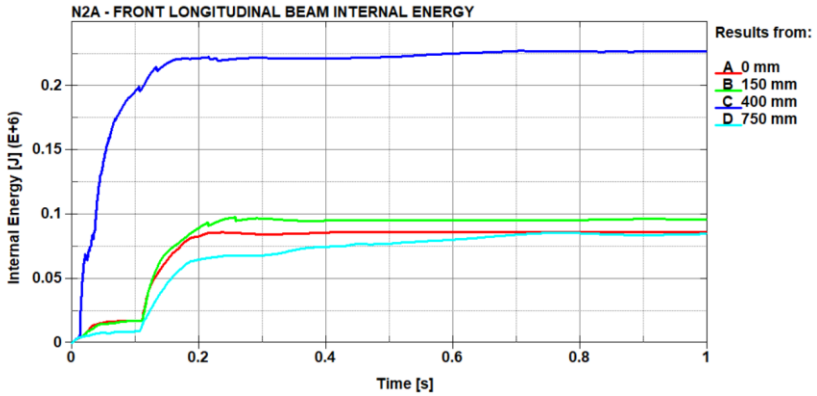


***Figure 4.52*** *– Front longitudinal beam internal energy for each case*

Provided that in the case of 400 $mm$ the longitudinal beam internal energy is the highest value among the energies of all the other components, even in the other cases of study the contribution that it gives to the system is not negligible at all, being actively involved in the impact in all the cases, as it is visible from the plot. The level of energy in the final deformed state is almost the same for the case of 0 $mm$, 150 $mm$ and 750 $mm$ respectively, due to the active role that the beam has in the rotating motion of the vehicle after the impact, also thanks to its great absorption capabilities.

### 4.4.3 Fan and Filter

Even if this is not a structural component of the vehicle, being placed in front of the engine,

the fan and filter absorbs a high part of the energy coming from the impact. Nevertheless, it should be pointed out that it is made of aluminium, so that it has a higher plastic deformable behaviour than steel. The material parameters are shown hereafter in Table 4.3.

| ***PARAMETER*** | *SYMBOL* | *VALUE* |
|---|---|---|
| ***YOUNG'S MODULUS*** | $E\ (MPa)$ | 70000 |
| ***POISSON'S RATIO*** | $\nu\ (-)$ | 0.28 |
| ***DENSITY*** | $\rho\ (kg/\mathrm{m}^3)$ | 5500 |
| ***YIELD STRESS*** | $\sigma_Y$ (MPa) | 100 |
| ***EFFECTIVE PLASTIC FAILURE LIMIT*** | $\varepsilon_Y\ (-)$ | 0.50 |

***Table 4.3*** *– Deformable aluminium parameters*

Figure 4.53 hereafter shows the isometric view of the fan and filter, placed in front of the engine. Indeed, being just a parallelepiped with rectangular section, it is useless to show more than one view, since the isometric one is enough to understand how the component is modelled.

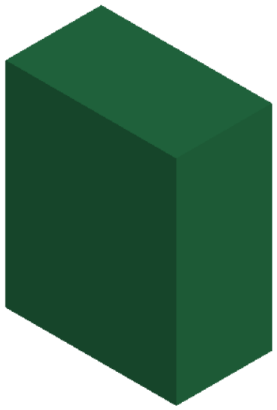

***Figure 4.53*** *– Isometric view of fan and filter*

As well as the previous components, the fan is not involved in the impact in the case of 750 $mm$, so that it will not be taken into consideration for that specific case. As it was done for the engine and the longitudinal beam, it is possible to appreciate the effective plastic strain, in the final deformed state, and for each case of interest, in the following Figure 4.54.

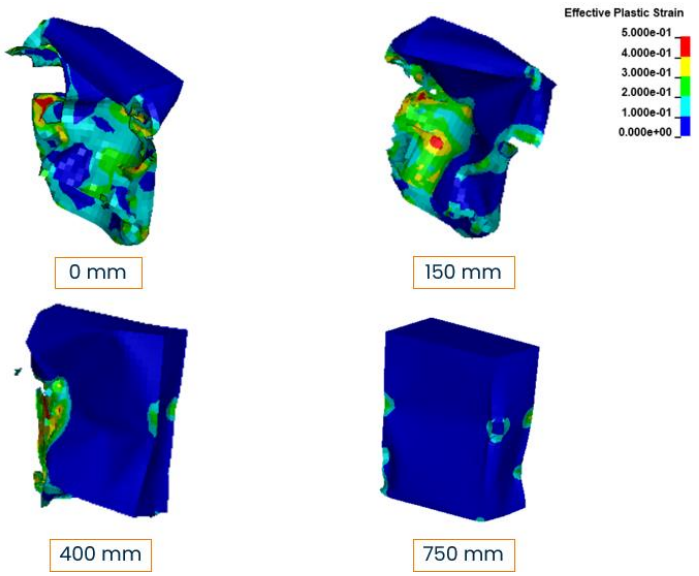


*Figure 4.54 – Effective plastic strain of fan and filter in final deformed state*

It is evident that the first two cases are the most severe, as far as the fan is concerned, since it is one of the first components that enters in contact with bollard. Perhaps, it could also be considered responsible of a bit of protection for the engine impact, lowering the displacement that the front face of the deformable engine is subjected to.

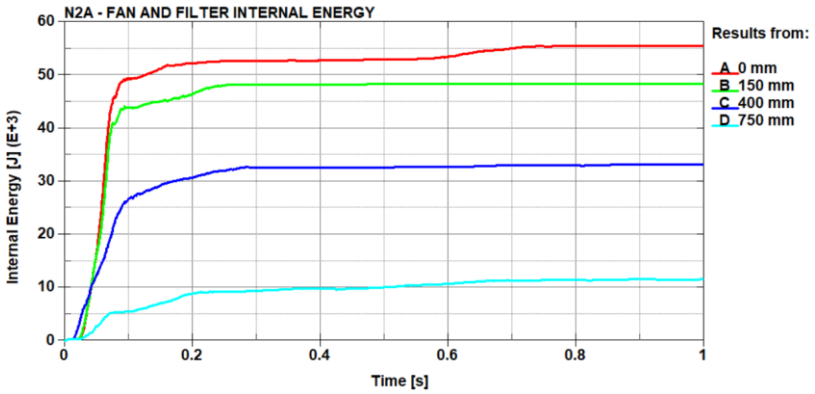


*Figure 4.55 – Fan and filter internal energy for each case*

Coherently to the plastic strains, Figure 4.55 indicates that in the reference case of 0 $mm$, the fan is capable of absorbing more energy from the impact, since it is perfectly centered with the bollard as well. In the other cases instead, the impact is marginal, and even in the last case of 750 $mm$ the fan and filter deformation could be due to some internal contacts, and not to the direct impact with the barrier, so that it will not be considered in the contribution analysis for this case.

### 4.4.4 Front Axle

Being the case of bollard moved of 750 $mm$ a bit different from the others, the components directly involved in the impact and that participate to the deformation of the system are different from the ones considered so far. The engine and the fan are positioned in the central part of the vehicle

indeed, so that they do not come in contact with the bollard, but they results to be deformed due to some contacts with other internal parts. For this reason, either the engine either the fan do not give enough contribution to the internal energy of the vehicle, and in fact, as it will be seen in the dedicated section, their energy percentage influence on the total energy absorption do not overcome the prescribed limit of 5%, and as a consequence they will not be taken into account in this case.

Looking at the right lower plot of Figure 4.45, the front axle appears to be the most deformed component for the case of bollard offset of 750 $mm$, together with the longitudinal beam, already discussed in section 4.4.2. Figure 4.56 illustrates this component in front and isometric views.

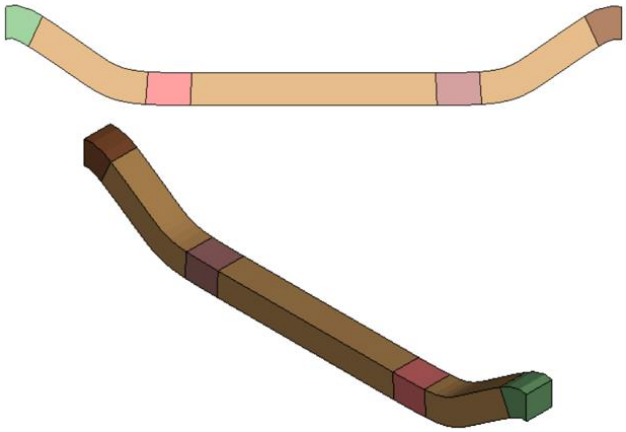

***Figure 4.56*** *– Front and isometric views of front axle*

Provided that the front axle internal energy overcomes the 5% of the total internal energy of the vehicle twice – both for 0 $mm$ and 750 $mm$ – it is better to study the effective plastic strain in each case, in order to understand the order of magnitude of the deformation that the component undergoes.

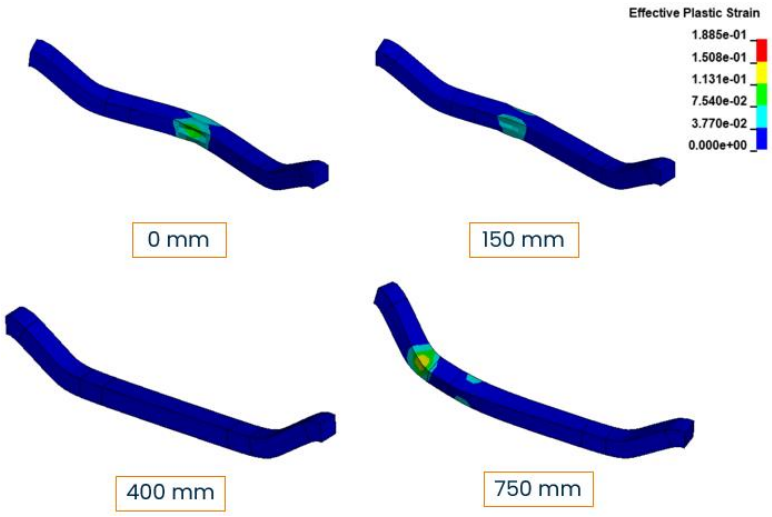


***Figure 4.57*** *– Effective plastic strain of front axle in final deformed state*

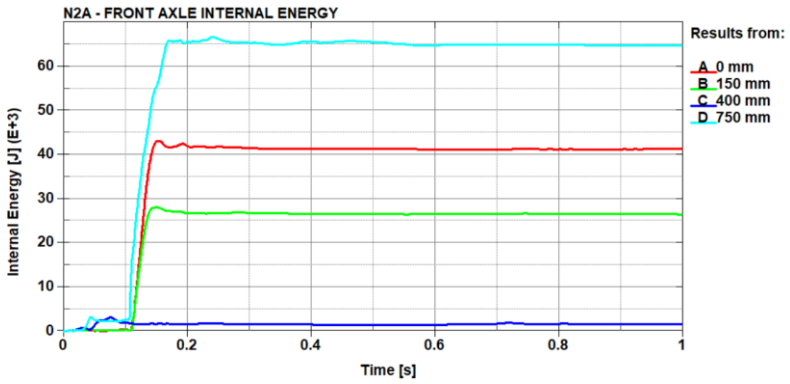


***Figure 4.58*** *– Front axle internal energy for each case*

Comparing the plot of Figure 4.58 and the plastic strains of Figure 4.57, it is evident that the highest deformation is present in the case of 750 $mm$, where the front axle provides a very high contribution to the internal energy of the system, as shown in Figure 4.45. The case of 400 $mm$ is evidently the less pronounced, also visible from the low level of relative internal energy and from the practically null effective plastic strain in that specific case.

### 4.4.5 Front bumper bar

The front bumper bar is used as support for the front bumper and realized in plastic deformable steel. Being one of first components that come in contact with the bollard, it is also well deformed in some of the considered cases.

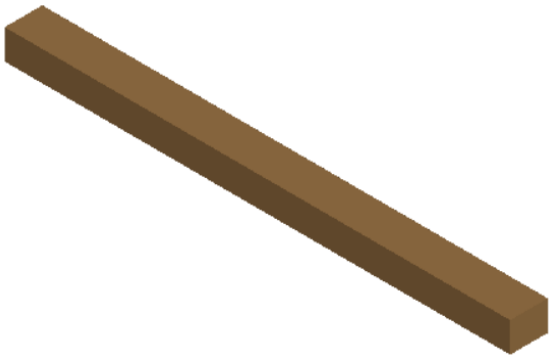

***Figure 4.59*** *– Isometric view of front bumper bar*

The contribution that it gives to the total internal energy in all the analysed cases is certainly not negligible, since it is always directly impacted by the bollard. In the specific cases of 400 $mm$ and 750 $mm$, the front bumper bar is responsible for the vehicle rotation, since it remains stuck in between the front axle and the bollard.

The following Figure 4.60 shows the plastic strain of this part, followed by the usual plot of its relative internal energy in Figure 4.61.

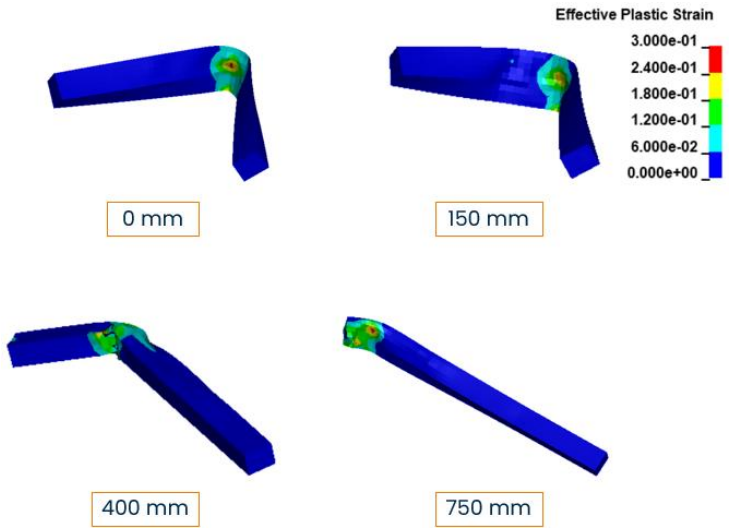


***Figure 4.60*** *– Effective plastic strain of front bumper bar in final deformed state*

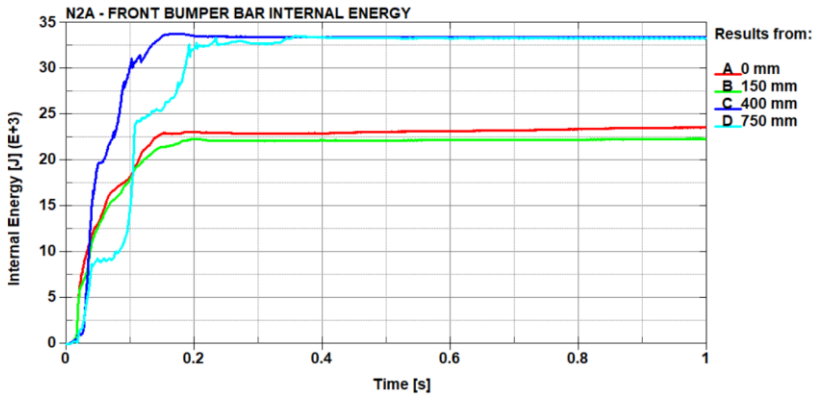


***Figure 4.61*** *– Front bumper bar internal energy for each case*

Since the front bumper bar is, together with the front bumper, one of the first component to impact the barrier, it is clear that it is deformed, of a not negligible quantity, in each case. However, this deformation does not overcome the limit of 5% of the total internal energy for the cases of 0 $mm$ and 150 $mm$, so that these two values will not be included in the following statistical analysis.

## 4.5 Statistical analysis on energy contributions

Having analysed each component by its own, in order to show how much it influences the internal energy of the vehicle, it could be useful to perform a statistical analysis based on the data that have been collected up to now, since percentage values could provide a better and clearer idea of the influence that each component has, in each of different case, on the general deformation, following the same line tracked for the tube shock case of study of section 2.2.2.

If for the tube shock case, the statistical comparison was done considering the mean values of the plot oscillations. In this case instead, the percentages will be computed using the maximum values of the internal energies, taken at the end of the simulation in the final deformed state, so that when the deformation of the components is expected to be the highest. Table 4.4 shows the maximum

energy values for each component and the corresponding percentages of influence with respect to the total internal energy of the system. The dash inside the table is used to indicate those components that have not been considered in the analysis, as it was previously explained.

| Component | **Max value** of components internal energy | | | |
|---|---|---|---|---|
| | 0 mm | 150 mm | 400 mm | 750 mm |
| Total | 614 kJ | 602 kJ | 579 kJ | 487 kJ |
| Engine | 44.6 kJ | 54.3 kJ | 20.5 kJ | - |
| Front long. beam | 86.3 kJ | 96.4 kJ | 227 kJ | 84.8 kJ |
| Fan and filter | 55.5 kJ | 48.4 kJ | 33.2 kJ | - |
| Front axle | 41.3 kJ | - | - | 64.8 kJ |
| Front bumper bar | - | - | 33.5 kJ | 33.4 kJ |

| Component | **%Influence** of components on total internal energy | | | |
|---|---|---|---|---|
| | 0 mm | 150 mm | 400 mm | 750 mm |
| Total | - | - | - | - |
| Engine | 7.3% | 9% | 4.5% | - |
| Front long. beam | 14% | 16% | 39.2% | 17.4% |
| Fan and filter | 9% | 8% | 5.7% | - |
| Front axle | 6.7% | - | - | 13.3% |
| Front bumper bar | - | - | 5.8% | 6.9% |

*Table 4.4 – Max value and %Influence of components on total internal energy*

The percentages reported in the right table reflect what has been said in the sections dedicated to the components deformation, and it is even clearer that the front longitudinal beam has a key role in the deformation mechanism of the whole system, regardless of which bollard position is considered. All the other components, including the engine, have not negligible energy values, even if they do not have a so high influence on the system deformation, as it is instead for the longitudinal beams.

To have a more schematic view, two histograms, based on the data collected in Table 4.4, have been created and shown hereafter in Table 4.5.

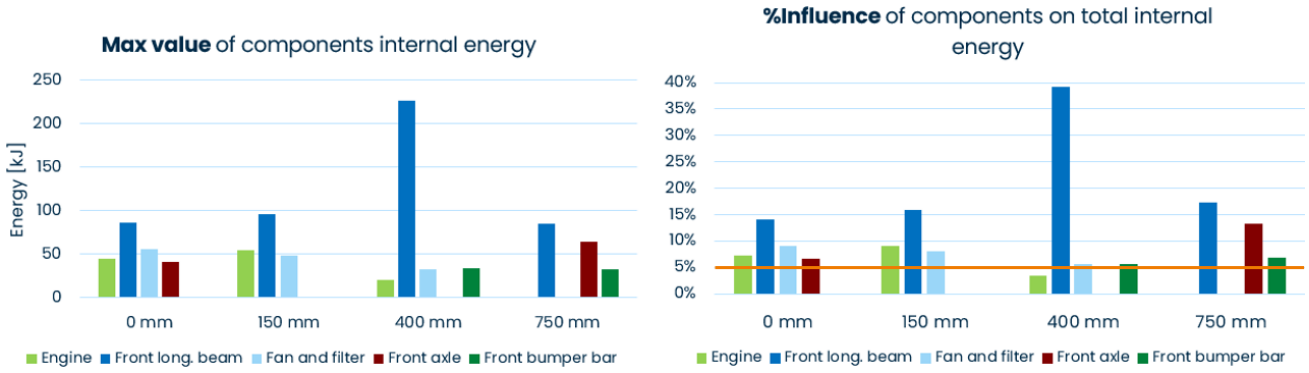


*Table 4.5 – Histogram max values and %Influence of components on total internal energy*

For sake of completeness, Table 4.6 lists the total energy values for each case, since inserting the corresponding bars into the left histogram would have distorted the other columns, making the interpretation of the chart a bit difficult.

| *CASE* | *TOTAL ENERGY MAX VALUE* |
|---|---|
| ***0 mm*** | 614 $kJ$ |
| ***150 mm*** | 602 $kJ$ |
| ***400 mm*** | 579 $kJ$ |
| ***750 mm*** | 487 $kJ$ |

***Table 4.6*** *– Total energy values for each case*

To have an evident indication of the chosen threshold of 5% of the total internal energy, a red line has been traced on the right histogram. It is visible that all the bars overcome the red line, except for the green one relative to the case of 400 $mm$, corresponding to the engine contribution. Anyway, the engine has been involved in the analysis as well, since it remains a key component not only in the deformation mechanism of the system, but also in the vehicle movement after the impact, thanks to the heavy weight of the internal rigid part, covered by the deformable one, which has been analysed so far and explained in previous sections.

## 4.6 Case of study conclusions

In order to have an overview of the cases that have been studied and the results that have been obtained, it could be useful to try to get some conclusions from the analysis performed up to now.

The first consideration that can be made regards the robustness of the N2/N3 generic vehicle model. It has been shown indeed that the model can be effectively used in simulations like the previous ones, but it can also be adapted to different vehicle categories, being representative of real vehicles as well.

Regarding the validation procedure, it was interesting to see if there was a misalignment of the bollard of the experimental test, that caused an evident asymmetry of the results. But the case of bollard moved of 150 $mm$ highlighted that this was not the prior cause of the non-symmetric motion of the real vehicle, which falls in the inertia of the semitrailer that pushes the vehicle cabin and triggers its rotation.

From the sensitivity analysis performed on the model instead, it is evident that the influence of the bollard position on the different results is huge. Moreover, if a quick comparison between the limit cases of 0 $mm$ and 750 $mm$ is made, the behaviour of the curves, rather than the animations, is completely different. As it was previously said, this is also the reason why, in the barrier design phase, a maximum distance between two consecutive bollards is necessary, because the amount of damage that can produce a single and not perfectly centered bollard is not sufficient to protect prescribed areas from possible terroristic attacks.

The last statistical analysis instead, revealed that the component that plays a key role in the deformation mechanism of the vehicle model is the longitudinal beam. The most interesting case was indeed that one of the bollard moved of 400 $mm$ from the central position, in which the longitudinal beam provides almost half of the total internal energy of the vehicle.

Anyway, it has been demonstrated that the bollard position has a great influence in the exchanged energies, rather than on the contact force exchanged between the bollard and the vehicle. This influence has not been appreciated in the X momentum plot, perhaps due to the linear dependence of the momentum on the velocity.

At the end of the analysis, a statistical view of the results was provided, in order to better summarize the results obtained from the current investigation, with a particular focus on the contribution given by some components of the model, whose internal energy was higher than the chosen threshold of 5% of the total internal energy, on the global deformation. This overview provided a hint of how simply breaking the symmetry of the impact would produce different loads on the barrier. Moreover, it has been demonstrated that the first two cases are the most critical ones, perhaps due to the rigid engine shock, even because this engine modelling does not provide a reliable representation of a real engine.

# Conclusions

In the present thesis, a comparison between the two software LS-Dyna and EPX has been performed, with the goal of establishing a solid benchmark, trying to minimize the existing differences analysing the same model. This test has been performed on two different cases, the tube shock and the tube shock-crush, reported in Chapter 2 and Chapter 3.

The investigation relative to the tube shock has demonstrated that the two software are particularly sensitive to the contact penalty parameters, so that a small variation in the contact setup had a deep influence on results, in terms of energy components and momentum. Anyway, their overall behaviour seems to be quite coherent.

On the other hand, the tube shock-crush confirmed that the two software can be considered almost equivalent in the numerical computation, regardless the model to be tested. Results indeed show not only the same trend, but they are also not so sensitive to the variation of the contact stiffness scale factors, as it was instead for the tube shock case, and even the contact formulation – i.e. Standard Penalty or Pinball – has shown to be not so impacting.

In the last Chapter 4, the reliability of the generic N2/N3 vehicle model was first verified, in order to understand if it could have been used for some sensitivity analyses. The robustness of the model has been demonstrated through a validation procedure, comparing a simulation of a bollard impact with a real experimental test. This validation showed that the model can be considered, with a certain level of tolerance and approximation, valid and representative of a real vehicle, so that a deeper investigation has been conducted.

The performed sensitivity analysis highlighted that even small variations of the bollard position produce very different results, in terms of energy absorption and loads on the bollard itself. To have an overview, apart from the reference case of centered bollard, three different configurations have been identified, with reference to the key component that has been shown to be the front longitudinal beam.

Distinct deformations have been indeed appreciated from case to case, and different components participated to the overall deformation of the vehicle, measured by the internal energy. The component that has been shown to have the heaviest influence on results is the longitudinal beam, main responsible of the bending behaviour of the vehicle when the bollard was not perfectly centered with the travel direction. However, the most critical cases are those that directly involve the engine shock, due to the rigid impact between the inner part of the engine and the bollard. This contact indeed created some significant peak in the contact force, making the overall deformation of the system more severe.

Finally, the same statistical methodology used in Chapter 2 was applied to this analysis, in order to understand the influence of each of the relevant components on the total internal energy, in percentage terms, confirming the hypothesis previously made. This methodology can be effectively applied to any case of interest – i.e. different impacts and barriers.

# Bibliography

[1] JRC, “Joint Research Centre,” [Online]. Available: https://commission.europa.eu/about-european-commission/departments-and-executive-agencies/joint-research-centre_en.

[2] M. Larcher and V. Karlos, “Guideline: Building Perimeter Protection: Design recommendations for enhanced security,” European Commission, Ispra, Italy, 2020.

[3] M. Larcher, V. Karlos, G. Valsamos and F. Casadei, “A numerical framework to support the certification of barrier testing,” European Commision, Ispra, Italy, 2020.

[4] M. Larcher, V. Karlos and G. Solomos, “Review on vehicle barrier protection guidance,” European Commission, Ispra, Italy, 2017.

[5] UNECE, “Consolidated Resolution on the Construction of Vehicles (R.E.3),” UNECE, [Online]. Available: https://unece.org/transport/vehicle-regulations/wp29/resolutions.

[6] J. Hallquist, “LS-DYNA Theory Manual,” Ansys, 2023.

[7] SVS FEM s.r.o. | Ansys Channel Partner, “SVS FEM,” [Online]. Available: https://www.svsfem.cz/.

[8] comPADRE - Digital Resources for Physics and Astronomy Education, “Tracker - Video Analisys and Modeling Tool,” [Online]. Available: https://physlets.org/tracker/.

[9] M. Šebík and Z. Kodajková, “Generic vehicle model N2A & N3D,” SVS FEM s.r.o., Brno, Czech Republic, 2023.

[10] *Crash test DAF LF 45 vs. Bollard: PAS 68 / IWA 14-1.* [Film]. Germany: CTS, 2021.

## Acknowledgements

At the end of this journey, made of sacrifices, fatigue, successes and delusions, having a look back to the past, I can say I am proud of what I have achieved with the determination I have had from the very first day I decided to take on this lifetime experience. Never have I thought of giving up, and this was the secret to keep going, even when difficulties arose. For this reason, I want to say thanks to *myself* for having become an automotive engineer.

I would like to thank my family, my *mom* and my *dad*, who always have been alongside me, supporting my decisions and spurring me to do better and better, my grandmothers, *nonna Carmen* and *nonna Maria*, who cannot be here with me, but I have never felt they left me. I would never have become what I am today without your help and your presence.

I would like to thank my best friends, *Sebastian* and *Rita Maria*, for being present every day and for sharing with me good and bad moments, made of football discussions and incredibly long calls. I will never feel alone with you alongside me.

I would like to thank my *loggia's* friends, *Ciccio*, *Daniele*, *Mikele* and *Sara*, mates of thousand adventures, from school to today. We grew up together and we will continue to do so, does not matter the distance between us.

I would like to thank my best colleague, *Carmine*, not only a colleague but a real and close friend, who accompanied me during school and my bachelor's degree, and only by chance not during this master's degree. You pushed me to reach my goals more than you think.

I would like to thank my girlfriend, *Fatima*, even if it is not so much time that we are together, you are entirely part of my life, I could not have done it without your daily support.

I would like to thank my *caffè sociale's* friends, *Luigi*, *Matteo* and *Simone*, close friends from the early years of our lives, mates of futsal matches, large dinners, long travels. Thanks for all the love and affection you have shown me throughout the years.

I would like to thank my basketball teammates, my second family, *Ivo* and *Marco*, so many years we spent together on a basketball court, sharing amazing victories and heavy losses, laughs and arguments, and for this reason we have become much stronger than ever.

I would like to thank my *via Bainsizza's friends*, *Matteo* and *Samuele*, my housemate and stadium mate respectively. I would have been lost in such a big city like Turin, without your help and your support. We shared some wonderful moments, and I hope one day we will be reunited again.

I would like to thank my master's degree colleagues, *Federica* and *Jacopo*, for the great collaboration we have had together, I would have never wished better colleagues in our group.

I would like to thank my thesis colleague, *Alessandro*, who worked with me the last nine months. We had a lot of stuff to deal with, but at the end, we came out well and we ended up this work together, as we have started. Half of the work belongs to you.

Last but not least, I would like to thank *Professor Scattina*, for his availability and kindness

during the development of this thesis work, during which he gave me the possibility of growing up as a person and as an engineer, rather than *Dr. Damijan Markovic*, *Dr. Martin Larcher* and all the *JRC staff* for the possibility to collaborate with them in the realization of this work and for the amazing experience we had in visiting their facilities in Ispra.

Thanks *everyone* for this amazing journey, I will never forget it.

Annibale